

**Interplay of driving, nonlinearity and dissipation  
in nanoscale  
and ultracold atom systems**

Inaugural-Dissertation

zur

Erlangung des Doktorgrades der  
Mathematisch-Naturwissenschaftlichen Fakultät  
der Heinrich-Heine-Universität Düsseldorf

vorgelegt von

Vittorio Peano Cavaola

aus Milano, Italien

März 2006

Aus dem Institut für Theoretische Physik IV  
der Heinrich-Heine-Universität Düsseldorf

Gedruckt mit der Genehmigung der  
Mathematisch-Naturwissenschaftlichen Fakultät der  
Heinrich-Heine-Universität Düsseldorf

Referent: Prof. Dr. Reinhold Egger

Koreferent: PD Dr. Michael Thorwart

Tag der mündlichen Prüfung: 16 Mai 2006

# Contents

<b>1</b>	<b>Introduction</b>	<b>1</b>
1.1	Problems addressed in this thesis . . . . .	3
<b>2</b>	<b>Dynamics of the Quantum Duffing oscillator</b>	<b>9</b>
2.1	Introduction: Classical Duffing oscillator . . . . .	10
2.2	Experimental systems . . . . .	11
2.2.1	The mechanical nanoresonator . . . . .	11
2.2.2	The SQUID . . . . .	12
2.3	Coherent dynamics . . . . .	13
2.3.1	Exact Floquet solution . . . . .	14
2.3.2	Rotating wave approximation (RWA) . . . . .	15
2.4	Dissipative dynamics . . . . .	20
2.4.1	The system-bath model and the Langevin equation . . . . .	22
2.4.2	The influence functional and the Markovian master equation (MME) . . . . .	25
2.4.3	Floquet master equation . . . . .	29
2.4.4	RWA master equation . . . . .	32
2.4.5	Observable for the nonlinear response . . . . .	33
2.5	Analytical results in the perturbative regime . . . . .	34
2.5.1	One-photon resonance vs. antiresonance . . . . .	35
2.5.2	Multiphoton resonance vs. antiresonance . . . . .	36
2.6	Numerical results in the strong driving regime . . . . .	44
2.6.1	Amplitude and phase response . . . . .	45
2.6.2	Interplay between dissipation and tunnelling . . . . .	47
2.6.3	Quantum relaxation in the driving induced bistability . . . . .	52
2.7	Conclusions and outlook . . . . .	54
<b>3</b>	<b>Nanoscale atomic waveguides with suspended carbon nanotubes</b>	<b>55</b>
3.1	Introduction: Alkali atoms in electromagnetic fields . . . . .	55
3.1.1	Zeeman interaction with an external magnetic field . . . . .	56
3.1.2	Dynamical Stark interaction with a laser field . . . . .	58
3.2	The setup for a nanowaveguide . . . . .	63
3.3	Influence of destructive effects . . . . .	65
3.4	Number of trapped atoms and size of atom cloud . . . . .	67
3.5	Double-well potential with two carbon nanotubes . . . . .	68
3.6	Conclusions . . . . .	71
<b>4</b>	<b>CIR in arbitrary quasi-1D traps</b>	<b>73</b>
4.1	Introduction: Scattering in free space . . . . .	74
4.1.1	Low energy scattering . . . . .	76
4.2	The two-body problem in presence of transverse confinement . . . . .	80

4.3	Bound-state solutions . . . . .	82
4.3.1	Dimer limit . . . . .	84
4.3.2	BCS limit . . . . .	85
4.4	Scattering solutions . . . . .	86
4.4.1	One-dimensional scattering length $a_{1D}$ . . . . .	86
4.4.2	Interpretation of the CIR as Feshbach resonances . . . . .	87
4.5	Special case of harmonic confinement . . . . .	89
4.5.1	Identical frequencies . . . . .	90
4.5.2	The case $\omega_1 \neq \omega_2$ : Relation to experiments . . . . .	92
4.6	Non-parabolic confining potentials . . . . .	95
4.7	Conclusions . . . . .	95
<b>5</b>	<b>Summary</b>	<b>97</b>
<b>A</b>	<b>Model for the driven suspended nanoresonator</b>	<b>99</b>
<b>B</b>	<b>Van Vleck perturbation theory</b>	<b>101</b>
<b>C</b>	<b>A Floquet master equation for a bichromatically driven system</b>	<b>103</b>
<b>D</b>	<b>Pseudopotential method for the two-body problem in free space</b>	<b>107</b>
<b>E</b>	<b>Short time Green's function and the operators <math>\zeta_E</math> and <math>\tilde{\zeta}_E</math></b>	<b>109</b>
E.1	Short-time expansion of the Tokatly Green's function . . . . .	109
E.2	Evaluation of the operators $\zeta_E$ and $\tilde{\zeta}_E$ . . . . .	110
	<b>References</b>	<b>113</b>
	<b>Acknowledgement</b>	<b>119</b>

# 1 Introduction

*La filosofia è scritta in questo grandissimo libro che continuamente ci sta aperto innanzi a gli occhi (io dico l'universo), ma non si può intendere se prima non s'impara a intender la lingua, e conoscer i caratteri, ne' quali è scritto. Egli è scritto in lingua matematica, e i caratteri son triangoli, cerchi, ed altre figure geometriche, senza i quali mezzi è impossibile a intenderne umanamente parola; senza questi è un aggirarsi vanamente per un oscuro laberinto [1].*

*(Galileo Galilei)*

With these words Galileo Galilei expresses the very essence of the -at his time exploding- scientific revolution. To the benefit of those who are not familiar with the italian language, we can summarize the above citation as follows: The universe is like a book that stands open in front of us. In order to be able to read it, one should first learn the language it is written in. This language is mathematics.

Galileo adds that the words are triangles, circles and other geometric shapes. It was the year 1623. In the focus of Galileo's studies was the dynamics of the celestial bodies in the solar system. The language of theoretical physics has been developing ever since, while the book has been deciphered in greater detail.

This thesis can be regarded as a 'footnote' in a large 'chapter' of the 'book': the physics of condensed matter systems, i.e. those systems composed by an extremely large number of constituents whose interactions are relevant but do not suppress their quantum nature. There is a large variety of systems that falls in this category including conduction electrons in metals, unpaired spins and mechanical degrees of freedom of atoms in crystals and ultracold gases of alkali atoms.

In particular, the latter class of systems has been one of the most important playgrounds for fundamental research in the last ten years and is the framework of Chapters 3 and 4. Another class of systems attracting an increasing attention of the scientific community are nanoscale electromechanical systems (NEMS) whose properties are determined by the interplay of mechanical and electronic degrees of freedom. In Chapter 2, we present a general model that could be implemented by a system belonging to the latter class, i. e., a nanoresonator. On such a system is also based the nanowaveguide for alkali atoms proposed in Chapter 3 that, if realized, could represent a fascinating link between the two fields of NEMS and ultracold atoms.

The 'language' of condensed matter physics is not unique. A wealth of different techniques has been developed to deal with previously unread part of the big 'book'. Nevertheless a new theoretical formalism is never univocally associated to a certain physical system but always prove to be a valuable tool in investigating systems very different in nature. In fact, few fundamental features determine which 'language'

should be adopted to describe a certain system. Most important are (i) the system dimensionality, (ii) the statistics of its constituent particles, (iii) the strength of the particle-particle interactions and (iv) the degree of disorder of the system:

(i) Not all condensed matter systems are embedded in the ordinary three-dimensional space. Reduced dimensionality arises in a lattice with strongly anisotropic interactions or when the degrees of freedom in a given spatial dimension are frozen due to a gap larger than the chemical potential in the corresponding excitation spectrum. In some systems, e.g. quantum dots, SQUIDs, flux and charge qubits, only a discrete number of degrees of freedom determine the observables of interest. One refers to such systems as zero-dimensional systems.

(ii) The particles can be either bosons or fermions. The statistics determines the symmetry properties of the total wave function which specifies the system configuration. It can be regarded as an effective force, which is attractive for bosons and repulsive for fermions.

(iii) Noninteracting many-body Hamiltonians are quadratic and can therefore be solved exactly. Weak interactions can be taken into account by means of ordinary perturbation theory. For stronger interactions, a *mean field* approach is appropriate. In the framework of the *path integral* formulation of quantum mechanics, one can straightforwardly look for mean-field solutions and perform a loop expansion to evaluate the corresponding corrections. In 1D and 2D systems in the thermodynamic limit, the mean-field approach breaks down (Mermin-Wagner theorem). In this limit one has to rely on other techniques like renormalization group analysis, numerically exact Monte Carlo integration and other numerical techniques. In addition, many exact analytical solutions are available. The physical picture that arises from these solutions is fascinating: due to the interplay of statistics and interactions, the distinction between bosonic and fermionic excitations is more subtle. For instance, in a 1D boson system, strong repulsive interactions mimic the Pauli principle, and give rise to a Tonks gas which is very similar to a degenerate gas of free fermions. The emerging excitations in 1D or 2D might have fractional statistics as well.

(iv) When disordered systems are considered, the governing Hamiltonian is usually not known. However many observables of interest, e. g., the conductance in a quantum wire, are self-averaging and a statistical approach is appropriate. The self-averaging quantities depend only on the strength of the disorder and on the symmetry of the system. For this reason, symmetric spaces have proved to be a valuable tool of investigation for such systems.

The systems of interest in this thesis are of reduced dimensionality, weakly interacting and with negligible disorder. Other common features to the problems addressed in this thesis are dissipation, nonlinearity and driving.

In chapter 2, we consider a zero-dimensional condensed matter system with a single relevant macrovariable, e. g., the phase difference in a Josephson junction or the amplitude of the fundamental mode in a nanoresonator. A natural approach to this kind of systems is to regard the remaining degrees of freedom as a bath causing dissipation and decoherence. A first order expansion in the coupling with the macrovariable yields a Markovian master equation for the reduced density matrix

obtained by tracing out the microscopic variables. A quantum field in a coherent state, e. g., a laser field, coupled to the system can be treated classically yielding a time-periodic system-Hamiltonian. Such Hamiltonians can be solved exactly by means of *Floquet theory* -the analogue for time-periodic systems of *Bloch theory*.

In Chapters 3 and 4, we focus on a particular condensed matter system: a gas of alkali atoms. Interestingly enough, a single alkali atom fits rather well in the above picture. In fact, it is a many-body system made out of protons, neutrons and electrons, whose relevant variable is the atom center-of-mass (COM), whereas the remaining microscopic ones are the electron degrees of freedom. In this case, an effective Hamiltonian for the COM coordinates can be derived by means of a simple adiabatic approximation. In presence of a tight transverse confinement, this single particle picture is the starting point for deriving an effective 1D many-body theory which describes a large ensemble of atoms. The building blocks of this theory are few-body problems, as the two-body one considered in Chapter 4.

## 1.1 Problems addressed in this thesis

In the following pages, we introduce the reader to the three problems in the focus of this thesis. These three topics are analyzed in detail in Chapters 2, 3 and 4, respectively.

### The quantum Duffing oscillator

Classical nonlinear systems subjected to strong periodic external driving often have several stable stationary states for which the amplitudes and phases of the forced vibrations differ in size [2–4]. One of the simplest theoretical models which show the coexistence of two stable states induced by external driving is the well-known classical Duffing oscillator. An anharmonic statically monostable potential can be driven into a dynamically bistable regime showing various interesting features of non-linear response [2–4], such as hysteresis, period doubling, and thermal activation when finite temperatures are considered. The external driving field with frequency  $\omega_{\text{ex}}$  induces an effective dynamic bistability which is manifest by the non-monotonous dependence of the amplitude  $A$  of the stationary vibrations for varying  $\omega_{\text{ex}}$ . For the classical system where all potential energies are allowed, this response curve  $A(\omega_{\text{ex}})$  is smooth showing only two points of bifurcation for the related bistability. If the control parameter  $\omega_{\text{ex}}$  is additionally varied adiabatically, hysteretic jumps between the two stable states occur. If additional thermal noise is added to the system, the regime of bistability shrinks due to thermal escape of the metastable state.

In the focus of Chapter 2 of this work is the dynamics of the quantum analogue of the classical Duffing oscillator. The investigation of this problem is motivated by two main reasons. On one hand there is its generality: Its characterizing features nonlinearity, driving and dissipation are ubiquitous in physics. As a consequence, there is a variety of physical systems, which are accurately described by such a model. Some examples are: (i) a driven nanoresonator, (ii) a superconducting ring

interrupted by a Josephson junction driven by an external radiofrequency radiation (in the literature referred to as SQUID, because it is the active part in the class of devices known as *superconducting quantum interference devices*), (iii) a polyatomic molecule driven by a laser pulse and (iv) a coherently driven dispersive cavity. On the other hand, the model is of an intrinsic theoretical interest. The interplay between nonlinearity, driving and dissipation might be very complex and produce a rich variety of phenomena, such as coherent and dissipative tunnelling, quantum chaos, etc.

The problem of a driven quantum oscillator with a quartic nonlinearity has been investigated theoretically in earlier works in various context. In the context of the radiative excitation of polyatomic molecules [5], Larsen and Bloembergen have calculated the wave functions for the coherent multiphoton Rabi precession between two discrete levels for a collisionless model. More recently, also Dykman and Fistul [6] have considered the bare nonlinear Hamiltonian under the rotating wave approximation. Drummond and Walls [7] have investigated a similar system occurring for the case of a coherently driven dispersive cavity including a cubic nonlinearity. Photon bunching and antibunching have been predicted upon solving the corresponding Fokker-Planck equation. Vogel and Risken [8] have calculated the tunneling rates for the Drummond-Walls model by use of continued fraction methods. Dmitriev, D'yakonov and Ioffe [9] have calculated the tunneling and thermal transition rates for the case when the associated times are large. Dykman and Smelyanskii [10] have calculated the probability of transitions between the stable states in a quasi-classical approximation in the thermally activated regime. Recently, the role of the detector (in this case, a photon detector) has been studied for the quantum Duffing oscillator in the chaotic regime [11]. The power spectra of the detected photons carry information on the underlying dynamics of the nonlinear oscillator and can be used to distinguish its different modes.

Most of these works focus on the connection between the classical and the quantum dissipative dynamics [7–11]. The others discuss the coherent dynamics without considering the interaction with the environment [5, 6].

Conversely, our approach is to start from an exact solution for the isolated system and include the influence of the environment by means of a Born-Markovian master equation. The main advantage of this strategy is that it allows to explore the connections between the coherent and the dissipative dynamics, which remained unaddressed so far.

In particular, we lay the focus on the lineshape of the nonlinear response. The central result is to discover a resonant or an antiresonant behavior of the dissipative system corresponding to multiple multiphoton transitions for the coherent system. The resonances and antiresonances are the result of a complex interplay between dissipation and tunnelling. They are studied, for a broad range of bath and system parameter, by means of perturbative analytical calculations and exact (within the Markovian approximation) numerical computations. In particular, the crossover between the resonant and antiresonant behavior is studied in detail and interpreted in terms of an analogy between a dynamically bistable quasipotential for the driven system and a double-well potential describing a static system.



The quasipotential is at the origin of the classical bistability. In the corresponding quantum system, it determines a separation of time scales: meaning that there is a relaxation process which is much slower than all the other dissipative processes. In the semiclassical limit, the slow dynamics is interpreted as a tunnelling transition between the two classically stable states. In the deep quantum limit considered here, a separation of time scales is already evident, but is suppressed by resonant tunnelling at the multi-photon transitions.

Our results have previously been published in Refs. [12–14].

## Nanoscale atomic waveguides with suspended carbon nanotubes

The ongoing progress in the fabrication and manipulation of micro- or nanoscale structures has recently allowed for systematic studies of ultracold atom gases, where current-carrying wires and additional magnetic bias fields generate magnetic fields trapping neutral atoms (‘atom chips’) [15, 16]. For instance, the Bose-Einstein condensation (BEC) of microchip-confined atoms has been successfully demonstrated by several groups [17]. So far, decoherence and atom loss constitute central impediments, since atoms are relatively close to ‘hot’ macroscopic surfaces or current-carrying wires (with typical diameters of several  $\mu\text{m}$ ), where the Casimir-Polder potential and Johnson noise can seriously affect stability [18–20]. To reduce these effects, further miniaturization to the nanoscale regime would be desirable. In particular, this is promising in the context of integrated atomic matter-wave interferometry and optics [21], and combines the strengths of nanotechnology and atomic physics. While at first sight this goal conflicts with the requirement of large currents forming tight trapping potentials, we propose that when using suspended carbon nanotubes (NTs) [22] (with diameters of a few nm) as wires, nanoscale atom chip devices with large current densities can be designed. In turn, these devices allow to trap ultracold atom gases basically free of trap-induced decoherence or atom losses, with the gas containing few tens of atoms. Since disorder is generally weak in NTs, the (extremely large) current density distribution is spatially homogeneous, which allows to overcome the problem of fragmentation of the atom cloud which plagues common atom chip designs. Moreover, they can be built with state-of-the-art technology.

With relevant length scales below optical and cold-atom de Broglie wavelengths, this also paves the way for the observation of interesting and largely unexplored many-body physics in one dimension (1D) [23]. Examples include the interference properties of interacting matter waves [24], the 1D analogue of the BEC-BCS crossover [25–27] and confinement induced resonances in 1D trapping potentials [28–31]. Previous realizations of 1D cold atoms were reported using optical lattices [32–34] and magnetic traps [35], but they involve arrays of 1D or elongated 3D systems, where it is difficult to separately manipulate a single 1D atom cloud (the distances between the 1D systems composing the array are few hundred nm). A noteworthy advantage of our proposal against dipole optical trap is that arrays of many NT waveguides can be built, where it is possible to manipulate an individual trap by changing the current through an individual NT. A further advantage of our proposal against the common macroscopic atom chips is that it minimizes unwanted

substrate effects and implies a drastically reduced transverse size (a few nm) of the cloud.

Our results have previously been published in Ref. [36].

## Confinement-induced resonances in arbitrary quasi-one-dimensional traps

A strongly interacting ultracold atom gas displays interesting features of a correlated quantum many-body system when its dynamics is confined to one dimension [23]. The presence of a transverse confining potential has been shown to induce characteristic resonances in the coupling constant of the two-particle s-wave scattering process [28–31], which have become known as confinement-induced resonances (CIR). The existence of the CIR has been revealed under the simplifying assumption of a transverse parabolic confinement potential with length scale  $a_{\perp}$  and for the case that the two scattering atoms belong to the same species [28–31]. In this case, the center-of-mass (COM) and relative coordinates of the two particles can be separated, allowing to factorize the problem into single-particle problems. At low temperatures, only the COM ground-state is occupied, the decoupled COM motion can be disregarded, and the two-body problem can be solved exactly within the pseudopotential approximation. The result is that there is exactly one bound state for any 3D scattering length  $a$ . In the limit of small binding energy, the particles are tightly bound in the lowest-energy transverse state and form a very elongated dimer. The appearance of such a bound state is purely due to the confinement, since for  $a < 0$  no dimer is formed in free space. In the opposite limit of large binding energies, the dimer becomes spherically symmetric. In this regime, the confinement is not effective, and the free-space result is recovered. Moreover, a unitary equivalence exists between the Hamiltonian and its projection onto those channels which are perpendicular to the one with lowest energy. As a consequence, to each bound state corresponds a bound state of the closed channels, which then causes the CIR [29]. It occurs at a universal value of the ratio  $a_{\perp}/a = \mathcal{C} = -\zeta(1/2, 1) \simeq 1.4603$ , where  $\zeta$  is the Hurvitz zeta function. The influence of the CIR has also been studied for the three-body [37] and the four-body problem [27] in the presence of confinement. In particular, the solution of the four-body problem completely determines the corresponding quasi-1D many-body BCS-BEC crossover phenomenon [27]. Recently, the existence of the confinement-induced molecular bound state in a quasi-1D Fermionic  $^{40}\text{K}$  atom gas confined in an optical trap has been reported [38]. By using rf spectroscopy, the binding energy of the dimer has been measured as a function of the scattering length, with quantitative agreement to the results of Ref. [29]. However, the existence of the CIR in the scattering states remains to be observed.

Although the analytical results for the parabolic confinement are instructive, realistic traps for matter waves frequently have non-linear potential forms, see for instance Ref. [36] for a particular example of a trap on the nanometer scale. To give another example, for the problem of tunneling of a macroscopic number of ultracold atoms between two stable states of a trapping potential, the nonlinearity clearly is crucial. Hence generalization to the non-parabolic case is desirable and provided in

this work. In addition, we consider traps with two different species of atoms. Note that sympathetic cooling techniques require to study this case. Different trap frequencies may arise for different atom species, e.g., because of different atom masses or different magnetic quantum numbers. Here we obtain general expressions for the bound-state energies and scattering resonances when the COM and the relative degrees of freedom do not decouple anymore. In the parabolic limit and for intraspecies scattering, we recover well-known results [28, 29]. For the general case, we show that more than one CIR may appear, and that it depends on the symmetry properties of the confining potential how many resonances occur. We apply our formalism to two experimentally relevant cases: (i) interspecies scattering in a two-species mixture of quantum degenerate Bose and Fermi gases in an optical trap, and (ii) a single species cloud in a magnetic trap, taking into account non-parabolic corrections due to a longitudinal magnetic field suppressing Majorana spin flips.

As we will discuss below in more detail, the CIR has a close similarity to the well-known Feshbach resonance [39], which arises if the Hilbert space can be divided into open and closed channels coupled together by a short-range interaction. Due to this small but finite coupling, two incoming particles initially in the open channel visit the closed channels during the scattering process. If a bound state with energy close to the continuum threshold exists, such a process is highly enhanced and a resonance results.

Our results have previously been published in Ref. [40].



# 2 Dynamics of the Quantum Duffing oscillator

In the focus of this chapter is the dynamics of the Duffing oscillator in the deep quantum limit. This model describes a periodically driven anharmonic oscillator coupled to a thermal bath that causes noise and dissipation.

The Hamiltonian of the isolated system is time-periodic and allows the application of Floquet theory, which is the analogue of Bloch theory for space-periodic systems. In this theory, the analogue of the quasimomenta are the quasienergy. The quasienergy spectrum of the driven anharmonic oscillator displays multiple avoided crossings, which correspond to multiple multi-photon transitions. Near the multi-photon transitions it is very similar to the energy spectrum of a static double-well potential.

This analogy can be better understood within the framework of the *rotating-wave approximation* (RWA), which consists in switching to the rotating frame and disregarding the time dependent terms in the transformed Hamiltonian. We can then identify the eigenvalues of this approximate Hamiltonian with the quasienergies of the Floquet theory. Moreover, it is possible to derive a quasipotential, which has the shape of a tilted Mexican hat. Its surface is divided into an internal and an external dome. For a quasienergy within a certain range, there are two classical solutions associated to the two different domes. When the energy is quantized, if there are a couple of levels corresponding to the same energy there can be many other pairs with the same energy. When the driving frequency is changed, the shape of the potential changes and the degeneracy is lifted: the spectrum displays multiple exact crossings. If tunnelling is considered, the degeneracy is lifted and the exact crossings become avoided crossings.

We include the dissipative influence of the environment by means of a Born-Markovian master equation. Within the RWA we find that the dynamics around the avoided quasienergy level crossings is well described by a simplified master equation involving only a few quasienergy states. Around the anticrossings, we find resonant as well as antiresonant nonlinear responses depending on the damping strength. The underlying mechanism is worked out in the perturbative regime of weak nonlinearity, weak driving and weak damping. There, Van Vleck perturbation theory allows to obtain the quasienergies and the quasienergy states analytically. The master equation can then be solved in the stationary limit and subsequently, the line shapes of the resonant as well as the antiresonant nonlinear response can be calculated in closed form.

The chapter is organized in the following way: In Section 2.1, we review the classical dynamics of the Duffing oscillator. In Section 2.2, we present the physical systems, which seem to be the most promising candidates to implement experimentally the quantum Duffing oscillator. In Section 2.3, we focus on the coherent

dynamics. We move on to Section 2.4, where we consider the dissipative dynamics. This section is composed by a brief introduction to quantum dissipation and by the derivation of two Born-Markovian master equations in the RWA and in the Floquet basis, which we solve in Sections 2.5 and 2.6 respectively. The conclusions and outlooks are drawn in Section 2.7. A brief introduction on Van Vleck theory is left to Appendix B as well as two derivations, which are connected but not directly related to the Duffing oscillator. These are the derivation of an effective single-particle Hamiltonian starting from the elasticity model for the nanoresonator and the derivation of a Born-Markovian master equation for a bichromatically driven anharmonic oscillator. They are included in Appendices A and C, respectively.

## 2.1 Introduction: Classical Duffing oscillator

Before investigating the dynamics of the quantum Duffing oscillator, which is in the focus of this chapter, we consider the corresponding classical oscillator (at zero temperature), the well-known Duffing oscillator [2–4]. It is characterized by the nonlinear equation of motion

$$m\ddot{\mathcal{X}} + m\gamma\dot{\mathcal{X}} + m\omega_1^2\mathcal{X} + \alpha\mathcal{X}^3 + f\mathcal{X}\cos\omega_{\text{ex}}t = 0 \quad (2.1)$$

and shows a rich variety of features including regular and chaotic motion. In this work, we focus on the parameter regime where only regular motion occurs. Moreover, we restrict to  $\alpha > 0$ . The nonlinear response of its amplitude  $A$  can be calculated perturbatively [2]. One obtains the response  $A(\omega_{\text{ex}})$  as the solution of the equation

$$\omega_{\text{ex}} - \omega_1 = \frac{3}{8}\frac{\alpha}{m\omega_1}A^2 \pm \left( \frac{f^2}{4m^2\omega_1^2A^2} - \frac{\gamma^2}{4} \right)^{1/2}. \quad (2.2)$$

Its characteristic form is shown in Fig. 2.1. For weak driving strengths, the response as a function of the driving frequency  $\omega_{\text{ex}}$  has the well-known form of the harmonic oscillator with the maximum at  $\omega_{\text{ex}} = \omega_1$ . For increasing driving strength, the resonance grows and bends away from the  $\omega_{\text{ex}} = \omega_1$ -axis towards larger frequencies (since  $\alpha > 0$ ). The locus of the maximal amplitudes is given by the parabola [2]  $\omega_{\text{ex}} - \omega_1 = \frac{3}{8}\frac{\alpha}{m\omega_1}A^2$ , which is often called the *backbone curve*. Most importantly, a bistability develops with two adjacent stable branches and one intermediate unstable branch. This bistability is connected with a hysteretic jump phenomenon which can be probed if the driving frequency  $\omega_{\text{ex}}$  is adiabatically increased or decreased. The hysteresis is maximal for zero temperature. At finite temperature, it is reduced since the particle can escape from the metastable local minimum to the adjacent global minimum via thermal hopping before the deterministic switching point is reached [41,42]. Note that for larger driving amplitudes, also bifurcations and period doublings can occur [2–4] which we do not address in the present work.

The nonlinear response of the phase  $\varphi$  can be determined perturbatively in a

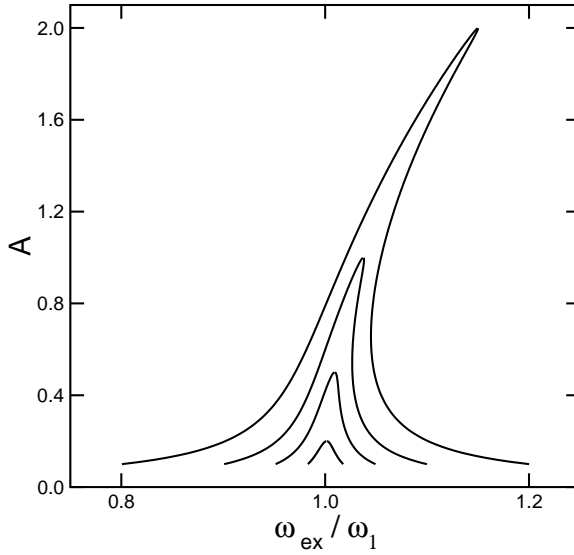


**Figure 2.1:** Classical response of the Duffing oscillator. For increasing driving strength, the harmonic Lorentzian peaks grows and bends, thereby defining a frequency region where three solutions are presents. In this regime the system is bistable since one of the three solutions is unstable.

similar way. One obtains [2]

$$\varphi(\omega_{\text{ex}}) = -\arctan \frac{\gamma A}{2 \left[ (\omega_{\text{ex}} - \omega_1) A - \frac{3}{8} \frac{\alpha A^3}{\omega_1} \right]}, \quad (2.3)$$

where  $A$  is the solution of Eq. (2.2). The curve  $\varphi(\omega_{\text{ex}})$  also has two stable branches with an unstable intermediate branch and displays similar hysteretic jump phenomena as the amplitude response.

As we will show in the following, the nonlinear response is qualitatively different in the corresponding quantum system. The discrete quasi-energy spectrum allows for multi-photon excitations which yield discrete resonances in the amplitude response profile. Moreover, the dynamically generated bistability allows for an escape of the system out of the metastable state via resonant quantum tunnelling. This generates characteristic resonances in the tunnelling rate when the external frequency  $\omega_{\text{ex}}$ , which plays the role of a control parameter, is tuned.

## 2.2 Experimental systems

The model of the quantum Duffing oscillator finds several realizations in experimental systems. Here, two are discussed in some details: (i) a doubly-clamped nanoresonator and (ii) the nonlinear response of a SQUID.

### 2.2.1 The mechanical nanoresonator

The experimental realization of nanobeams which show quantum mechanical behavior [43–47] is currently on the schedule of several research groups worldwide and poses a rather non-trivial task. Important key experiments on the way to this goal

have already been reported in the literature [48–60]. Most techniques to reveal the quantum behavior so far address the linear response in form of the amplitude of the transverse vibrations of the nanobeam around its eigenfrequency. The goal is to excite only a few energy quanta in a resonator held at low temperature. To measure the response, the ultimate goal of the experiments is to increase the resolution of the position measurement to the quantum limit [53, 59–62]. As the response of a damped linear quantum oscillator has the same simple Lorentzian shape as the one of a damped linear classical oscillator [63], a unique identification of the “quantum-ness” of a nanoresonator in the linear regime can sometimes be difficult.

No signatures of a quantum behavior in the nonlinear response of realized nanobeams have been reported up to present. One reason is that a nanomechanical resonator is exposed to a variety of intrinsic as well as extrinsic damping mechanisms depending on the details of the fabrication procedure, the experimental conditions and the used materials [64–66]. Possible extrinsic mechanisms include clamping losses due to the strain at the connections to the support structure, heating, coupling to higher vibrational modes, friction due to the surrounding gas, nonlinear effects, thermoelastic losses due to propagating acoustic waves, surface roughness, extrinsic noise sources, dislocations, and other material-dependent properties. An important internal mechanism is the interaction with localized crystal defects. Controlling this variety of damping sources is one of the major tasks to be solved to reveal quantum mechanical features. Recent measurement show that in the so far realized devices based on silicon and diamond structures, damping has been rather strong at low frequencies [64, 65] indicating even sub-Ohmic-type damping [63] which would make it difficult to observe quantum effects at all. However, using freely suspended carbon nanotubes instead could reduce damping at low frequencies due to the more regular structure of the long molecules which can be produced in a very clean manner. Further experimental work is required to clarify this point and to optimize the experimental conditions.

Nanoscale nonlinear resonators in the quantum regime have been investigated theoretically starting from microscopic models based on elasticity theory for the beam [12, 67, 68]. This model is presented in Appendix A.

### 2.2.2 The SQUID

Another system implementing the quantum Duffing oscillator model is a superconducting ring interrupted by a Josephson junction driven by means of an externally applied radio-frequency radiation (or alternatively a bias current). This system is known as superconducting quantum interference device (SQUID), because it can be used as an active element of a quantum interferometer measuring the superconducting phase.

The relevant macroscopic quantum observable for such devices is the total magnetic flux  $\Phi$  piercing the ring. It is given by  $\Phi = \phi_0 \varphi / 2\pi + n\phi_0$  in terms of the superconducting phase difference  $\varphi$  between the two junction interfaces and the flux quantum  $\phi_0$ .

In many cases such devices display an Ohmic dissipation in presence of a normal



current

$$V = RI_n \equiv R(I - I_s), \quad (2.4)$$

here, the Josephson supercurrent  $I_s$  is given by the Josephson relation  $I_s = I_c \sin \varphi$ . Since not all the charge that flows in the region of the junction is transported through it, a phenomenological description of the junction should include a finite capacitance  $C$ . Moreover, the ring has a geometrical self-inductance  $L$  due to the flux induced by a circulating current. The SQUID is thus equivalent to a phenomenological circuit. The applied current  $I_{\text{ex}}$  partly flows through the device as a supercurrent, partly as a normal current, partly is accumulated at the junction interfaces and partly is fed back by the geometrical inductance. Keeping in mind Faraday's law  $V = -\dot{\Phi}$ , one can straightforwardly derive the governing equation of motion

$$C\ddot{\Phi} + \frac{\dot{\Phi}}{R} + \frac{\Phi - \Phi_{\text{ex}}}{L} + \frac{I_c \phi_0}{2\pi} \sin\left(\frac{2\pi\Phi}{\phi_0}\right) = I_{\text{ex}}. \quad (2.5)$$

When the sinus is expanded keeping the first nonlinear term and a periodic driving is included by varying either the external flux  $\Phi_{\text{ex}}$  or the external current  $I_{\text{ex}}$  periodically, one recovers the Duffing equation.

The SQUID in this regime can be used for a resonant non-destructive read-out of a persistent current qubit [69–72]. In contrast to the conventional switching current measurement that generates unwanted quasi-particles when the dc-SQUID (acting as the qubit detector) switches to the voltage state, this technique keeps the SQUID biased along the supercurrent branch during the measurement. Thereby, the Josephson plasma resonance of the SQUID depends on the inductive coupling of the SQUID to the qubit. Measuring the plasma resonance allows to non-destructively read-out the qubit state. The application of this read-out technique in the nonlinear regime of the SQUID could allow for an improved sensitivity as well as its potential use as a nonlinear amplifier.

## 2.3 Coherent dynamics

In Section 2.2, we have presented two interesting candidates to implement the quantum Duffing oscillator (QDO) model. From now on, we will consider this generic model without focusing on a particular physical system.

We note that in the sequel the driven system will emit or absorb discrete quanta of energy, which we will refer to as *photons*. In the context of the mechanical resonator, however, no real photons are present but instead, phonons are the object of interest. This has to be kept in mind when applying the generic model to particular physical systems.

We start our investigation of the QDO considering the coherent dynamics of a nonlinear oscillator with mass  $m$  and coordinate  $\mathcal{X}$ . The corresponding Hamiltonian is

$$H_S(t) = \frac{\mathcal{P}^2}{2m} + \frac{m\omega_1^2}{2}\mathcal{X}^2 + \frac{\alpha}{4}\mathcal{X}^4 + \mathcal{X}f \cos(\omega_{\text{ex}}t). \quad (2.6)$$

Here,  $m$  and  $\omega_1$  are the mass and the harmonic frequency of the resonator, respectively, while  $\alpha$  gives the strength of the nonlinearity. We focus on the case  $\alpha > 0$  of hard non-linearities, where the undriven potential is monostable. The external driving is characterized by the amplitude  $f$  and the frequency  $\omega_{\text{ex}}$ . To proceed, we scale  $H_S(t)$  to dimensionless quantities such that the energies are in units of  $\hbar\omega_1$  while the lengths are scaled in units of  $x_0 \equiv \sqrt{\frac{\hbar}{m\omega_1}}$ . Put differently, we formally set  $m = \hbar = \omega_1 = 1$ . The nonlinearity parameter  $\alpha$  is scaled in units of  $\alpha_0 \equiv \hbar\omega_1/\mathcal{X}_0^4$ , while the driving amplitudes are given in units of  $f_0 \equiv \hbar\omega_1/x_0$ . For later purpose, we already mention that we scale temperature in units of  $T_0 \equiv \hbar\omega_1/k_B$  while the damping strengths are measured with respect to  $\omega_1$ .

### 2.3.1 Exact Floquet solution

A powerful tool to investigate the dynamical behavior of driven periodic systems is the Floquet theory. This is the analogue for time-periodic Hamiltonians of the well known Bloch theory for space-periodic Hamiltonians. In this subsection we will state the most important results of Floquet theory and apply them to our specific problem. For a systematic derivation of these result a useful reference is Ref. [73]. The central statement of Floquet theory is the Floquet theorem which is the analogue of the Bloch theorem: A periodic time dependent Schrödinger equation has a complete set  $\{|\psi_\alpha(t)\rangle\}$  of solutions such that each element of the basis can be expressed as

$$|\psi_\alpha(t)\rangle = e^{-i\varepsilon_\alpha t}|\phi_\alpha(t)\rangle \quad (2.7)$$

with the time-dependent vector  $|\phi_\alpha(t)\rangle$  being time-periodic with period  $T_{\omega_{\text{ex}}} = 2\pi/\omega_{\text{ex}}$ . This is a simple consequence of the invariance of the Schrödinger equation under discrete time translations  $-id/dt + H(t) = -id/dt + H(t + T_{\omega_{\text{ex}}})$ .  $\varepsilon_\alpha$  and  $|\phi_\alpha(t)\rangle$  are called Floquet or quasienergies and Floquet states, respectively, and follow from the solution of the eigenvalue equation

$$\mathcal{H}|\phi_\alpha(t)\rangle = \left[ H_S(t) - i\hbar \frac{\partial}{\partial t} \right] |\phi_\alpha(t)\rangle = \varepsilon_\alpha |\phi_\alpha(t)\rangle. \quad (2.8)$$

The linear operator  $\mathcal{H}$  is usually called Floquet Hamiltonian. The identification of  $\mathcal{H}$  as an Hamiltonian operator is justified by two strong motivations:

(i) The above equation is formally equivalent to a time-independent Schrödinger equation,  $\mathcal{H}$  being the Hermitian operator which determines the quasienergies and the Floquet states. The corresponding Hilbert space is the vector product  $\mathcal{R} \otimes \mathcal{T}$  of the original Hilbert space  $\mathcal{R}$  and the Hilbert space of the time-periodic functions  $\mathcal{T}$ . An inner product in  $\mathcal{T}$  is defined by

$$(f, g) = \frac{1}{T_{\omega_{\text{ex}}}} \int_0^{T_{\omega_{\text{ex}}}} dt f^*(t)g(t).$$

The most simple basis  $\{|n_\tau\rangle\}$  of orthonormalized vectors for this space is the set of vectors defined by  $\langle t|n_\tau\rangle = \exp[-in\omega_{\text{ex}}t]$ , where  $n$  is an integer. We can write the

Floquet Hamiltonian  $\mathcal{H}$  in this basis as

$$\mathcal{H}_{nn'} = (H_0 - n\omega_{\text{ex}})\delta_{nn'} + \frac{f}{2}\mathcal{X}(\delta_{nn'+1} + \delta_{nn'-1}), \quad (2.9)$$

with the undriven Hamiltonian  $H_0 = \mathcal{P}^2/(2m) + (m\omega_1^2/2)\mathcal{X}^2 + (\alpha/4)\mathcal{X}^4$ .

(ii) The Floquet Hamiltonian can be derived starting from the Hamiltonian  $H_{SB} = H_S + \omega_{\text{ex}}b^\dagger b + f/(2n_0^{1/2})\mathcal{X}(b + b^\dagger)$  describing the system Hamiltonian linearly coupled to a boson degree of freedom. If all the states relevant for the dynamics have photon number  $n + n_0$  with  $|n| \ll n_0$ , i.e only few photons are exchanged between the oscillator and the driving field compared to the average photon number  $n_0$ , one obtains the Floquet Hamiltonian in Eq. (2.9) by neglecting the terms of order  $\mathcal{O}(n_0^{-1/2})$  in  $H_{SB}$ . Thus, the additional degree of freedom can be interpreted as the number of photon exchanged. The Schrödinger equation of the Floquet Hamiltonian in the extended Hilbert space  $\mathcal{R} \otimes \mathcal{T}$  yields the same mean values for the oscillator observables as the Schrödinger equation for the time dependent Hamiltonian in Eq. (2.6) in the system Hilbert space  $\mathcal{H}$  once an initial coherent state with very large average photon number  $n_0$  is assumed for the boson degree of freedom [73].

In analogy with the quasimomenta in Bloch theory, the quasienergies  $\varepsilon_\alpha$  are defined up to a multiple integer of  $\omega_{\text{ex}}$ . In fact, the state  $|\phi_\alpha^{(n)}(t)\rangle = e^{in\omega_{\text{ex}}t}|\phi_\alpha(t)\rangle$  is also an eigenstate of the Floquet Hamiltonian, but with the eigenvalue  $\varepsilon_{\alpha,n} = \varepsilon_\alpha + n\omega_{\text{ex}}$ . However these two Floquet states correspond to the same solution  $|\psi_\alpha(t)\rangle$  of the Schrödinger equation. Hence, the spectrum of the Floquet Hamiltonian has a Brillouin zone structure, each Brillouin zone being of size  $\omega_{\text{ex}}$ . Moreover, in order to find a complete set  $\{|\psi_\alpha(t)\rangle\}$  of solutions, it is sufficient to consider only those Floquet states which lie within a single Brillouin zone, for example  $-\omega_{\text{ex}}/2 \leq \varepsilon < \omega_{\text{ex}}/2$ . Due to the Brillouin zone structure the quasienergies do not allow for global ordering. This, however, can be achieved with the mean energies obtained after averaging over one driving period, i.e.,

$$\overline{E}_\alpha = \frac{1}{T_{\omega_{\text{ex}}}} \int_0^{T_{\omega_{\text{ex}}}} dt \langle \psi_\alpha(t) | H(t) | \psi_\alpha(t) \rangle = \sum_n (\varepsilon_\alpha + n\omega_{\text{ex}}) \langle \hat{\phi}_{\alpha,n} | \hat{\phi}_{\alpha,n} \rangle, \quad (2.10)$$

with the Fourier components of the Floquet states

$$|\hat{\phi}_{\alpha,n}\rangle = \frac{1}{T_{\omega_{\text{ex}}}} \int_0^{T_{\omega_{\text{ex}}}} dt e^{in\omega_{\text{ex}}t} |\phi_\alpha(t)\rangle. \quad (2.11)$$

The eigenvalue equation (2.8) can be solved numerically by using the representation in Eq. (2.9). One has to approximate the Hilbert space  $\mathcal{R} \otimes \mathcal{T}$  by considering the subspace spanned by the first  $\mathcal{N}$  eigenstates of the undriven Hamiltonian  $H_0$  and by the  $2\mathcal{M} + 1$  vectors  $|n_\tau\rangle$  corresponding to  $n = -\mathcal{M}, -\mathcal{M} + 1, \dots, \mathcal{M} - 1, \mathcal{M}$ . Thus the dimension of the Floquet matrix is  $\mathcal{N}(2\mathcal{M} + 1)$  and the computational effort is proportional to  $[\mathcal{N}(2\mathcal{M} + 1)]^3$ .

### 2.3.2 Rotating wave approximation (RWA)

The Floquet solution presented in the previous subsection has the advantage of being exact. Thereby it allows a numerical solution for rather strong driving strengths  $f$

and nonlinearities  $\alpha$ . In this section we will present an alternative approximate solution valid for weak anharmonicity  $\alpha \ll \omega_1$ , weak driving  $f \ll \alpha$  and close to the fundamental resonance  $|\omega_{\text{ex}} - \omega_1| \ll \omega_1$ . This approach has the advantage to yield simple analytical results that shed light on the physical picture for the nonlinear oscillator. In particular we will derive a quasi-potential which is at the origin of the bistability of the classical Duffing oscillator. For convenience, we switch to a representation in terms of creation and annihilation operators  $a$  and  $a^\dagger$ , such that  $\mathcal{X} = x_0(a + a^\dagger)/\sqrt{2}$ . Moreover, we switch to the rotating frame by performing the canonical transformation  $R = \exp[i\omega_{\text{ex}}a^\dagger at]$ . The RWA consists in eliminating all the fast oscillating terms from the transformed Hamiltonian. Thereby, one obtains the Schrödinger equation in the rotating frame

$$\tilde{H}|\varphi_\alpha\rangle = \varepsilon_\alpha|\varphi_\alpha\rangle, \quad (2.12)$$

with the Hamiltonian in the RWA

$$\tilde{H} = \tilde{\omega}\hat{n} + \frac{\nu}{2}\hat{n}(\hat{n} + 1) + \mu(a + a^\dagger). \quad (2.13)$$

Here, we have introduced the detuning  $\tilde{\omega} = \omega_1 - \omega_{\text{ex}}$ , the nonlinearity parameter  $\nu = 3\alpha/(4m^2\omega_1^2)$ , the driving strength  $\mu = (x_0/2^{3/2})f$  and  $\hat{n} = a^\dagger a$ . By projecting onto the harmonic oscillator basis, we get

$$\tilde{H}_{nn'} = \left(\tilde{\omega}n + \frac{\nu}{2}n(n+1)\right)\delta_{nn'} + \mu\left(\sqrt{n+1}\delta_{nn'-1} + \sqrt{n}\delta_{nn'+1}\right). \quad (2.14)$$

In the static frame, an orthonormal (at equal times) set  $\{|\psi_\alpha(t)\rangle\}$  of approximate solutions of the Schrödinger equations follows as

$$|\psi_\alpha(t)\rangle \simeq e^{-i\varepsilon_\alpha t}e^{-i\omega_{\text{ex}}a^\dagger at}|\varphi_\alpha\rangle. \quad (2.15)$$

Since  $\exp[-i\omega_{\text{ex}}a^\dagger at]|\varphi_\alpha\rangle$  is  $T_{\omega_{\text{ex}}}$ -periodic, the solutions in the previous equation have the form predicted by the Floquet theorem in Eq. (2.7). Within the limit of validity of the RWA, we can thus identify  $\varepsilon_\alpha$  and  $\exp[-i\omega_{\text{ex}}a^\dagger at]|\varphi_\alpha\rangle$  with the Floquet quasi-energies and the Floquet states  $|\phi_\alpha(t)\rangle$ , respectively. It is instructive to derive directly Eq. (2.12) from the defining eigenvalue equation (2.8) of the previous section. One has to make the following steps:

- (i) Approximate the undriven Hamiltonian  $H_0$  in Eq. (2.9) with its first order expansion in  $\alpha$ ,  $H_0 \simeq \omega\hat{n} + (\nu/2)\hat{n}(\hat{n} + 1)$
- (ii) Neglect in the driving term the contributions  $\mu(a\delta_{nn'+1} + a^\dagger\delta_{nn'-1})$
- (iii) Project  $\mathcal{H}$  onto the set  $\{|n\rangle \otimes |m_\tau\rangle\}$ .

Then the Floquet Hamiltonian is block-diagonal, each block corresponding to the subspace spanned by the subset  $\{|n\rangle \otimes |m_\tau \equiv n + m\rangle\}$ , with  $m$  a fixed integer. Moreover, the block corresponding to  $m = 0$  can be identified with the approximated Hamiltonian in the rotating frame  $\tilde{H}$ , since  $\mathcal{H}_{nn,nn} = \tilde{H}_{nn}$ . The RWA is thus equivalent to the approximation (i) and (ii).

We have performed the transformation to the rotating frame because it would have been difficult to justify (ii) in the framework of Floquet theory. As already

mentioned at the beginning of this subsection, another remarkable advantage of a transformation to the rotating frame is that it is possible to derive the quasipotential which is at the origin of the classical bistability of the Duffing oscillator. Following Ref. [6] we introduce the reduced coordinate and momentum of the oscillator in the rotating frame

$$\mathcal{X}_r = \left(\frac{\nu}{4\tilde{\omega}}\right)^{1/2} (a^\dagger + a), \quad \mathcal{P}_r = \left(\frac{i\nu}{4\tilde{\omega}}\right)^{1/2} (a^\dagger - a) \quad (2.16)$$

with the commutator  $[\mathcal{X}_r, \mathcal{P}_r] = -i\lambda$ ,  $\lambda = \nu/(2\tilde{\omega})$ . By substituting into Eq. (2.13), one obtains

$$\tilde{H} = \frac{\tilde{\omega}^2}{2\nu} \left[ (\mathcal{X}_r^2 + \mathcal{P}_r^2 - 1)^2 - \beta^{1/2} \mathcal{X}_r \right] + \mathcal{O}(\lambda) \quad (2.17)$$

with  $\beta = 4\mu^2\nu/\tilde{\omega}^3$ . The quasipotential is sketched in Fig. 2.2. It has the shape of a tilted Mexican hat. Its minimum and local maximum correspond to the classical stable states of the forced vibration. They coexist for  $0 < \beta < 16/27$ . For such  $\beta$  in a certain range of quasienergies, there are two Hamiltonian trajectories corresponding to the same quasi-energy, one on the internal part of the surface and the other on the external one. When the motion is quantized, and two levels, corresponding to an internal and an external trajectory respectively, coincide, many of them will coincide pairwise [5, 6].

For zero driving strength one can easily identify these trajectories with the eigenstates of the undriven Hamiltonian  $H_0$  in the rotating frame (see Eq. (2.13) with  $\mu = 0$ ): the harmonic oscillator states  $|n\rangle$ . In fact, for  $\tilde{\omega} = -\nu(N+1)/2$  ( $N$  positive integer), corresponding to  $\omega_{\text{ex}} = \omega_1 + \nu(N+1)/2 \equiv \omega_N$ , we have  $\varepsilon_{N-n} = \varepsilon_n$  for  $n \leq N$ .

For a finite driving strength  $\mu > 0$ , the exact crossings turn into avoided crossings which is a signature of multiphoton transitions [5, 6, 12] as we shall explain at the end of this section. A typical quasienergy spectrum is shown in Fig. 2.3 for the parameters  $\nu = 10^{-3}$  and  $\mu = 10^{-4}$ . The dashed vertical lines indicate the multiple avoided level crossings which occur all for the same driving frequency.

The dynamics of the QDO near the multiple avoided level crossings can be understood by means of a perturbative approach, with the small parameter  $\varepsilon$  defined as

$$\varepsilon = \frac{2\mu}{\nu(N+1)}. \quad (2.18)$$

For  $\varepsilon \ll 1$  and  $\omega_{\text{ex}} \simeq \omega_N$ , each pair of degenerate levels interacts only weakly with the other levels, and acts effectively like a two-level Rabi system [5]. The Rabi frequency is equal to the minimal splitting of the levels. In the following, we diagonalize the RWA Hamiltonian near the multiphoton resonances perturbatively, with  $\varepsilon$  as a small parameter.

Let us therefore consider the multiphoton resonance at  $\tilde{\omega} = -\nu(N+1)/2$ . In addition, we are interested in the response around the resonance and therefore introduce the small deviation  $\Delta$ . We formally rewrite  $\tilde{H}$  as

$$\tilde{H} = \frac{\nu(N+1)}{2} \left[ -(1 + \Delta)\hat{n} + \frac{\hat{n} + 1}{N+1}\hat{n} + \varepsilon(a + a^\dagger) \right]. \quad (2.19)$$

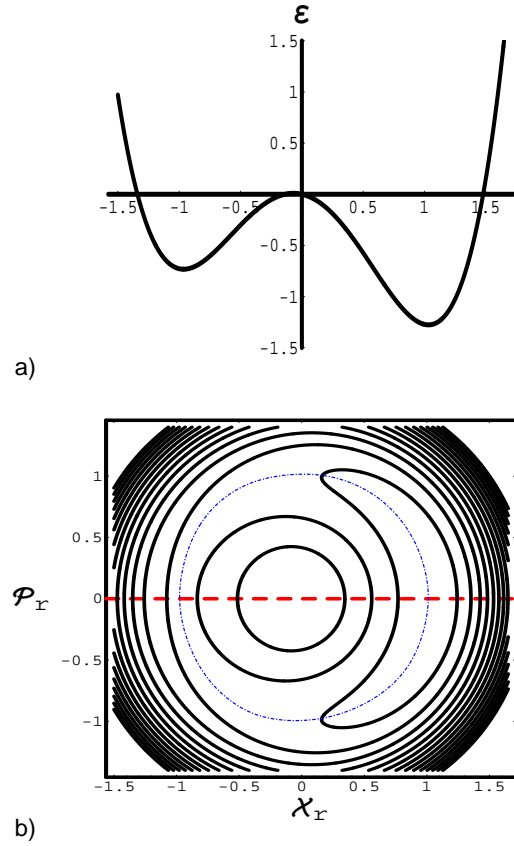


**Figure 2.2:** Quasipotential for the driven nonlinear oscillator. The quasienergy is measured in unit of  $\tilde{\omega}^2/2\nu$  and  $\beta = 2/27$ . (a) shows a cut along  $P_r = 0$  through the contour plot shown in (b), see horizontal dashed line. The 1D cut displays (from left to right) a relative minimum, a relative maximum and the absolute minimum. They correspond to a saddle point, a relative maximum and the absolute minimum of the complete 2D potential, respectively. The surface of the potential is divided into an internal and an external dome. In the contour plot are visible: i) The border of the two domes, passing through the saddle point and the absolute minimum (dotted-dashed line) ii) one trajectory around the minimum of the quasipotential, iii) two trajectories on the internal dome of the potential, iv) several trajectories on the external part. The most and the second most internal trajectory on the external dome have the same quasi-energy as the most external and the most internal trajectory on the internal part, respectively.

Let us then first discuss the dynamics at resonance ( $\Delta = 0$ ). We divide it in the unperturbed part  $H_0$  and the perturbation  $\varepsilon V$  according to

$$H_0 = \frac{\nu(N+1)}{2} \left[ -\hat{n} + \frac{\hat{n}+1}{N+1} \hat{n} \right], \quad V = \frac{\nu(N+1)}{2} [a + a^\dagger], \quad (2.20)$$

respectively. The unperturbed Hamiltonian is diagonal and near the resonance its spectrum is divided in well separated groups of nearly degenerate quasienergy eigenvalues.

An appropriate perturbative method to diagonalize this type of Hamiltonian is the Van Vleck perturbation theory [74–76]. A brief introduction to this formalism is included in Appendix B. The central idea behind the Van Vleck formalism is that it is possible to define a unitary transformation yielding the Hamiltonian  $\tilde{H}$  in an effective block diagonal form. The effective Hamiltonian has the same eigenvalues

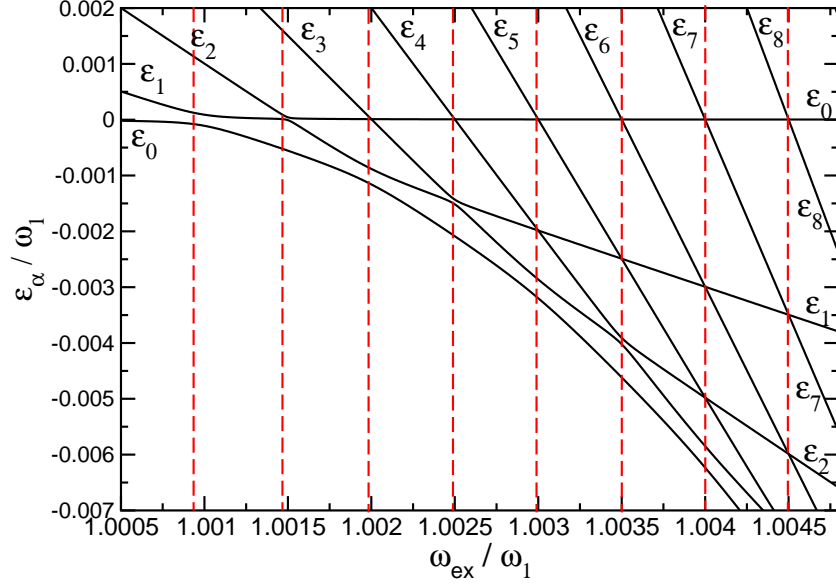


**Figure 2.3:** Typical quasienergy spectrum  $\varepsilon_\alpha$  for increasing driving frequency  $\omega_{\text{ex}}$  for the case  $\nu = 10^{-3}$  and  $\mu = 10^{-4}$ . The vertical dashed lines indicate the multiple avoided level crossings for a fixed driving frequency.

as the original one, with the quasi-degenerate eigenvalues in a common block. It can be written as

$$\tilde{H}' = e^{iS} \tilde{H} e^{-iS}. \quad (2.21)$$

In our case, each block is a two by two matrix corresponding to a subspace formed by a couple of quasienergy states forming an anticrossing. Let us consider the effective Hamiltonian  $H'_n$  corresponding to the involved levels  $|n\rangle$  and  $|N-n\rangle$ , being eigenstates of the harmonic oscillator. The degeneracy in the corresponding block is lifted at order  $N - 2n$  in Van Vleck perturbation theory. The block Hamiltonian then reads <sup>1</sup>

$$\tilde{H}'_n = \begin{pmatrix} \frac{\nu}{2} n(n-N) & \varepsilon^{N-2n} C_{12,N-2n} \\ \varepsilon^{N-2n} C_{12,N-2n} & \frac{\nu}{2} n(n-N) \end{pmatrix}, \quad (2.22)$$

where

$$C_{12,N-2n} = (N+1)^{N-2n} \frac{\nu}{2} \frac{\sqrt{(N-n)!}}{\sqrt{n!}(N-2n-1)!^2}. \quad (2.23)$$

This is the lowest order of the perturbed Hamiltonian which allows to calculate the corresponding zeroth order eigenstates. By diagonalizing  $\tilde{H}'_n$  in Eq. (2.22), one finds

<sup>1</sup>see Appendix B for the derivation of this formula

the minimal splitting for the  $N$ -photon transition as

$$\begin{aligned}\Omega_{N,n} &= |2\varepsilon^{N-2n}C_{12,N-2n}| \\ &= 2\mu \left(\frac{2\mu}{\nu}\right)^{N-2n-1} \frac{\sqrt{(N-n)!}}{\sqrt{n!}(N-2n-1)!^2}.\end{aligned}\quad (2.24)$$

For the case away from the  $N$ -th resonance, we consider a detuning  $\Delta = \varepsilon^N \delta$ . Within the Van Vleck technique, only the zero-th block is influenced according to

$$\tilde{H}'_0 = \begin{pmatrix} 0 & \varepsilon^N C_{12,N} \\ \varepsilon^N C_{12,N} & -\frac{\nu(N+1)}{2}\varepsilon^N N\delta \end{pmatrix}, \quad (2.25)$$

the other blocks given in Eq. (2.22) for  $n \neq 0$  are not influenced by this higher-order correction. The eigenvectors for the Hamiltonian  $\tilde{H}$  at zero-th order are obtained by diagonalizing  $\tilde{H}'_0$  in Eq. (2.22). One finds  $|\varphi_n\rangle = |n\rangle$  for  $n \geq N+1$  or  $|\varphi_n\rangle = (|n\rangle + |N-n\rangle)/\sqrt{2}$  and  $|\varphi_{N-n}\rangle = (|n\rangle - |N-n\rangle)/\sqrt{2}$  for  $0 < n < N/2$  and  $|\phi_{N/2}\rangle = |N/2\rangle$  if  $N$  is even. Moreover,

$$\begin{aligned}|\varphi_0\rangle &= \cos\frac{\theta}{2}|0\rangle - \sin\frac{\theta}{2}|N\rangle, \\ |\varphi_N\rangle &= \sin\frac{\theta}{2}|0\rangle + \cos\frac{\theta}{2}|N\rangle,\end{aligned}\quad (2.26)$$

where we have introduced the angle  $\theta$  via

$$\tan\theta = -2\Omega_{N,0}/[\nu(N+1)N\Delta] = -\Omega_{N,0}/[\omega_{\text{ex}} - \omega_N]. \quad (2.27)$$

Note that the Rabi frequency  $\Omega_{N,n}$  sets the width of the corresponding multiphoton resonance.

To conclude this section, let us discuss the physical interpretation of the multiphoton transitions and the corresponding Rabi frequencies: The system initially prepared in the state  $|n \leq N\rangle$  in presence of a driving field with resonant frequency  $\omega_{\text{ex}} = \omega_N$  switches continuously between the pair of states  $|n\rangle$  and  $|N-n\rangle$ . The time scale of these virtual processes is set by the Rabi frequency  $\Omega_{N,n}$ . According to the discussion in Section 2.3.1, the transition between different oscillator states are due to the fluctuations of the photon number in the driving field. Within the limit of validity of the RWA approximation, the virtual transition between the states  $|n\rangle$  and  $|N-n\rangle$  is accompanied by the absorption of exactly  $N-n$  photons from the field. For this reason, such transitions are denominated multiphoton transitions as already anticipated above. In the following we will refer to them also as multiple multiphoton transitions, since, when the system is prepared in a generic state, there is a multiphoton transition for each pair of quasidegenerate levels.

## 2.4 Dissipative dynamics

In the previous section we have described extensively the coherent dynamics of the driven nonlinear oscillator. Within the RWA, the Hamiltonian of the system



can be described in terms of a quasipotential. As a consequence of the particular shape of the potential (a tilted Mexican hat), in a certain quasienergy range, there are two classical orbits corresponding to the same quasienergy. In the classical Duffing oscillator (which also comprises a dissipative force), this feature leads to bistability. Canonical quantization of the RWA Hamiltonian  $\tilde{H}$  leads to degenerate multiphoton tunnelling transitions. It remains to be investigated what is the effect of dissipation in the quantum system. In this section we will briefly present the theoretical formalism necessary to describe dissipation in the framework of a fully quantum mechanical analysis. For simplicity, we will often restrict the discussion to the particular system we are investigating. For a more general and comprehensive review on the subject, see Ref. [63].

Classically, dissipation can be introduced phenomenologically, by adding a velocity proportional force. In principle, it could be possible to incorporate this model in a Lagrangian description. However this approach leads to unphysical properties when attempting a canonical quantization [63]. The most successful approach to dissipation, consistent with the fundamental laws of quantum mechanics, is based on the coupling of a system with external degrees of freedom, the so-called system-bath model [63, 77–90]. It is possible to show that this model leads to a Langevin-type equation with a memory-friction force and an operator valued random force. Moreover it obeys the Ehrenfest theorem: The Heisenberg equations of motion for the canonical operators associated to the bath and system coordinates and momenta are formally equivalent to the classical equations of motion for the corresponding classical variables. However, due to the non-linear contribution to the system potential, the mean values of the system coordinate and momentum do not obey the classical equations of motion. For this reason, we expect to find a signature of the quantum-mechanical nature of such a system, even at equilibrium and after averaging out quantum fluctuations.

An approach, alternative to the Langevin equation, to the quantum dynamics of the central system is possible in the framework of the path integral formalism. This consists in formally eliminating the bath degrees of freedom and describing their influence on the system in term of a functional, the so-called Feynman Vernon influence functional [81]. This approach enabled the investigation of dissipative quantum system beyond the weak coupling limit. Unfortunately, it has the drawback of being rather involved. As soon as non-linear force come into play, one has to resort to sophisticated numerical treatments, such as quantum Monte-Carlo calculations [91] or, alternatively, deterministic iterative real-time path integral simulations with the QUAPI approach [92, 93]. However in the deep quantum limit we are interested in, which corresponds to a weak coupling to the bath, a perturbative approach is appropriate. This leads to a Markovian master equation (MME) for the reduced density matrix [94, 95]. At the end of the section we will show how to combine the MME with Floquet theory in the spirit of Ref. [96]. When the RWA is applied in addition, a rather simple dynamical equation follows.

### 2.4.1 The system-bath model and the Langevin equation

In order to model dissipation, we will use the simplest system-bath model, consisting in a set of harmonic oscillators coupled bilinearly to the system. This choice might appear arbitrary. The most obvious motivation for this common approach, is that it allows analytical progress and compact formulae. Most importantly, in the weak coupling and low-temperature limit we are interested in, the physics will not depend on the structure of the bath (as long as it has a smooth frequency distribution). As it will be clear from the discussion, in this limit, the bath will be characterized by only two phenomenological parameters, the damping strength  $\gamma$  and the temperature  $T$ .

The total Hamiltonian of the system plus bath is given by

$$H(t) = H_S(t) + H_B + H_{SB}, \quad (2.28)$$

where

$$H_B = \sum_{j=1}^{\mathcal{N}} \frac{1}{2} \left[ \frac{p_j^2}{m_j} + m_j \omega_j^2 x_j^2 \right], \quad (2.29)$$

$$H_{SB} = -\mathcal{X} \sum_j c_j x_j + \mathcal{X}^2 \sum_j \frac{c_j^2}{2m_j \omega_j^2}. \quad (2.30)$$

are the bath Hamiltonian and its coupling to the system, respectively. They represent an ensemble of  $\mathcal{N}$  harmonic oscillators of masses  $m_j$  with coordinate and momentum operators  $x_j$  and  $p_j$  and oscillation frequencies  $\omega_j$ . The coupling of the system to the bath is assumed to be linear both in the bath oscillator coordinates  $x_j$  and in the system coordinate  $\mathcal{X}$ . The strength of the coupling is given by the coupling constants  $c_j$ . In Eq. (2.30), the additional potential term proportional to  $\mathcal{X}^2$  is introduced in order to cancel a renormalization of the potential  $V(\mathcal{X}, t)$ , which arises due to the linear coupling of the system to the bath [63] (counter term).

The Hamiltonian equations of motion for the system plus bath read

$$m\ddot{\mathcal{X}} + m\omega_1^2 \mathcal{X} + \alpha \mathcal{X}^3 + f \cos \omega_{\text{ext}} t + \mathcal{X} \sum_{j=1}^{\mathcal{N}} \frac{c_j^2}{m_j \omega_j^2} = \sum_{j=1}^{\mathcal{N}} c_j x_j, \quad (2.31)$$

$$m_j \ddot{x}_j + m_j \omega_j^2 x_j = c_j \mathcal{X}, \quad j = 1, \dots, \mathcal{N}. \quad (2.32)$$

Note that at this stage is not yet necessary to distinguish between classical coordinates and momenta, and the corresponding quantum operators. Ehrensfest theorem assures us that the classical and the Heisenberg quantum equations of motion are formally equivalent. The equations for the harmonic oscillator configurations are second order linear differential equations. They can be readily solved in terms of the system configuration  $\mathcal{X}$  and the time  $t$ . By substituting the solutions into the equation for  $\mathcal{X}$ , we get the Langevin-type equation

$$\ddot{\mathcal{X}} + \int_0^t ds \gamma(t-s) \dot{\mathcal{X}} + \omega_1^2 \mathcal{X} + \frac{\alpha}{m} \mathcal{X}^3 + \frac{f}{m} \cos \omega_{\text{ext}} t = \frac{1}{m} \xi(t). \quad (2.33)$$

On the righthand side of this equation we have neglected the transient term  $-\gamma(t)\mathcal{X}^{(0)}$ , which depends on the initial configuration of the system  $\mathcal{X}^{(0)}$ . Moreover, we have introduced the *memory-friction kernel*

$$\gamma(t) = \frac{\Theta(t)}{m} \sum_{j=1}^{\mathcal{N}} \frac{c_j^2}{m_j \omega_j^2} \cos \omega_j t, \quad (2.34)$$

and the time-dependent force

$$\xi(t) = \sum_{j=1}^{\mathcal{N}} c_j \left[ x_j^{(0)} \cos \omega_j t + \frac{p_j^{(0)}}{m_j \omega_j} \sin \omega_j t \right]. \quad (2.35)$$

The latter can be regarded as a stochastic force since the initial values  $x_j^{(0)}$  and  $p_j^{(0)}$  are drawn from an initial thermal distribution.

In the following, we (i) assume that the bath is in equilibrium with a (not further specified) superbath at temperature  $T$  and (ii) neglect the initial correlations between the system and the bath. At this stage, we have to distinguish between the classical and the quantum case. In the classical case, we expect the position and momentum of the system to assume the initial values  $\mathcal{X}^{(0)}$  and  $\mathcal{P}^{(0)}$ , whereas the bath coordinates and momenta are described by the classical Boltzmann distribution

$$\varrho_B^{(0)} = Z^{-1} \exp \left[ -\beta \sum_j \left( \frac{p_j^{(0)2}}{2m_j} + \frac{m_j \omega_j^2}{2} x_j^{(0)2} \right) \right]. \quad (2.36)$$

In this case, the force  $\xi(t)$  becomes a fluctuating force with colored noise and Gaussian statistical properties

$$\langle \xi(t) \rangle = 0, \quad \langle \xi(t) \xi(t') \rangle = m k_B T \gamma(t - t'). \quad (2.37)$$

The second relation is the classical fluctuation-dissipation theorem. For the quantum case, the assumption (i) and the approximation (ii) imply that the density operator  $W(t)$  of the system-plus-bath at initial time  $t = 0$  factorizes according to

$$W(0) = \rho_S(0) \otimes \frac{e^{-H_B/k_B T}}{\text{tr } e^{-H_B/k_B T}}. \quad (2.38)$$

where  $\rho_S(0)$  is the density operator of the system at time 0. The influence of the fluctuating force on the system is fully characterized by its symmetric autocorrelation function, the *noise kernel*

$$K(t - t') = \frac{1}{2} \langle [\xi(t), \xi(t')]_+ \rangle = \frac{1}{2} \sum_{j=1}^{\mathcal{N}} \frac{c_j^2}{m_j \omega_j} \coth \frac{\omega_j \beta}{2} \cos \omega_j (t - t'). \quad (2.39)$$

Note that in this case, the fluctuating force is operator-valued and the average has to be intended on both the quantum and the thermal fluctuations.

It is now convenient to introduce the *spectral density* of the bath mode, defined as

$$J(\omega) = \frac{\pi}{2} \sum_{j=1}^{\mathcal{N}} \frac{c_j^2}{m_j \omega_j} \delta(\omega - \omega_j). \quad (2.40)$$

We can then express the friction and the noise kernel in terms of the spectral density as

$$\gamma(t) = \Theta(t) \frac{2}{\pi m} \int_0^\infty d\omega \frac{J(\omega)}{\omega} \cos \omega t, \quad (2.41)$$

$$K(t) = \frac{1}{\pi} \int_0^\infty d\omega J(\omega) \coth \frac{\omega \beta}{2} \cos \omega t. \quad (2.42)$$

The two kernels are not independent since they obey the second fluctuation-dissipation theorem, which in Fourier representation reads

$$\hat{K}(\omega) + \hat{K}(-\omega) = m\omega \operatorname{Re}[\hat{\gamma}(\omega)] \coth \frac{\omega \beta}{2}. \quad (2.43)$$

Before continuing the discussion about the Langevin equation, we make a few remarks on the spectral density  $J(\omega)$ . For a small number  $\mathcal{N}$  of bath oscillators, the time on which the transferred energy is fed back to the system is of the order of other relevant time scales. However already for  $\mathcal{N} = 20$  this Poincaré recurrence time results to be very large. Hence, any realistic bath can be described in terms of an infinite number of degrees of freedom. In this continuum limit  $J(\omega)$  will be a smooth function. Throughout this work, we will consider the case in which  $J(\omega)$  has a power-law form with an exponential cut-off

$$J(\omega) = m\gamma_s \frac{\omega^s}{\omega_1^{s-1}} e^{-\omega/\omega_c} \quad (2.44)$$

The case  $s = 1$  (when also the cut-off is sent to infinity) correspond to a memoryless friction and a white noise (in the classical limit)

$$\gamma(t) = 2\gamma_1 \delta(t) \quad (2.45)$$

The damping term in the Langevin equation (2.33) becomes  $\gamma_s \dot{\mathcal{X}}$ . In the literature, due to the formal analogy to Ohm's law, such a bath is referred as to an *Ohmic* bath. The cases  $0 < s < 1$  and  $s > 1$  have been popularized as *sub-Ohmic* and *super-Ohmic* respectively.

We close this subsection commenting on the connection between the quantum and the classical Langevin equation. We start from the observation that, for  $\omega \ll k_B T$ , the second fluctuation-dissipation theorem in Eq. (2.43) reduce to its classical analogous in Eq. (2.37). Hence in the long-time limit, the quantum Langevin equation is formally equivalent to the classical Langevin equation. When considering the damped harmonic oscillator (corresponding to  $\alpha = 0$ ), it is even possible to go a step further: the mean value of the position operator obeys the classical

equation of motion, as can be easily seen by taking the average on the quantum fluctuations in Eq. (2.33). This does not hold anymore for the nonlinear damped oscillator. To illustrate this, let us consider low temperature. In this limit, the thermal fluctuations are strongly suppressed. As a consequence, in the classical case, we can conclude that  $\langle \mathcal{X}^3 \rangle \simeq \langle \mathcal{X} \rangle^3$  and that the Langevin equation (2.33) yields the Duffing equation in Eq. (2.1)<sup>2</sup>. This is not valid in the quantum limit: Due to quantum fluctuations  $\langle \mathcal{X}^3 \rangle \neq \langle \mathcal{X} \rangle^3$  even at very low temperature and the mean value for the system coordinate  $\langle \mathcal{X} \rangle$  does not obey the classical Duffing equation of motion.

### 2.4.2 The influence functional and the Markovian master equation (MME)

In the previous subsection, we have shown that the mean value of the position operator of a nonlinear damped quantum oscillator, unlike its harmonic counterpart, does not obey the classical equation of motion. This implies that a signature of the underlying quantum nature of the system can be discerned in the response of the oscillator even at equilibrium and when a measurement scheme is used, which averages over the quantum fluctuations. Moreover, since it is not possible to derive a simple differential equation for the mean value of the position operator  $\langle \mathcal{X} \rangle$ , one should solve the quantum Langevin equation (2.33) describing the time evolution in the Heisenberg picture of the corresponding operator  $\mathcal{X}$ . Such an approach appears to be hopeless: It is usually challenging to solve a differential nonlinear equation, the stochastic and operatorial nature of the quantum Langevin equation renders exceedingly difficult even a numerical treatment of the problem. For this reason in the following we will pursue a different approach based on a formalism developed by Feynman and Vernon, leading, in the weak coupling limit, to a simple linear equation for the reduced density matrix, the so-called Markovian master equation (MME).

In their original paper in 1963 [81], Feynman and Vernon use Feynman's real-time path integral formulation to calculate the behavior of the central system of interest, which is coupled to other external quantum systems, in terms of its own variables only. Feynman and Vernon derive the elegant general result that the effect of the external systems can always be included in a general class of functionals of the coordinates of the central system only, the so-called *influence functionals*. This finding is now applied to the situation where the nonlinear oscillator is coupled bilinearly to a bath of harmonic oscillators. Due to the linear coupling to a harmonic bath, a closed expression for the influence functional can be derived.

To this end, we introduce the shorthand notation  $\mathbf{x} = \{x_j\}$ ,  $j = 1, \dots, \mathcal{N}$ , for the bath oscillator coordinates and write down the full density operator  $W(t)$  at time  $t$

---

<sup>2</sup>Strictly speaking, we recover Eq. (2.1), when also an Ohmic bath is considered. However, a qualitatively similar response is expected at equilibrium in presence of a sub-Ohmic or super-Ohmic environment, the major difference with respect to the Ohmic case being a  $\omega_{\text{ex}}$ -dependence of the damping strength, which might not be detected in a narrow interval around the resonant frequency.

in coordinate representation. It yields

$$\begin{aligned} \langle \mathcal{X}_f \mathbf{x}_f | W(t) | \mathcal{X}'_f \mathbf{x}'_f \rangle &= \langle \mathcal{X}_f \mathbf{x}_f | U(t, 0) W(0) U^{-1}(t, 0) | \mathcal{X}'_f \mathbf{x}'_f \rangle \\ &= \int d\mathcal{X}_i d\mathcal{X}'_i \prod_{j=1}^{\mathcal{N}} dx_{j,i} \prod_{j=1}^{\mathcal{N}} dx'_{j,i} U(\mathcal{X}_f, \mathbf{x}_f, t; \mathcal{X}_i, \mathbf{x}_i, t_0) \\ &\quad \times \langle \mathcal{X}_i \mathbf{x}_i | W(0) | \mathcal{X}'_i \mathbf{x}'_i \rangle U^*(\mathcal{X}'_f, \mathbf{x}'_f, t; \mathcal{X}'_i, \mathbf{x}'_i, t_0) \end{aligned} \quad (2.46)$$

with

$$U(\mathcal{X}_f, \mathbf{x}_f, t; \mathcal{X}_i, \mathbf{x}_i, 0) = \langle \mathcal{X}_f \mathbf{x}_f | \mathcal{T} \exp \left[ -i \int_0^t ds H(s) \right] | \mathcal{X}_i \mathbf{x}_i \rangle \quad (2.47)$$

being the propagator for the system-plus-bath from the initial state  $|\mathcal{X}_i \mathbf{x}_i\rangle$  at time  $t_0$  to the final state  $|\mathcal{X}_f \mathbf{x}_f\rangle$  at time  $t$ . The similar restriction for the paths  $\mathcal{X}'$ ,  $\mathbf{x}'$  in (2.46) is understood implicitly. The integration over all the position coordinates is performed from  $-\infty$  to  $+\infty$ . Moreover, we have used the completeness property of the composed Hilbert space (of the system-plus-bath)  $\mathbb{I} = \int d\mathcal{X}_i \prod_{j=1}^{\mathcal{N}} \int dx_{j,i} |\mathcal{X}_i \mathbf{x}_i\rangle \langle \mathcal{X}_i \mathbf{x}_i|$  with  $\mathbb{I}$  being the identity operator. According to Feynman and Vernon [81], the propagator can be represented as a real-time functional integral over all paths, i.e.,

$$U(\mathcal{X}_f, \mathbf{x}_f, t; \mathcal{X}_i, \mathbf{x}_i, t_0) = \int_{\mathcal{X}(t_0)=\mathcal{X}_i}^{\mathcal{X}(t)=\mathcal{X}_f} \mathcal{D}\mathcal{X} \prod_{j=1}^{\mathcal{N}} \int_{x_j(t_0)=x_{j,i}}^{x_j(t)=x_{j,f}} \mathcal{D}x_j \exp \left\{ iS_S[\mathcal{X}] + \sum_{j=1}^{\mathcal{N}} S_B[\mathcal{X}, x_j] \right\} \quad (2.48)$$

with

$$\begin{aligned} S_S[\mathcal{X}] &= \int_{t_0}^t ds \left\{ \frac{m}{2} \dot{\mathcal{X}}^2(s) - \frac{m}{2} \omega_1^2 \mathcal{X}^2(s) - \frac{\alpha}{4} \mathcal{X}^4(s) - f \mathcal{X}(s) \cos \omega_{\text{ex}} s \right\}, \\ S_B[\mathcal{X}, x_j] &= \int_{t_0}^t ds \left\{ \frac{m_j}{2} \dot{x}_j^2(s) - \frac{m_j}{2} \omega_j^2 [x_j(s) - \frac{c_j}{m_j \omega_j^2} \mathcal{X}(s)]^2 \right\} \end{aligned} \quad (2.49)$$

being the classical action of each path  $\mathcal{X}(s)$  and  $[\mathcal{X}(s), x_j(s)]$  respectively. Since the details of the single bath oscillators are not of interest at every instant of time, averaging over the bath degrees of freedom is appropriate. We introduce the reduced density operator  $\varrho(t)$  by performing the trace over the bath degrees of freedom in the full density operator  $W(t)$ , i.e.,

$$\varrho(t) \equiv \text{tr}_B W(t). \quad (2.50)$$

Assuming furthermore a factorizing initial preparation (2.38) of system and bath, the path-integral (2.48) over the bath coordinates  $x_j$  can be performed since only Gaussian integrals occur. The reduced density operator in coordinate representation then reads

$$\begin{aligned} \varrho(\mathcal{X}_f, \mathcal{X}'_f, t) &= \prod_{j=1}^{\mathcal{N}} \int dx_{j,f} \langle \mathcal{X}_f \mathbf{x}_f | W(t) | \mathcal{X}'_f \mathbf{x}'_f \rangle \\ &= \int d\mathcal{X}_i \int d\mathcal{X}'_i \mathcal{G}(\mathcal{X}_f, \mathcal{X}'_f, t; \mathcal{X}_i, \mathcal{X}'_i, 0) \rho_S(\mathcal{X}_i, \mathcal{X}'_i, 0). \end{aligned} \quad (2.51)$$

Here,

$$\begin{aligned} \mathcal{G}(\mathcal{X}_f, \mathcal{X}'_f, t; \mathcal{X}_i, \mathcal{X}'_i, 0) &= \int_{\mathcal{X}(0)=\mathcal{X}_i}^{\mathcal{X}(t)=\mathcal{X}_f} \mathcal{D}\mathcal{X} \int_{\mathcal{X}'(0)=\mathcal{X}'_i}^{\mathcal{X}'(t)=\mathcal{X}'_f} \mathcal{D}\mathcal{X}' \exp \{i (S_S[\mathcal{X}] - S_S[\mathcal{X}'])\} \\ &\times \exp \{-\phi_{\text{FV}}[\mathcal{X}, \mathcal{X}']\} \end{aligned} \quad (2.52)$$

denotes the propagating function for the reduced density operator. The last term in the previous equation is the Feynman-Vernon influence functional which covers the entire influence of the bath. It contains the influence phase [81]

$$\begin{aligned} \phi_{\text{FV}}[\mathcal{X}, \mathcal{X}'] &= \int_0^t dt' \int_0^{t'} dt'' [\mathcal{X}(t') - \mathcal{X}'(t')] K(t' - t'') [\mathcal{X}(t'') - \mathcal{X}'(t'')] \\ &+ \frac{i}{2} \int_0^t dt' \int_0^{t'} dt'' [\mathcal{X}(t') - \mathcal{X}'(t')] \gamma(t' - t'') [\dot{\mathcal{X}}(t'') + \dot{\mathcal{X}}'(t'')] \\ &+ \frac{i}{2} \int_0^t dt' [\mathcal{X}(t') - \mathcal{X}'(t')] \gamma(t') [\mathcal{X}(0) + \mathcal{X}'(0)] . \end{aligned} \quad (2.53)$$

The last term, just like the one neglected in Eq. (2.33), is a transient, and will be omitted in the following.

Since we are considering a non-quadratic system Hamiltonian, the functional integral in Eq. (2.52) can not be performed analytically. In principle, an exact solution would be possible by means of numerical techniques such as Monte Carlo integration or QUAPI. However, in the weak coupling limit in the focus of this work, a perturbative approach is more appropriate. In order to be definite, from now on, we consider the spectral densities in Eq. (2.44), characterized by the powerlaw exponent  $s$ , the cut-off frequency  $\omega_c$  and the damping strength  $\gamma_s$  at the resonant frequency. In the weak coupling limit, the damping strength  $\gamma_s$  is the smallest frequency scale, meaning

$$\gamma_s \ll T, \omega_1 \omega_{\text{ex}}. \quad (2.54)$$

We can thus expand the propagator for the reduced density matrix in Eq. (2.52) in terms of  $\gamma_s$ . The zero-th order expansion  $\mathcal{G}_0(\mathcal{X}_f \mathcal{X}'_f, t; \mathcal{X}_0 \mathcal{X}'_0, 0)$  is given by the first line of Eq. (2.52). It can be expressed in terms of the propagator for the Schrödinger equation  $U_0(\mathcal{X}_f, t; \mathcal{X}_0, 0)$  as

$$\mathcal{G}_0(\mathcal{X}_f \mathcal{X}'_f, t; \mathcal{X}_0 \mathcal{X}'_0, 0) = U_0(\mathcal{X}_f, t; \mathcal{X}_0, 0) U_0^*(\mathcal{X}'_f, t; \mathcal{X}'_0, 0). \quad (2.55)$$

The first order expansion  $\mathcal{G}_1(\mathcal{X}_f \mathcal{X}'_f, t; \mathcal{X}_0 \mathcal{X}'_0, 0)$  is obtained by substituting

$$\exp(-\phi_{\text{FV}}[\mathcal{X}, \mathcal{X}']) \approx 1 - \phi_{\text{FV}}[\mathcal{X}, \mathcal{X}'] \quad (2.56)$$

into Eq. (2.52), yielding

$$\begin{aligned}
\varrho(\mathcal{X}_f, \mathcal{X}'_f, t) = & \int d\mathcal{X}_0 d\mathcal{X}'_0 \mathcal{G}_0(\mathcal{X}_f, \mathcal{X}'_f, t; \mathcal{X}_0, \mathcal{X}'_0, t_0) \varrho(\mathcal{X}_0, \mathcal{X}'_0, t_0) \\
& - \int_0^t dt' \int_0^{t'} dt'' \int d\mathcal{X}_1 d\mathcal{X}'_1 d\mathcal{X}_2 d\mathcal{X}'_2 \mathcal{G}_0(\mathcal{X}_f, \mathcal{X}'_f, t; \mathcal{X}_1, \mathcal{X}'_1, t') (\mathcal{X}_1 - \mathcal{X}'_1) \\
& \quad \times \mathcal{G}_0(\mathcal{X}_1, \mathcal{X}'_1, t'; \mathcal{X}_2, \mathcal{X}'_2, t'') K(t' - t'') (\mathcal{X}_2 - \mathcal{X}'_2) \varrho(\mathcal{X}_2, \mathcal{X}'_2, t'') \\
& - \frac{i}{2} \int_0^t dt' \int_0^{t'} dt'' \int d\mathcal{X}_1 d\mathcal{X}'_1 d\mathcal{X}_2 d\mathcal{X}'_2 \mathcal{G}_0(\mathcal{X}_f, \mathcal{X}'_f, t; \mathcal{X}_1, \mathcal{X}'_1, t') (\mathcal{X}_1 - \mathcal{X}'_1) \\
& \quad \times \mathcal{G}_0(\mathcal{X}_1, \mathcal{X}'_1, t'; \mathcal{X}_2, \mathcal{X}'_2, t'') \gamma(t' - t'') (\dot{\mathcal{X}}_2 + \dot{\mathcal{X}}'_2) \varrho(\mathcal{X}_2, \mathcal{X}'_2, t'') \quad (2.57)
\end{aligned}$$

It is convenient to express  $\varrho(t'')$  in terms of  $\varrho(t)$  by using the zero-th order propagator in Eq. (2.55) such that

$$\varrho(\mathcal{X}_2, \mathcal{X}'_2, t'') = \int d\mathcal{X} d\mathcal{X}' U_0(\mathcal{X}_2, t''; \mathcal{X}, t) U_0^*(\mathcal{X}'_2, t''; \mathcal{X}', t) \varrho(\mathcal{X}, \mathcal{X}', t). \quad (2.58)$$

By inserting this expression into Eq. (2.57), differentiating with respect to  $t$ , and defining  $\tau = t - t''$ , we get the master equation

$$\begin{aligned}
\dot{\varrho}(\mathcal{X}_f, \mathcal{X}'_f, t) = & -i(H_S(\mathcal{X}_f) - H_S(\mathcal{X}'_f)) \varrho(\mathcal{X}_f, \mathcal{X}'_f, t) \\
& - \int_0^t d\tau K(\tau) \int d\mathcal{X}_2 d\mathcal{X}'_2 d\mathcal{X} d\mathcal{X}' (\mathcal{X}_f - \mathcal{X}'_f) U_0(\mathcal{X}_f, t; \mathcal{X}_2, t - \tau) U_0^*(\mathcal{X}'_f, t; \mathcal{X}'_2, t - \tau) \\
& \quad \times (\mathcal{X}_2 - \mathcal{X}'_2) U_0(\mathcal{X}_2, t - \tau; \mathcal{X}, t) U_0^*(\mathcal{X}'_2, t - \tau; \mathcal{X}', t) \varrho(\mathcal{X}, \mathcal{X}', t) \\
& - \frac{i}{2} \int_0^t d\tau \gamma(\tau) \int d\mathcal{X}_2 d\mathcal{X}'_2 d\mathcal{X} d\mathcal{X}' (\mathcal{X}_f - \mathcal{X}'_f) U_0(\mathcal{X}_f, t; \mathcal{X}_2, t - \tau) U_0^*(\mathcal{X}'_f, t; \mathcal{X}'_2, t - \tau) \\
& \quad \times (\dot{\mathcal{X}}_2 + \dot{\mathcal{X}}'_2) U_0(\mathcal{X}_2, t - \tau; \mathcal{X}, t) U_0^*(\mathcal{X}'_2, t - \tau; \mathcal{X}', t) \varrho(\mathcal{X}, \mathcal{X}', t). \quad (2.59)
\end{aligned}$$

This master equation is Markovian (memoryless) since the derivative of the reduced density matrix  $\dot{\varrho}(t)$  depends only on the density matrix  $\varrho(t)$  at equal time. The MME can be written in the more compact operatorial form as

$$\frac{d}{dt} \varrho = -i[H_S(t), \varrho] + \mathcal{L} \varrho. \quad (2.60)$$

The influence of the bath enters in the superoperator

$$\mathcal{L} \varrho = -[\mathcal{X}, [P(t), \varrho]_+] - [\mathcal{X}, [Q(t), \varrho]]. \quad (2.61)$$

Here we have defined the correlators

$$P(t) = \frac{i}{2} \int_0^\infty d\tau \gamma(\tau) U_0^\dagger(t - \tau, t) \mathcal{P} U_0(t - \tau, t) \quad (2.62)$$

and

$$Q(t) = \int_0^\infty d\tau K(\tau) U_0^\dagger(t - \tau, t) \mathcal{X} U_0(t - \tau, t). \quad (2.63)$$



Moreover, we have assumed that the integration kernel  $K(t)$  and  $\gamma(t)$  are practically zero after a finite time  $\tau_B$  and extended the upper integration limit in Eq. (2.59) to infinity, thereby implicitly considering the time distance  $t$  from the preparation to be much larger than  $\tau_B$ .

### 2.4.3 Floquet master equation

In this subsection we want to combine the MME approach with the Floquet formalism described in Subsection 2.3.1. This treatment is appropriate for weak coupling to the bath but arbitrary driving strengths, since the Floquet formalism is exact. We start by selecting a complete set of Floquet solutions  $\{|\phi_\alpha(t)\rangle\}$ , such that

$$\sum_{\alpha} |\phi_\alpha(t)\rangle \langle \phi_\alpha(t)| = \mathbb{I}_{\mathcal{R}}, \quad (2.64)$$

with  $\mathbb{I}_{\mathcal{R}}$  being the identity operator in the system Hilbert space  $\mathcal{R}$ . The choice is not unique, since, according to the discussion in Subsection 2.3.1, there is an infinite number of eigenvectors of the Floquet Hamiltonian which correspond to the same solution of the Schrödinger equation. We then project the density matrix onto the selected set of Floquet states, such that the matrix elements read

$$\varrho_{\alpha\beta}(t) = \langle \phi_\alpha(t) | \varrho(t) | \phi_\beta(t) \rangle. \quad (2.65)$$

Performing the derivative one obtains

$$\begin{aligned} \dot{\varrho}_{\alpha\beta}(t) &= -i \langle \phi_\alpha(t) | \left[ i \frac{\overleftarrow{d}}{dt} \varrho + [H(t), \varrho] + i\mathcal{L}\varrho + \varrho i \frac{d}{dt} \right] | \phi_\beta(t) \rangle \\ &= -i(\varepsilon_\alpha - \varepsilon_\beta) \varrho_{\alpha\beta}(t) + \langle \phi_\alpha(t) | \mathcal{L} \varrho | \phi_\beta(t) \rangle. \end{aligned} \quad (2.66)$$

For the dissipative term, we need to compute

$$X_{\alpha\beta}(t) = \langle \phi_\alpha(t) | \mathcal{X} | \phi_\beta(t) \rangle = \sum_n e^{-in\omega_{\text{ex}}t} X_{\alpha\beta,n}, \quad n \in \mathbb{Z}. \quad (2.67)$$

The Fourier transform of the mean value of the position operator  $X_{\alpha\beta,n}$  can be expressed in terms of the Fourier transform of the Floquet states, given in Eq. (2.11), as

$$X_{\alpha\beta,n} = \sum_j \langle \hat{\phi}_{\alpha j} | \mathcal{X} | \hat{\phi}_{\beta j+n} \rangle. \quad (2.68)$$

We need, moreover,

$$\begin{aligned} Q_{\alpha\beta}(t) &= \int_0^\infty d\tau K(\tau) \langle \phi_\alpha(t) | U_0^\dagger(t-\tau, t) \mathcal{X} U_0(t-\tau, t) | \phi_\beta(t) \rangle \\ &= \int_0^\infty d\tau K(\tau) e^{-i(\varepsilon_\alpha - \varepsilon_\beta)\tau} \langle \phi_\alpha(t-\tau) | \mathcal{X} | \phi_\beta(t-\tau) \rangle \\ &= \sum_n e^{-in\omega_{\text{ex}}t} \left[ \int_0^\infty d\tau K(\tau) e^{-i(\varepsilon_\alpha - \varepsilon_\beta - n\omega_{\text{ex}})\tau} \right] X_{\alpha\beta,n}. \end{aligned} \quad (2.69)$$

In an analogous way, we have

$$\begin{aligned}
P_{\alpha\beta}(t) &= \frac{i}{2} \int_0^\infty d\tau \gamma(\tau) e^{-i(\varepsilon_\alpha - \varepsilon_\beta)\tau} \langle \phi_\alpha(t - \tau) | \mathcal{P} | \phi_\beta(t - \tau) \rangle \\
&= -\frac{m}{2} \int_0^\infty d\tau \gamma(\tau) e^{-i(\varepsilon_\alpha - \varepsilon_\beta)\tau} \\
&\quad \times \left( \langle \phi_\alpha(t - \tau) | [\pm i \frac{\overleftrightarrow{d}}{dt} + H(t), \mathcal{X}] | \phi_\beta(t - \tau) \rangle - i \frac{d}{dt} \langle \phi_\alpha(t - \tau) | \mathcal{X} | \phi_\beta(t - \tau) \rangle \right) \\
&= -\frac{m}{2} \left( \varepsilon_\alpha - \varepsilon_\beta - i \frac{d}{dt} \right) \left[ \int_0^\infty d\tau \gamma(\tau) e^{-i(\varepsilon_\alpha - \varepsilon_\beta)\tau} X_{\alpha\beta}(t - \tau) \right]. \tag{2.70}
\end{aligned}$$

Here, we have defined the time derivative  $\pm \frac{\overleftrightarrow{d}}{dt}$  where the positive (negative) sign belongs to the left (right) direction. In the second line, we have used the canonical relation  $\mathcal{P}/m = -i[\mathcal{X}, H(t)]$ . We can now compute the matrix elements of the operators involved in the dissipative part in Eq. (2.66) and find for the terms in Eq. (2.61)

$$(P + Q)_{\alpha\beta} = \sum_n e^{-in\omega_{\text{ext}}} N_{\alpha\beta, -n} X_{\alpha\beta, n}, \tag{2.71}$$

and

$$(P - Q)_{\alpha\beta} = -\sum_n e^{-in\omega_{\text{ext}}} N_{\beta\alpha, n} X_{\alpha\beta, n}. \tag{2.72}$$

Here,  $N_{\alpha\beta, n}$  are defined as

$$N_{\alpha\beta, n} = N(\varepsilon_\alpha - \varepsilon_\beta + n\omega_{\text{ex}}), \quad N(\varepsilon) = J(|\varepsilon|) [n_{th}(|\varepsilon|) + \Theta(-\varepsilon)], \tag{2.73}$$

in terms of the bath density of states  $J(|\varepsilon|)$ , the bosonic thermal occupation number

$$n_{th}(\varepsilon) = \frac{1}{2} \left[ \coth \left( \frac{\varepsilon}{2k_B T} \right) - 1 \right], \tag{2.74}$$

and the Heaviside function  $\Theta(x)$ .

Note that  $N(\varepsilon)$  in Eq. (2.73) diverges for  $s < 1$  at low energies. This indicates that a perturbative approach is not appropriate for a sub-Ohmic bath. For this reason we will restrict to (super-)Ohmic baths. During the calculation, the  $\tau$ -integration in the double integrals in Eqs. (2.70) and (2.69) has been evaluated by using the representation  $\int_0^\infty d\tau \exp(i\omega\tau) = \pi\delta(\omega) + i\mathcal{P}_p(1/\omega)$ , where  $\mathcal{P}_p$  denotes the principal part. The contributions of the principal part result in quasienergy shifts of the order of  $\gamma_s$  which are the so-called Lamb shifts. As usual, these have also been neglected here.

The ingredients can now be put together to obtain the Floquet Markovian master equation as

$$\begin{aligned}
\dot{\varrho}_{\alpha\beta}(t) &= -i(\varepsilon_\alpha - \varepsilon_\beta) \varrho_{\alpha\beta}(t) \\
&+ \sum_{\alpha'\beta'} \sum_{n, n'} e^{-i(n+n')\omega_{\text{ext}}} [(N_{\alpha\alpha', -n} + N_{\beta\beta', n'}) X_{\alpha\alpha', n} \rho_{\alpha\beta'} X_{\beta'\beta, n'} \\
&- N_{\beta'\alpha', -n'} X_{\alpha\beta', n} X_{\beta'\alpha', n'} \rho_{\alpha'\beta} - N_{\alpha'\beta', n'} \rho_{\alpha\beta'} X_{\beta'\alpha', n'} X_{\alpha'\beta, n}] . \tag{2.75}
\end{aligned}$$

Next, we perform a *moderate rotating-wave approximation* consisting in averaging the time-dependent terms in the bath part over the driving period  $T_{\omega_{\text{ex}}} = 2\pi/\omega_{\text{ex}}$ , yielding

$$\dot{\varrho}_{\alpha\beta}(t) = \sum_{\alpha'\beta'} \mathcal{S}_{\alpha\beta,\alpha'\beta'} \varrho_{\alpha'\beta'}(t) = \sum_{\alpha'\beta'} [-i(\varepsilon_\alpha - \varepsilon_\beta)\delta_{\alpha\alpha'}\delta_{\beta\beta'} + \mathcal{L}_{\alpha\beta,\alpha'\beta'}] \varrho_{\alpha'\beta'}(t) \quad (2.76)$$

with the dissipative transition rates

$$\begin{aligned} \mathcal{L}_{\alpha\beta,\alpha'\beta'} = & \sum_n (N_{\alpha\alpha',-n} + N_{\beta\beta',-n}) X_{\alpha\alpha',n} X_{\beta'\beta,-n} \\ & - \delta_{\alpha\alpha'} \sum_{\alpha'';n} N_{\alpha''\beta',-n} X_{\beta'\alpha'',-n} X_{\alpha''\beta,n} \\ & - \delta_{\beta\beta'} \sum_{\beta'';n} N_{\beta''\alpha',-n} X_{\alpha\beta'',-n} X_{\beta''\alpha',n}. \end{aligned} \quad (2.77)$$

The moderate rotating-wave master equation has been originally introduced in Ref. [96], and has been since then used in a number of papers. The reason of its popularity is that it yields a time-independent stationary solution  $\varrho_{\alpha\beta}$ , which can be obtained by solving the simple linear system of equations

$$0 = -i(\varepsilon_\alpha - \varepsilon_\beta)\varrho_{\alpha\beta} + \sum_{\alpha'\beta'} \mathcal{L}_{\alpha\beta,\alpha'\beta'} \varrho_{\alpha'\beta'}. \quad (2.78)$$

However, to the knowledge of the author of this thesis, a discussion on the limit of validity of this approximation is still missing in the literature. It is thus worth to state a few remarks on it. Since the right-hand side of Eq. (2.78) is of order  $\gamma$ ,  $\gamma$  acts as a cut-off frequency for the coherences in the stationary state:  $|\varepsilon_\alpha - \varepsilon_\beta| \gg \gamma$  implies  $\varrho_{\alpha\beta} = \varrho_{\beta\alpha} = 0$ . Correspondingly  $\varrho_{\alpha\beta} = \varrho_{\beta\alpha}^* \neq 0$  implies  $|\varepsilon_\alpha - \varepsilon_\beta| \approx \gamma$  or less. However, as already observed, the choice of a Floquet basis is not unique. Let us assume that in a certain Floquet basis there are two Floquet solutions  $|\phi_\alpha(t)\rangle$  and  $|\phi_\beta(t)\rangle$  whose quasienergy difference  $|\varepsilon_\alpha - \varepsilon_\beta|$  is of order  $\gamma$ , the corresponding matrix elements  $\varrho_{\alpha\beta}$  and  $\varrho_{\beta\alpha}$  are thus finite at equilibrium. By replacing the element  $|\phi_\alpha(t)\rangle$  in the Floquet basis with the vector  $|\phi_\alpha^{(n)}(t)\rangle = e^{in\omega_{\text{ex}}t}|\phi_\alpha(t)\rangle$  corresponding to the same solution of the Schrödinger equation, the corresponding matrix elements  $\varrho_{\beta\alpha}$  and  $\varrho_{\alpha\beta}$  acquire a time dependence according to

$$\begin{aligned} \varrho_{\beta\alpha} &= \langle \phi_\beta(t) | \varrho(t) | \phi_\alpha(t) \rangle \rightarrow \langle \phi_\beta(t) | \varrho(t) | \phi_\alpha^{(n)}(t) \rangle = e^{in\omega_{\text{ex}}t} \varrho_{\beta\alpha}, \\ \varrho_{\alpha\beta} &= \langle \phi_\alpha(t) | \varrho(t) | \phi_\beta(t) \rangle \rightarrow \langle \phi_\alpha^{(n)}(t) | \varrho(t) | \phi_\beta(t) \rangle = e^{-in\omega_{\text{ex}}t} \varrho_{\alpha\beta}. \end{aligned} \quad (2.79)$$

On the other hand, if we had performed the moderate rotating-wave approximation directly in this basis we would have obtained a time-independent solution. In particular, we would have obtained  $\varrho_{\alpha\beta} = 0$ , since

$$|\varepsilon_\alpha - \varepsilon_\beta| \rightarrow |\varepsilon_\alpha - \varepsilon_\beta - n\omega_{\text{ex}}| \gg \gamma \quad (2.80)$$

within the limit of validity of the Markovian approximation  $\gamma \ll \omega_{\text{ex}}$ . The reason of this discrepancy is that by replacing  $|\phi_\alpha(t)\rangle$  with  $|\phi_\alpha^{(n)}(t)\rangle = e^{in\omega_{\text{ex}}t}|\phi_\alpha(t)\rangle$  in

the Floquet basis the indices  $\{\alpha\beta, n'\}$  and  $\{\beta\alpha, n'\}$  of the matrix elements  $X_{\alpha\beta, n'}$  ( $N_{\alpha\beta, n'}$ ) and  $X_{\beta\alpha, n'}$  ( $N_{\beta\alpha, n'}$ ), which appear in the Floquet master equation (2.75), change according to

$$\{\alpha\beta, n'\} \rightarrow \{\alpha\beta, n' + n\} \quad \text{and} \quad \{\beta\alpha, n'\} \rightarrow \{\beta\alpha, n' - n\}, \quad (2.81)$$

respectively. As long as we solve the full Floquet master equation in Eq. (2.75), we get solutions that transform according to Eq. (2.79) under a change of the Floquet basis. On the other hand, while performing the moderate rotating-wave approximation, the choice of a basis determines which contributions are included and which are neglected in Eq. (2.76). Hence one has to be careful in choosing the Floquet basis so that those terms are kept, that would yield a finite off-diagonal term in the equilibrium density matrix. This can be achieved by selecting all the Floquet states within one Brillouin zone. Moreover, one has to be careful with the states whose energies lie near the borders of the Brillouin zone. If two states exist, such that  $|\varepsilon_\alpha - \varepsilon_\beta| > \omega_{\text{ex}} - \gamma$  the borders of the Brillouin zone have to be moved, so that one of the states is replaced by its equivalent from the nearby Brillouin zone and the quasi-energy difference becomes  $|\varepsilon_\alpha - \varepsilon_\beta| < \gamma$  yielding a finite off-diagonal element  $\varrho_{\alpha\beta}$  of the equilibrium density matrix. If, consistent with the Markovian approximation,  $\gamma \ll \omega_{\text{ex}}$ , it is possible to define a Brillouin zone so that no state lies in a narrow stripe of width  $\gamma$  around the border and all the relevant contributions are taken into account.

A simpler but more heuristic argument leading to the rotating-wave approximation corresponds to note that the characteristic frequency of the free evolution of the density matrix (corresponding to  $\gamma = 0$ )  $\varrho_{\alpha\beta}(t) = e^{-i(\varepsilon_\alpha - \varepsilon_\beta)t} \varrho_{\alpha\beta}(0)$  is  $\varepsilon_\alpha - \varepsilon_\beta$  and to assume that in the weak coupling limit only those terms of the superoperator  $\mathcal{L}$  in Eq. (2.75) are relevant for the dissipative dynamics, which oscillates with frequency in an interval of width  $\gamma$  around  $\varepsilon_\alpha - \varepsilon_\beta$ . All the other terms can be averaged out. If we choose a Floquet basis, corresponding to a Brillouin zone such that no state lies in a narrow stripe of width  $\gamma$  around the border, all the relevant contributions to the master equation (2.75) correspond to  $n = -n'$  and are taken into account in the moderate rotating-wave approximation.

#### 2.4.4 RWA master equation

The Floquet master equation derived in the previous section treats the system Hamiltonian exactly and is thus valid for an arbitrary nonlinearity and driving strength. Its stationary solution can be straightforwardly computed numerically by diagonalizing the Floquet Hamiltonian in Eq. (2.9), computing the Fourier components of the position operator in Eq. (2.68) and solving the linear system in Eq. (2.78). We will follow this approach in section 2.6. In this section, we derive a different master equation by applying the RWA, introduced in Section 2.3.2, to the system dynamics. This approach, valid for  $\alpha \ll \omega_1$ ,  $f \ll \alpha$  and  $|\omega_{\text{ex}} - \omega_1| \ll \omega_1$ , will allow an analytical perturbative treatment of the full dissipative dynamics, which will be pursued in Section 2.5.

We start by projecting the MME Eq. (2.66) onto the approximate Floquet states  $\{|\phi_\alpha(t)\rangle \equiv \exp[-i\omega_{\text{ex}}a^\dagger at]|\varphi_\alpha\rangle\}$  rather than onto the exact Floquet solutions. As a consequence to this approximation, all the Fourier components of  $X_{\alpha\beta,n}$  vanish except for  $X_{\alpha\beta,-1}$  and  $X_{\alpha\beta,1}$ , yielding

$$\begin{aligned} X_{\alpha\beta}(t) &= \langle\varphi_\alpha|e^{i\omega_{\text{ex}}a^\dagger at}\mathcal{X}e^{-i\omega_{\text{ex}}a^\dagger at}|\varphi_\beta\rangle = (e^{-i\omega_{\text{ex}}t}X_{\alpha\beta,+1} + e^{i\omega_{\text{ex}}t}X_{\alpha\beta,-1}) \\ &= \frac{x_0}{\sqrt{2}}(e^{-i\omega_{\text{ex}}t}\langle\varphi_\alpha|a|\varphi_\beta\rangle + e^{i\omega_{\text{ex}}t}\langle\varphi_\alpha|a^\dagger|\varphi_\beta\rangle). \end{aligned} \quad (2.82)$$

Hence the sums in Eq. (2.75) include only the terms with  $n, n' = \pm 1$ . Being consistent with the RWA, we can assume that  $|\nu|, |\mu|, |\omega_{\text{ex}} - \omega_1| \ll \omega_1$ , which yields to  $|\varepsilon_\alpha - \varepsilon_\beta| \ll \omega_{\text{ex}}$ . According to the discussion in the previous subsection, we can then perform the moderate rotating-wave approximation by averaging out the time dependent contribution to  $\mathcal{L}$  corresponding to  $n = n' = \pm 1$ . The dissipative transition rates, entering in the master equation (2.76) then read

$$\begin{aligned} \mathcal{L}_{\alpha\beta,\alpha'\beta'} &= \sum_{n=\pm 1} (N_{\alpha\alpha',-n} + N_{\beta\beta',-n})X_{\alpha\alpha',n}X_{\beta'\beta,-n} \\ &\quad - \delta_{\alpha\alpha'} \sum_{\alpha'';n=\pm 1} N_{\alpha''\beta',-n}X_{\beta'\alpha'',-n}X_{\alpha''\beta,n} \\ &\quad - \delta_{\beta\beta'} \sum_{\beta'';n=\pm 1} N_{\beta''\alpha',-n}X_{\alpha\beta'',-n}X_{\beta''\alpha',n}. \end{aligned} \quad (2.83)$$

The sums in Eq. (2.83) only include the  $n = \pm 1$  terms indicating that only one-step transitions are possible where  $n = -1$  refers to emission and  $n = +1$  to absorption. Since  $|\varepsilon_\alpha - \varepsilon_\beta| \ll \omega_{\text{ex}}$ ,  $N_{\alpha\beta,+1}$ , given in Eq. (2.73), is the product of the bath density of states and the bosonic occupation number at temperature  $T$ . This corresponds to the thermally activated absorption of a photon from the bath. On the other hand,  $N_{\alpha\beta,-1}$  contains the temperature-independent term  $.. + J(\omega_{\text{ex}})$  describing spontaneous emission.

We can conclude that the RWA simplify considerably the Floquet master equation, leading to compact expressions for the transition rates, which will allow a fully analytical treatment to take into account the influence of the thermal bath on the system.

Interestingly enough, within the framework of the RWA, it is possible to derive an extension of the master equation presented in this section to the bichromatically driven anharmonic oscillator. The derivation is presented in Appendix C.

### 2.4.5 Observable for the nonlinear response

We are interested in the nonlinear response characterized by the mean value of the position operator in the stationary state according to

$$\langle\mathcal{X}\rangle_t = \text{tr}(\varrho(t)\mathcal{X}) = \sum_{\alpha\beta} \varrho_{\alpha\beta}(t)X_{\beta\alpha}(t). \quad (2.84)$$

Using Eq. (2.68) yields  $\langle \mathcal{X} \rangle = A \cos(\omega_{\text{ex}} t + \varphi)$ , with the oscillation amplitude

$$A = 2 \left| \sum_{\alpha\beta} \varrho_{\alpha\beta} X_{\beta\alpha,+1} \right|, \quad (2.85)$$

and the phase shift

$$\begin{aligned} \varphi = & -\pi \Theta \left( -\text{Re} \left[ \sum_{\alpha\beta} \varrho_{\alpha\beta} X_{\beta\alpha,+1} \right] \right) \\ & + \text{sgn} \left( -\text{Re} \left[ \sum_{\alpha\beta} \varrho_{\alpha\beta} X_{\beta\alpha,+1} \right] \right) \arctan \left[ \frac{\text{Im} \left[ \sum_{\alpha\beta} \varrho_{\alpha\beta} X_{\beta\alpha,+1} \right]}{\text{Re} \left[ \sum_{\alpha\beta} \varrho_{\alpha\beta} X_{\beta\alpha,+1} \right]} \right], \end{aligned} \quad (2.86)$$

with  $\Theta$  being the Heaviside function.

## 2.5 Analytical results in the perturbative regime

In this section we solve perturbatively the RWA master equation around resonant frequency corresponding to the multiple multiphoton transitions. We then compute the lineshape of the transition, resulting in a resonance or an antiresonance depending on the bath parameter.

Within the limit of validity of the RWA, i.e.,  $|\nu|, |f|, |\omega_{\text{ex}} - \omega_1| \ll \omega_1$ , we have  $|\varepsilon_\alpha - \varepsilon_\beta| \ll \omega_{\text{ex}}$ . In the regime of low temperature  $k_B T \ll \omega_{\text{ex}}$ , it follows from Eq. (2.73) that  $N_{\alpha\beta,-1} \simeq J(\omega_{\text{ex}})$  and  $N_{\alpha\beta,1} \simeq 0$  entering in the transition rates in Eq. (2.83). This approximation corresponds to consider spontaneous emission only and yields the dissipative transition rates

$$\mathcal{L}_{\alpha\beta,\alpha'\beta'} = \frac{\gamma_s}{2} \left( \frac{\omega_{\text{ex}}}{\omega_1} \right)^s \left( 2A_{\alpha\alpha'} A_{\beta\beta'} - \delta_{\alpha\alpha'} \sum_{\alpha''} A_{\alpha''\beta'} A_{\alpha''\beta} - \delta_{\beta\beta'} \sum_{\beta''} A_{\beta''\alpha} A_{\beta''\alpha'} \right). \quad (2.87)$$

Here, we have defined  $A_{\alpha\beta} \equiv \langle \varphi_\alpha | a | \varphi_\beta \rangle$ . Note that it is consistent with the previous approximation to set  $\omega_{\text{ex}}/\omega_1 \approx 1$ . Hence, all the following results are valid for Ohmic as well as super-Ohmic baths.

In the following we will use this simplified transition rates to solve the master equation near the multiple multiphoton resonances. The transition between the groundstate and the  $N$ -photon state is the narrowest. Hence, it will be affected first when a finite coupling to the bath is considered. In particular, it is interesting to consider the case when the damping constant  $\gamma_s$  is larger than the minimal splitting  $\Omega_{N0}$  between the two quasienergy states but smaller than all the minimal splittings of the other, i.e.,  $\Omega_{N0} < \gamma_s \ll \Omega_{Nn}$  for  $n \geq 1$ . In this case, we can assume a partial secular approximation: We set all the off-diagonal elements to zero except

for  $\varrho_{0N}$  and  $\varrho_{N0} = \varrho_{0N}^*$ . In this regime the stationary solutions are determined by the conditions

$$\begin{aligned} 0 &= \sum_{\beta} \mathcal{L}_{\alpha\alpha,\beta\beta} \varrho_{\beta\beta} + \mathcal{L}_{\alpha\alpha,0N} 2 \operatorname{Re}(\varrho_{0N}), \\ 0 &= -i(\varepsilon_0 - \varepsilon_N) \varrho_{0N} + \sum_{\alpha} \mathcal{L}_{0N,\alpha\alpha} \varrho_{\alpha\alpha} + \mathcal{L}_{0N,0N} \varrho_{0N} + \mathcal{L}_{0N,N0} \varrho_{0N}^*. \end{aligned} \quad (2.88)$$

For very weak damping, i.e., when  $\gamma_s$  is smaller than all minimal splittings ( $\gamma_s \ll \Omega_{Nn}$ ), the off-diagonal elements of the density matrix are negligibly small and can be set to zero. Within this approximation, the stationary solution for the density matrix is determined by the simple kinetic equation

$$0 = \sum_{\beta} \mathcal{L}_{\alpha\alpha,\beta\beta} \varrho_{\beta\beta}. \quad (2.89)$$

In this regime, a very simple physical picture arises. The bath causes transitions between different quasienergy states, but here, the transition rates are independent from the quasienergies. It is instructive to express the quasienergy solutions in terms of the harmonic oscillator (HO) solutions as  $|\varphi_{\alpha}\rangle = \sum_n c_{\alpha n} |n\rangle$  with some coefficients  $c_{\alpha n}$ . The transition rates between two quasienergy states then read

$$\mathcal{L}_{\alpha\alpha,\beta\beta} = \gamma_s |\langle \varphi_{\alpha} | a | \varphi_{\beta} \rangle|^2 = \gamma_s \sum_n (n+1) |c_{\alpha n}|^2 |c_{\beta n+1}|^2. \quad (2.90)$$

This formula illustrates simple selection rules in this low-temperature regime: When the Floquet states are decomposed in terms of the harmonic oscillator eigenstates, only those components of the two different quasienergy states contribute to the transition rate whose excitation number differ by one ( $n \leftrightarrow n+1$ ).

### 2.5.1 One-photon resonance vs. antiresonance

Before we consider the general multiphoton case, we first elaborate on the one-photon resonance. This, in particular, allows to make the connection to the standard linear response of a driven damped harmonic oscillator which is resonant at the frequency  $\omega_1 + \nu$ . We will illustrate the mechanism how this resonant behavior is turned into an antiresonant behavior when the damping is reduced (and the driving amplitude  $\mu$  is kept fixed).

The corresponding effective Hamiltonian  $\tilde{H}'_0$  follows from Eq. (2.25) and is readily diagonalized by the quasienergy states  $|\varphi_0\rangle$  and  $|\varphi_1\rangle$  which are of zero-th order in  $\varepsilon$  and which are given in Eq. (2.26). The master equation (2.88) can be straightforwardly solved in terms of the rates  $\mathcal{L}_{\alpha\beta,\alpha'\beta'}$  for which one needs the ingredients  $A_{00} = -A_{11} = \sin(\theta/2) \cos(\theta/2)$ ,  $A_{01} = \cos^2(\theta/2)$  and  $A_{10} = -\sin^2(\theta/2)$ . The

general solution follows as

$$\begin{aligned}
\varrho_{00} &= \frac{-\mathcal{L}_{00,11}[\mathcal{L}_{01,01}^2 - \mathcal{L}_{01,10}^2 + \Omega^2(\Delta)] + 2\mathcal{L}_{00,01}\mathcal{L}_{01,11}(\mathcal{L}_{01,01} - \mathcal{L}_{01,10})}{(\mathcal{L}_{00,00} - \mathcal{L}_{00,11})[\mathcal{L}_{01,01}^2 - \mathcal{L}_{01,10}^2 + \Omega^2(\Delta)] - 2\mathcal{L}_{00,01}(\mathcal{L}_{01,00} - \mathcal{L}_{01,11})(\mathcal{L}_{01,01} - \mathcal{L}_{01,10})}, \\
\text{Re}\varrho_{01} &= \frac{-(\mathcal{L}_{01,01} - \mathcal{L}_{01,10})[\mathcal{L}_{01,11} + (\mathcal{L}_{01,00} - \mathcal{L}_{01,11})\varrho_{00}]}{\mathcal{L}_{01,01}^2 - \mathcal{L}_{01,10}^2 + \Omega^2(\Delta)}, \\
\text{Im}\varrho_{01} &= \frac{\Omega(\Delta)}{\mathcal{L}_{01,01} - \mathcal{L}_{01,10}} \text{Re}\varrho_{01}, \tag{2.91}
\end{aligned}$$

where  $\Omega(\Delta) = \varepsilon_0 - \varepsilon_1$ .

In the following, we calculate the amplitude  $A$  according to Eq. (2.85) to zero-th order in  $\varepsilon$ . In Fig. 2.4, we show the nonlinear response for the parameter set (in dimensionless units)  $\mu = 10^{-5}$  and  $\nu = 10^{-3}$ . Moreover, the one-photon resonance condition reads  $\omega_{\text{ex}} = \omega_1 + \nu$ . The transition from the resonant to antiresonant behavior depends on the ratio  $\gamma/\Omega_{10} = \gamma/(2\mu)$ . For the case of stronger damping,  $\gamma/(2\mu) = 10$ , we find that the response shows a resonant behavior with a Lorentzian form similar to the response of a damped linear oscillator. In fact, the corresponding standard classical result is also shown in Fig. 2.4 (black dashed line). The only effect of the nonlinearity to lowest order perturbation theory is to shift the resonance frequency by the nonlinearity parameter  $\nu$ . The resonant behavior turns into an antiresonant one if the damping constant is decreased to smaller values. A cusp-like line profile arises in the limit of very weak damping when the damping strength is smaller than the minimal splitting, i.e.,  $\gamma/(2\mu) \ll 1$ . Then, the response follows from the master equation (2.89) as

$$A = x_0\sqrt{2} \left| \sin \frac{\theta}{2} \cos \frac{\theta}{2} \right| \left| \frac{\sin^4 \frac{\theta}{2} - \cos^4 \frac{\theta}{2}}{\sin^4 \frac{\theta}{2} + \cos^4 \frac{\theta}{2}} \right|. \tag{2.92}$$

This antiresonance lineshape is also shown in Fig. 2.4 (see dotted-dashed line). At resonance  $\Delta = 0$ , we have an equal population of the quasienergy states:  $\varrho_{00} = \varrho_{11} = 1/2$  and both add up to a vanishing oscillation amplitude  $A$  since  $A_{00} = -A_{11}$ . Note that we show also the solution from the exact master equation containing all orders in  $\varepsilon$ , for the case  $\gamma/(2\mu) = 0.5$  and  $s = 1$  (blue dashed line in Fig. 2.4), in order to verify the validity of our perturbative treatment.

### 2.5.2 Multiphoton resonance vs. antiresonance

In this subsection we want to investigate the multiple multiphoton resonances  $N > 1$ . In order to illustrate the physics, we start with the simplest case at resonance and within the secular approximation.

#### Secular approximation at resonance

The zero-th order quasienergy solutions are given in terms of the eigenstates of the harmonic oscillator in Eq. (2.26) with  $\theta = \pi/4$ . Then,  $|n\rangle$  and  $|N - n\rangle$  ( $n < N/2$ )



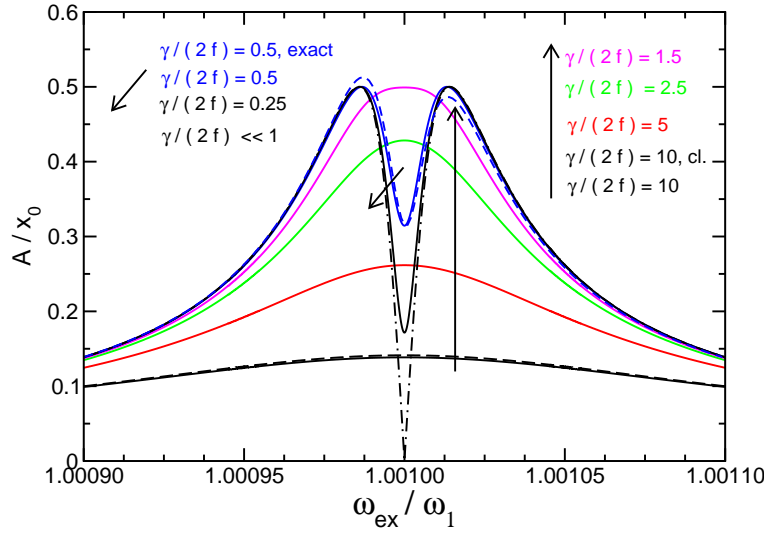


**Figure 2.4:** Nonlinear response of the nanoresonator at the one-photon resonance  $N = 1$ , where  $\omega_{\text{ex}} = \omega_1 + \nu$  for the parameters  $\mu = 10^{-5}$  and  $\nu = 10^{-3}$  (in dimensionless units). The transition from a resonant behavior for large damping ( $\gamma/(2\mu) = 10$ ) to an antiresonant behavior at small damping ( $\gamma/(2\mu) \ll 1$ ) is clearly visible. The resonant line shape is a Lorentzian and coincides with the linear response of a harmonic oscillator at frequency  $\omega_1 + \nu$  (see black dashed line for  $\gamma/(2\mu) = 10$ ). Also shown is the limit of  $\gamma/(2\mu) \ll 1$  (black dotted-dashed line) yielding a cusplike lineshape. Note that we also depict the solution from the exact master equation for the case  $\gamma/(2\mu) = 0.5$  (blue dashed line).

form a pair of quasienergy solutions. For  $N$  odd, there are  $(N + 1)/2$  pairs. For  $N$  even, there are  $N/2$  pairs whereas the state  $|\varphi_{N/2}\rangle = |N/2\rangle$  remains sole. Within the secular approximation, we can describe the dynamics in terms of the kinetic equation (2.89). Plugging Eq. (2.26) into the expression for the transition rates in Eq. (2.90), we find that most of the transition rates between two different states belonging to two different pairs are zero, except for

$$\begin{aligned}
 \mathcal{L}_{nn,n+1n+1} &= \mathcal{L}_{nn,N-n-1N-n-1} = \mathcal{L}_{N-nN-n,n+1n+1} \\
 &= \mathcal{L}_{N-nN-n,N-n-1N-n-1} = \frac{\gamma_s}{4}(n+1), \\
 \mathcal{L}_{n+1n+1,nn} &= \mathcal{L}_{n+1n+1,N-nN-n} = \mathcal{L}_{N-n-1N-n-1,nn} \\
 &= \mathcal{L}_{N-n-1N-n-1,N-nN-n} = \frac{\gamma_s}{4}(N-n), \\
 \mathcal{L}_{N/2N/2,N/2\pm 1N/2\pm 1} &= \frac{\gamma_s}{4}(N+2) \quad (\text{for } N \text{ even}), \\
 \mathcal{L}_{N/2\pm 1N/2\pm 1,N/2N/2} &= \frac{\gamma_s}{4}N \quad (\text{for } N \text{ even}).
 \end{aligned} \tag{2.93}$$

The transition rates between states belonging to the same pair are zero with the exception  $\mathcal{L}_{(N-1)/2(N-1)/2,(N+1)/2(N+1)/2} = \gamma_s(N+1)/8$ .

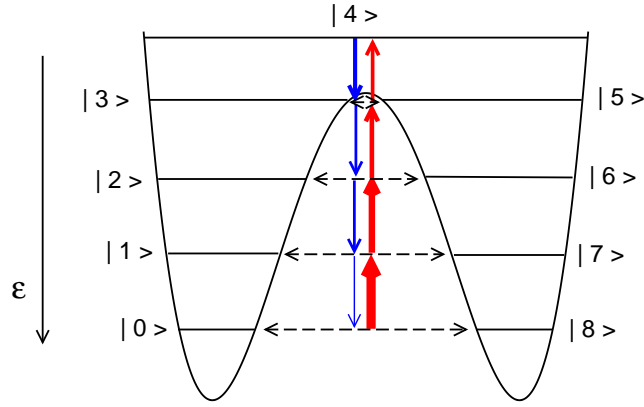


**Figure 2.5:** Schematic view of the quasipotential and localized states in the rotating frame for the case  $N = 8$ . Shown are the pairs of levels consisting of  $|n\rangle$  and  $|N - n\rangle$  each of which is localized in one of the two wells. The corresponding quasienergy states  $|\varphi_n\rangle$  and  $|\varphi_{N-n}\rangle$  are a superposition of the two localized states, see text. The horizontal arrows indicate the multiphoton transitions between the two quasienergy states. The vertical arrows mark the bath-induced transitions with their thickness being proportional to the transition rate. The quasienergy axis indicates that the states on the bottom of this schematic quasipotential have larger quasienergy.

The dynamics can be illustrated with a simple analogy to a double-well potential. Each partner of the pair  $|\varphi_n\rangle$  and  $|\varphi_{N-n}\rangle$  of the quasienergy states consists of a superposition of two harmonic oscillator states  $|n\rangle$  and  $|N - n\rangle$  which are the approximate eigenstates of the static anharmonic potential in the regime of weak nonlinearity. In our simple picture,  $|n\rangle$  and  $|N - n\rangle$  should be identified with two localized states in the two wells of the quasienergy potential, see Fig. 2.5 for illustration. In Subsection 2.3.2, we have derived the quasipotential in Eq. (2.17) by writing the RWA Hamiltonian Eq. (2.13) in terms of the reduced position and momentum operators  $\mathcal{X}_r$  and  $\mathcal{P}_r$ . The right/left well should be identified with the internal/external part of the quasienergy surface shown in Fig. 2.2

In Fig. 2.5, we have chosen  $N = 8$ . Within our analogy, the states  $|0\rangle, |1\rangle, \dots, |N/2 - 1\rangle$  are localized in one (here, the left) well, while  $|N\rangle, |N - 1\rangle, \dots, |N/2 + 1\rangle$  are localized in the other well (here, the right). The fact that the true quasienergy states are superpositions of the two localized states is illustrated by a horizontal arrow representing tunnelling.

From Eq. (2.93) follows that a bath-induced transition is only possible between states belonging to two different neighboring pairs. As discussed after Eq. (2.90), the only contribution to the transition rates comes from nearby HO states. In our case, we consider only spontaneous emission which corresponds to intrawell transitions induced by the bath. This is shown schematically in Fig. 2.5 by the vertical arrows with their thickness being proportional to the transition rates. We emphasize that the bath-induced transitions occur towards lower lying HO states. Consequently, in

our picture, spontaneous decay happens in the left well downwards but in the right well upwards.

The driving field excites the transition from  $|0\rangle$  to  $|N\rangle$  while the bath generates transitions between HO states towards lower energies according to  $|N\rangle \rightarrow |N-1\rangle \rightarrow \dots \rightarrow |0\rangle$  when only spontaneous emission is considered.

As a consequence, the ratio of the occupation numbers of two states belonging to two neighboring pairs is simply given by the ratio of the corresponding transition rates according to

$$\begin{aligned} \varrho_{nn} &= \varrho_{N-n, N-n}, \\ \frac{\varrho_{nn}}{\varrho_{n+1, n+1}} &= \frac{\mathcal{L}_{nn, n+1, n+1}}{\mathcal{L}_{n+1, n+1, nn}} = \frac{n+1}{N-n}. \end{aligned} \quad (2.94)$$

Hence, the unpaired state  $|\varphi_{N/2}\rangle$  (for  $N$  even) or the states  $|\varphi_{(N-1)/2}\rangle$  and  $|\varphi_{(N+1)/2}\rangle$  (for  $N$  odd) are the states with the largest occupation probability. By iteration, one finds

$$\begin{aligned} \varrho_{N/2} &= \left( 1 + 2 \sum_{n=1}^{N/2} \prod_{k=0}^{n-1} \frac{N-2k}{N+2+2k} \right)^{-1} = 0.5, 0.37, 0.31, 0.27, \dots \\ &\text{for } N = 2, 4, 6, 8, \dots, \end{aligned} \quad (2.95)$$

and

$$\begin{aligned} \varrho_{(N\mp 1)/2} &= \left( 2 + 2 \sum_{n=1}^{(N-1)/2} \prod_{k=0}^{n-1} \frac{N-1-2k}{N+3+2k} \right)^{-1} = 0.37, 0.31, 0.27, 0.25, \dots \\ &\text{for } N = 3, 5, 7, 9, \dots \end{aligned} \quad (2.96)$$

### Density matrix of the stationary state around the resonance

So far, we have discussed the dynamics exactly at resonance. Next, we consider the situation around the resonance and for an increased coupling to the bath. Therefore, we compute the stationary solution using the conditions in Eq. (2.88) and the general leading order solution for the quasienergy states given in Eq. (2.26). The expressions

for the rates which are modified compared to before are readily calculated to be

$$\begin{aligned}
\mathcal{L}_{00,11} &= \mathcal{L}_{00,N-1N-1} = \frac{\gamma_s}{2} \cos^2 \frac{\theta}{2}, \\
\mathcal{L}_{NN,11} &= \mathcal{L}_{NN,N-1N-1} = \frac{\gamma_s}{2} \sin^2 \frac{\theta}{2}, \\
\mathcal{L}_{11,00} &= \mathcal{L}_{N-1N-1,00} = \frac{\gamma_s}{2} N \sin^2 \frac{\theta}{2}, \\
\mathcal{L}_{11,NN} &= \mathcal{L}_{N-1N-1,NN} = \frac{\gamma_s}{2} N \cos^2 \frac{\theta}{2}, \\
\mathcal{L}_{00,0N} &= \mathcal{L}_{00,N0} = \mathcal{L}_{NN,0N} = \mathcal{L}_{NN,N0} = \mathcal{L}_{0N,00} = \mathcal{L}_{N0,00} \\
&= \mathcal{L}_{0N,NN} = \mathcal{L}_{N0,NN} = \frac{\gamma_s}{2} N \sin \frac{\theta}{2} \cos \frac{\theta}{2}, \\
\mathcal{L}_{11,0N} &= \mathcal{L}_{11,N0} = \mathcal{L}_{N-1N-1,0N} = \mathcal{L}_{N-1N-1,N0} \\
&= -\frac{\gamma_s}{2} N \sin \frac{\theta}{2} \cos \frac{\theta}{2}, \\
\mathcal{L}_{0N,11} &= \mathcal{L}_{N0,11} = \mathcal{L}_{0N,N-1N-1} = \mathcal{L}_{N0,N-1N-1} \\
&= \frac{\gamma_s}{2} \sin \frac{\theta}{2} \cos \frac{\theta}{2}.
\end{aligned} \tag{2.97}$$

Similarly, there are only three equations which change compared to the previous situation. They read

$$\begin{aligned}
0 &= -N \sin^2 \frac{\theta}{2} \varrho_{00} + \cos^2 \frac{\theta}{2} \varrho_{11} + N \cos \frac{\theta}{2} \sin \frac{\theta}{2} \varrho_{N0}, \\
0 &= -N \cos^2 \frac{\theta}{2} \varrho_{NN} + \sin^2 \frac{\theta}{2} \varrho_{11} + N \cos \frac{\theta}{2} \sin \frac{\theta}{2} \varrho_{N0}, \\
0 &= -i\Omega(\Delta) \varrho_{N0} + \frac{\gamma_s}{2} \left[ -N \varrho_{N0} + \cos \frac{\theta}{2} \sin \frac{\theta}{2} (N \varrho_{00} + N \varrho_{NN} + 2 \varrho_{11}) \right],
\end{aligned} \tag{2.98}$$

with the quasienergy level splitting

$$\Omega(\Delta) = \varepsilon_N - \varepsilon_0 = -\text{sgn}(\Delta) \left[ \left( \frac{\nu(N+1)}{2} N \Delta \right)^2 + \Omega_{N,0}^2 \right]^{1/2}. \tag{2.99}$$

These equations can be straightforwardly solved by

$$\begin{aligned}
\varrho_{00} &= \left[ \frac{1}{N} \cot^2 \frac{\theta}{2} + \frac{Ng^2}{2} \cos^2 \frac{\theta}{2} \left( 1 + \frac{1}{2} \tan^2 \frac{\theta}{2} + \frac{1}{2} \cot^2 \frac{\theta}{2} \right) \right] \varrho_{11}, \\
\varrho_{NN} &= \left[ \frac{1}{N} \tan^2 \frac{\theta}{2} + \frac{Ng^2}{2} \sin^2 \frac{\theta}{2} \left( 1 + \frac{1}{2} \tan^2 \frac{\theta}{2} + \frac{1}{2} \cot^2 \frac{\theta}{2} \right) \right] \varrho_{11}, \\
\varrho_{N0} &= g \sin \frac{\theta}{2} \cos \frac{\theta}{2} \left( \frac{N}{2} g - i \right) \left( 1 + \frac{1}{2} \tan^2 \frac{\theta}{2} + \frac{1}{2} \cot^2 \frac{\theta}{2} \right) \varrho_{11}.
\end{aligned} \tag{2.100}$$

Here,  $g = \gamma_s/\Omega(\Delta)$  has been defined as the ratio between the damping strength and the Raby frequency of the narrowest avoided crossing. Away from the resonance ( $|\theta| \ll 1$ ), the density matrix follows as

$$\varrho \simeq |\varphi_0\rangle\langle\varphi_0| \simeq |0\rangle\langle 0|. \tag{2.101}$$

In the limit of strong coupling corresponding to  $g \gg 1$ , one finds

$$\varrho \simeq \cos^2 \frac{\theta}{2} |\varphi_0\rangle\langle\varphi_0| + \sin^2 \frac{\theta}{2} |\varphi_N\rangle\langle\varphi_N| + \sin \frac{\theta}{2} \cos \frac{\theta}{2} (|\varphi_0\rangle\langle\varphi_N| + |\varphi_N\rangle\langle\varphi_0|) = |0\rangle\langle 0|, \quad (2.102)$$

for any  $\theta$ . In the opposite limit  $g \ll 1$  and for  $\theta \approx \pi/2$  (near resonance) we recover the solution in Eq. (2.94) characterized by a large occupation of the unpaired state  $|\varphi_{N/2}\rangle$  (for  $N$  even) or the states  $|\varphi_{(N-1)/2}\rangle$  and  $|\varphi_{(N+1)/2}\rangle$  (for  $N$  odd).

These results can be interpreted in the framework of the analogy to the double-well potential carried out in the previous section. Starting from the bottom of the right well, dissipation causes transitions towards the top of the right well and subsequently towards the bottom of the left well and tends to populate the state  $|0\rangle$  at the bottom of the left well. On the other hand, tunnelling causes transition from the left to the right well and vice versa. Away from resonance, the tunnelling from the state at the bottom of the left well to the bottom of the right well is not possible and the resonator gets stuck at the bottom of the left well. Near resonance the stationary solution results from a competition between dissipation and driving induced tunnelling to the state  $|N\rangle$ . For  $g \gg 1$ , the dissipation is much faster than tunnelling and at equilibrium we expect the oscillator to populate the state  $|0\rangle$ . On the other hand for  $g \ll 1$  and  $\theta \approx \pi/2$ , the tunnelling is much faster than dissipation and since the dissipation towards the top of the right well is faster than the one towards the bottom of the right well, an higher population of the states at the top of the quasipotential results.

In the next subsection we will derive an analytical expression for the lineshape of the multi-photon resonances when  $\alpha \approx 0.01$  or less, being consistent with the RWA. In this limit there are multiple avoided level crossings at the same driving frequency. Nevertheless only the  $N$ -photon transition is crucial for the mechanism illustrated above. For this reason, we expect the analytically computed lineshape to yield a qualitatively correct picture also for stronger anharmonicity, when the degeneracy of the avoided level crossing is lifted. We shall prove this statement by numerically calculating the lineshape for  $\alpha \approx 0.1$  in Section 2.6.

### Lineshape around the resonance

Within our partial secular approximation, the lineshape of the oscillator's nonlinear response given in Eq. (2.85) reduces to

$$A = \sqrt{2}x_0 \left| \sum_{\alpha\beta} \varrho_{\alpha\alpha} A_{\alpha\alpha} + \varrho_{0N} A_{0N} + \varrho_{N0} A_{N0} \right|. \quad (2.103)$$

The leading order is given by the zeroth order expression for  $\varrho$  and the first-order expressions for  $A_{\alpha\alpha}$ ,  $A_{N0}$  and  $A_{0N}$ . In order to compute these matrix elements, we determine the first order eigenvectors using Van Vleck perturbation theory according to

$$|\varphi_0\rangle_1 = e^{i\varepsilon S_1} |\varphi_0\rangle_0, \quad (2.104)$$

where  $S_1$  is the first order component in the expansion of  $S$  with respect to  $\varepsilon$  given in Eq. (2.21). The matrix elements of its off-diagonal blocks are given by

$$\langle \alpha | S_1 | \beta \rangle = -i \frac{\langle \alpha | V | \beta \rangle}{E_\beta - E_\alpha}. \quad (2.105)$$

Here,  $E_\alpha$  are the eigenenergies of the unperturbed Hamiltonian  $H_0$  given in Eq. (2.20). This yields for  $N = 2$

$$\begin{aligned} A_{00} &= 3\varepsilon \left( 1 - 2\sqrt{2} \sin \frac{\theta}{2} \cos \frac{\theta}{2} \right), & A_{22} &= 3\varepsilon \left( 1 + 2\sqrt{2} \sin \frac{\theta}{2} \cos \frac{\theta}{2} \right), \\ A_{02} &= 6\sqrt{2}\varepsilon \cos^2 \frac{\theta}{2} & A_{20} &= -6\sqrt{2}\varepsilon \sin^2 \frac{\theta}{2}, & A_{11} &= -9\varepsilon. \end{aligned} \quad (2.106)$$

The corresponding result for the nonlinear response for  $N = 2$  is shown in Fig. 2.6 for the case  $\nu = 10^{-3}$  and  $f = 10^{-4}$  for different values of  $\gamma_s/\Omega_{2,0}$ . For strong damping  $\gamma_s/\Omega_{2,0} = 5$ , the resonance is washed out almost completely. Decreasing damping, a resonant lineshape appears whose maximum is shifted compared to the resonance condition  $\omega_{\text{ex}} = \omega_1 + 3\nu/2$ . Note that the dashed line refers to the result which includes all orders in  $\varepsilon$  and which follows from the numerical solution of the master equation for an Ohmic bath at temperature  $T = 0.1T_0$ .

The picture which arises for the behavior is the following: For weak damping ( $\gamma_s \ll \Omega_{2,0}$ ), the equilibrium state is a statistical mixture of quasienergy states. At resonance, the most populated state is  $|\varphi_1\rangle$  which oscillates with a phase difference of  $-\pi$  in comparison with the driving. This is due to the negative sign of  $A_{11}$  in Eq. (2.106). Hence, at resonance the overall oscillation of the observable occurs with a phase difference of  $\varphi = -\pi$ . Far away from resonance, the most populated state is  $|\varphi_0\rangle$ , see Eq. (2.101), which oscillates in phase with the driving. Thus, the overall oscillation occurs in phase, i.e.,  $\varphi = 0$ . If no off-diagonal element of the density matrix is populated (which is the case for weak damping), the overall phase is either  $\varphi = 0$  or  $\varphi = -\pi$ . Hence, increasing the distance from resonance, the amplitude  $A$  has to go through zero yielding a cusp-like line-shape. This implies the existence of a maximum in the response. For slightly larger damping, the finite population of the off-diagonal elements leads to a smearing of the cusp. For larger damping, the resonance is washed out completely, as has been already discussed, see Eq. (2.102). In this regime, the oscillation is in phase with the driving. By decreasing the damping, the population of the out-of-phase state starts to increase near the resonance resulting in a reduction of the in-phase oscillation and thus producing a minimum of the response.

Let us now consider the case of an arbitrary resonance  $N > 2$ . A straightforward calculation yields

$$A_{N/2N/2} = -\varepsilon(N+1)^2 \quad A_{(N\pm 1)/2} = \pm \frac{1}{2} \sqrt{\frac{N+1}{2}} - \varepsilon \frac{(N+1)^2}{4}. \quad (2.107)$$

Hence an occupation of the states at the top of the quasipotential results in an  $-\pi$  out-of-phase response. With a detailed calculation it can be proved that at equilibrium and for  $\theta \approx \pi/2$  and  $g \ll 1$  these states dominates the dynamics, and an overall

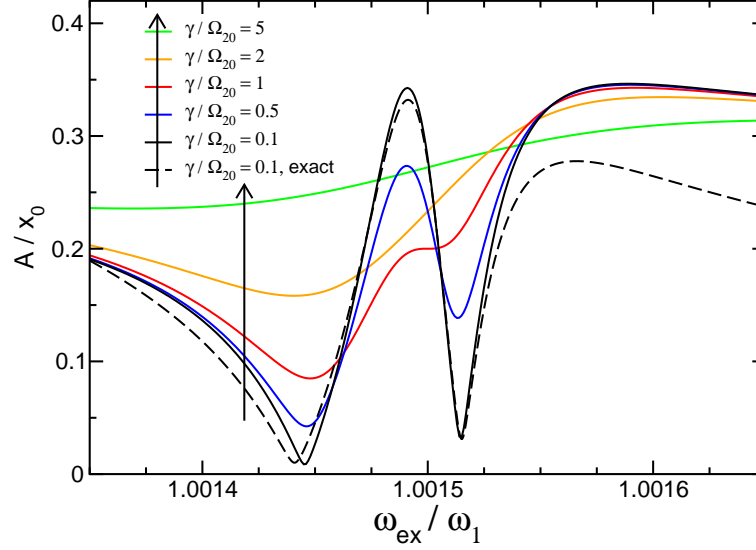


**Figure 2.6:** Nonlinear response at the two-photon resonance  $N = 2$ , where  $\omega_{\text{ex}} = \omega_1 + 3\nu/2$  for the parameters  $\mu = 10^{-4}$  and  $\nu = 10^{-3}$  (in dimensionless units) for different values of the damping.

out-of-phase oscillation results. Note that a calculation up to first order in  $\varepsilon$  for the density matrix is required for  $N$  odd, since the matrix elements  $A_{(N\pm 1)/2(N\pm 1)/2}$  have a zero-th order term, in order that the overall result for  $A$  is again of first order in  $\varepsilon$ . We omit this cumbersome and scarcely illuminating calculation. However, since all the other Floquet states oscillates in-phase it is clear that also in this case a transition to an in-phase antiresonant response is expected.

Some remarks on the observability of such high photon number resonances are in order. The size of the Rabi frequency  $\Omega_{N,0}$  for the  $N$ -photon transition is crucial. In fact, it specifies both the width of the transition and the order of magnitude of the coupling to the bath, which is compatible to the observability of this quantum effect. Its perturbative expression, given in Eq. (2.24), is of  $N$ -th order in  $\varepsilon$ . In Fig. 2.7, we show the behavior for  $N = 3$  for various damping constants  $\gamma_s/\Omega_{3,0}$  for the case  $\mu = 0.5 \times 10^{-4}$  and  $\nu = 10^{-3}$  corresponding to  $\varepsilon = 0.025$  and  $\Omega_{3,0} = 0.7 \times 10^{-7}$ . For such a small  $\varepsilon$  there is a good agreement between the perturbative solution, and the exact solution. However, for  $\gamma_s/\Omega_{3,0} = 5$  corresponding to  $\gamma_s = 0.35 \times 10^{-6}$ , the resonance is washed out completely. Only when the damping is decreased, a dip appears which corresponds to an antiresonance. Decreasing the damping further, the antiresonance turns into a clear resonance. However an oscillator with a quality factor  $Q \approx 10^8$  is required to observe such a resonance. Although the experimental techniques are evolving rapidly, such high quality factors seem very difficult to achieve in a near future. Hence, it seems more relevant for the experiments to consider larger driving strengths yielding larger Rabi frequencies. For this reason, in the next section we will leave our analytical perturbative approach and treat the system dynamics exactly

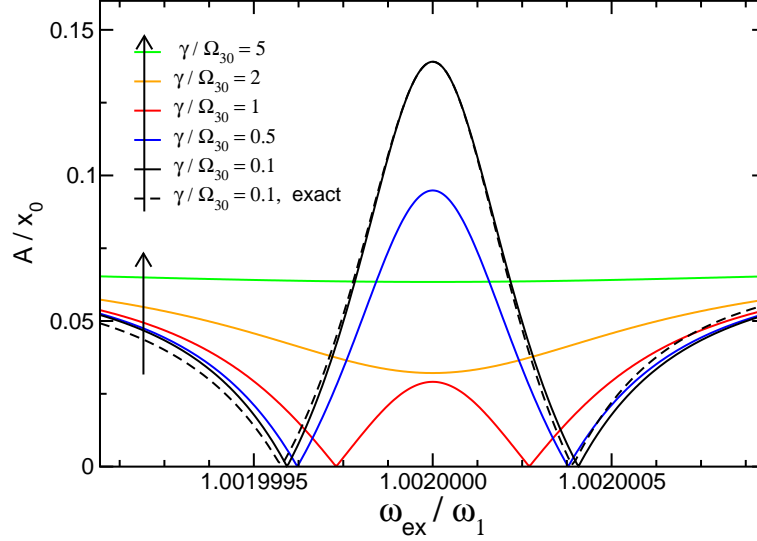


**Figure 2.7:** Nonlinear response at the three-photon resonance  $N = 3$ , where  $\omega_{\text{ex}} = \omega_1 + 2\nu$  for the parameters  $\mu = 0.5 \times 10^{-4}$  and  $\nu = 10^{-3}$  (in dimensionless units) for different values of the damping.

by diagonalizing numerically the Floquet Hamiltonian given in Eq. (2.9).

## 2.6 Numerical results in the strong driving regime

In this section we solve numerically the Floquet master equation (2.76). We will show that the physical picture that arises from the analytical perturbative treatment of Sections 2.3.2 and 2.5 allows to interpret the lineshape and the phase response of the quantum Duffing oscillator for a broad range of parameters, including larger  $N$ , larger  $T$  and larger  $\varepsilon$ . Moreover we will investigate the tunnelling dynamics near the stationary regime, which prevents the bistability of the classical Duffing oscillator to show up in the quantum regime.

We first compute the quasi-energies  $\varepsilon_\alpha$  and the Floquet states  $|\phi_\alpha(t)\rangle$  as outlined at the end of Section 2.3.1. Thereby, we truncate the total Hilbert space of the anharmonic resonator to its  $\mathcal{N}$ -dimensional lowest energy subspace. We then compute the matrix elements, defined in Eqs. (2.68) and (2.73), which are needed to evaluate the operator  $\mathcal{S}$  in Eq. (2.76). This is a  $\mathcal{N}^2 \times \mathcal{N}^2$ -matrix and can be readily diagonalized numerically by standard means. In order to be definite, we consider Ohmic damping only. However, according to the discussion in the previous section, the results are not expected to change qualitatively in the case of a super-Ohmic bath. For practical purposes, we set  $\mathcal{N} = 12$  throughout this part. Note that we have confirmed convergence with respect to  $\mathcal{N}$  for all results shown below.

The stationary solution of Eq. (2.78) corresponds to a zero eigenvalue of  $\mathcal{S}$ .



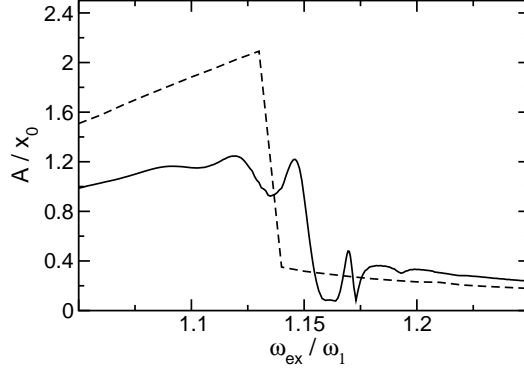


**Figure 2.8:** Amplitude  $A$  of the expectation value  $\langle x(t) \rangle$  in units of  $x_0 = \sqrt{\frac{\hbar}{m\omega_1}}$  for varying the driving frequency  $\omega$ . Parameters are  $k_B T = 0.1\hbar\omega_1$ ,  $\alpha = 0.1\alpha_0$ ,  $f = 0.1f_0$ ,  $\gamma = 0.005\omega_1$ . Dashed line: Results of the classical Duffing oscillator at  $T = 0$  with the remaining parameters being the same.

The remaining eigenvalues all have a negative real part leading to a decay of the corresponding mode with time. Due to the structure of the master equation (2.76), there exist two classes of eigenvalues: (i) the first class having an imaginary part of zero consists of individual eigenvalues (associated to *relaxation*), and (ii) the second class having non-zero imaginary parts (associated to *dephasing*) consists of pairs of complex conjugated eigenvalues. The eigenvalues can be ordered according to the size of the absolute value of their real parts. As it turns out, there is one eigenvalue, corresponding to a relaxation process, with the smallest non-zero absolute value of the real part. Moreover, we find that its real part, which we denote by  $\Gamma$ , is clearly separated in size from the remaining ones indicating a separation of time scales. That eigenvalue is responsible for the tunnelling dynamics at long times, as will be discussed in Section 2.6.3.

### 2.6.1 Amplitude and phase response

A typical response profile for the amplitude  $A(\omega)$  as a function of the driving frequency is shown in Fig. 2.8. For increasing driving frequency, the lineshape shows: (i) several broad resonances, (ii) a dramatic decrease of the response, showing a shoulder-like shape remnant of the classical form of the response (indicated by the dashed line), (iii) a sharp resonance and (iv) an antiresonance. The associated quasienergy spectrum, shown in Fig. 2.9 a), displays multiple avoided level crossings of the quasienergies in correspondence of the distinct resonances and the antiresonance. By switching-off adiabatically the driving strength, we label the different quasienergy level with the quantum number  $n$  associated with the unperturbed levels of the nonlinear oscillator. Thereby, we can identify each avoided crossing with a multiphoton process. For the moderate value of the nonlinearity considered here ( $\alpha = 0.1\alpha_0$  for all the simulations in this section), the avoided crossings are no longer degenerate. However, the driving strength is also rather strong ( $f = 0.1f_0$ ) and the

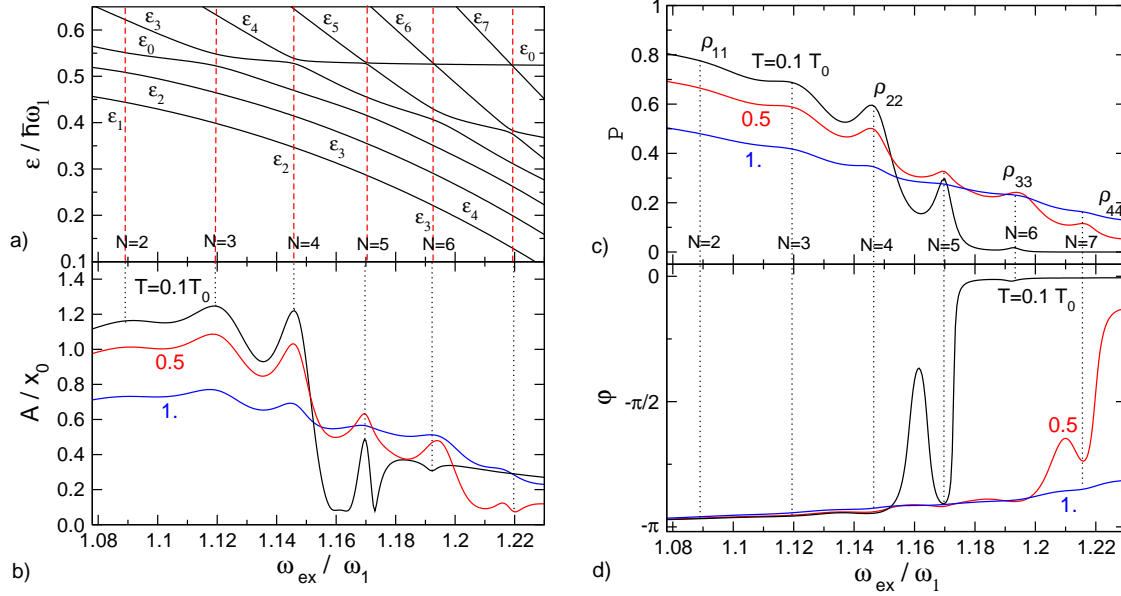


**Figure 2.9:** a) Quasienergy levels  $\varepsilon_\alpha(\omega_{\text{ex}})$ , b) amplitude  $A(\omega_{\text{ex}})$  of the fundamental mode, c) occupation probability of the Floquet state oscillating out-of-phase  $P(\omega_{\text{ex}})$ , d) overall phase response  $\varphi(\omega_{\text{ex}})$  (bottom right) for different temperatures. The remaining parameters are  $\alpha = 0.1\alpha_0$ ,  $f = 0.1f_0$  and  $\gamma = 0.005\omega_1$ .

widths of the broader multiphoton transitions result to be much larger than their displacements from the narrowest one. We label each resonance with the number  $N$  of photon exchanged in the transition corresponding to the narrowest avoided crossing of the levels  $\varepsilon_N$  and  $\varepsilon_0$ . Near a resonance corresponding to  $N$  even, the level with the lowest quasienergy is associated to the  $N/2$ -th Floquet state and is unpaired. At the following resonance  $N' = N + 1$  (odd), it displays an avoided crossing with the level corresponding to the  $(N' + 1)/2$ -Floquet state and the two levels exchange their labels. The lowest energy level switch from the  $N/2 = (N' - 1)/2$ -Floquet state to the  $(N' + 1)/2$ -Floquet state. Hence the lowest quasienergy level, in Fig. 2.9 a), corresponds to the state, which has the largest occupation probability around the resonances and is responsible for the large out-of-phase oscillation, in the limit of weak nonlinearities and weak driving.

In this moderate driving regime, we do not expect the perturbative result for the stationary density matrix to be accurate. However, the occupation probability of such a state, shown in Fig. 2.9 c), displays clear peaks around the resonance frequencies. To each of these peaks corresponds a minimum close to  $-\pi$  in the phase response, shown in figure 2.9 d). This suggest that the interpretation, carried out in Section 2.5, of the resonances and the antiresonances, as a result of competing out-of-phase and in-phase oscillations of different Floquet states is still valid in this moderate nonlinearity and driving regime. In fact, this picture explains qualitatively the different structures present in the lineshape of the response:

(i) For frequency corresponding to  $N$  small ( $N = 2, 3$ ) where broad resonances are

present, the population of the lowest quasienergy level decreases while moving away from one resonance. However, the transition to an in-phase oscillation is not possible, because the degenerate avoided crossings associated with the next resonance are very broad, and they readily cause an increase of the occupation of the lowest energy state while approaching the resonance. In this regime the overall phase of the oscillation stays close to  $-\pi$ .

(ii) While moving away from the 4-photon resonance, the population of the lowest quasienergy state decreases sharply, correspondingly the phase increases up to  $\varphi \approx -\pi/2$  indicating that the contribution of the in-phase Floquet states and the out-of-phase Floquet state to the overall oscillation cancel out. The amplitude does not vanish due to non-vanishing coherences in the stationary state, which yield a small oscillation. The transition to an overall in-phase oscillation is blocked by the influence of the the next group of avoided crossings corresponding to the 5-photon resonance.

(iii) Around this resonance the population of the lowest energy state displays a clear peak, correspondingly the phase defines a minimum close to  $-\pi$  and the amplitude has a sharp maximum.

(iv) Moving away from the 5-photon resonance the occupation probability of the state oscillating out-of-phase decreases down to zero, while the overall phase increases up to zero: only states oscillating in-phase are occupied. Around the 6-photon resonance the occupation probability of the out-of-phase state displays a small maximum. The corresponding out-of-phase oscillation partially cancel the dominating in-phase oscillation, yielding an antiresonance.

### 2.6.2 Interplay between dissipation and tunnelling

In the limits of validity of the leading order RWA, we have interpreted the large occupation at resonance of the state oscillating out-of phase in terms of the analogy between this system and a static double-well potential. This analogy is based, in first place, on the similarity of the quasienergy spectrum of the driven nonlinear oscillator to the energy spectrum of the double well potential. The quasienergy (energy) levels of both systems display multiple avoided crossings for certain value of the control parameter (the driving frequency or a static bias for the driven oscillator and the double well, respectively). In correspondence to these multiple avoided crossings, each pair of eigenstates of the double well potential, whose energy levels are displaying an avoided crossing, is given by the symmetric and the antisymmetric superposition of two states localized in opposite wells. Correspondingly, the pair of states of the driven oscillator, whose quasienergy levels display the avoided crossing associated with the  $(N - 2n)$ -photon transition, is the superposition of the eigenstates of the harmonic oscillator in the rotating frame  $|N - n\rangle$  and  $|n\rangle$  ( $n < N/2$ ). It is thus natural to identify the two opposite wells as the set  $\{|N - n\rangle\}$  and  $\{|n\rangle\}$  respectively, with the state  $|N/2\rangle$  sitting on top of the two well (for  $N$  even). Such an identification sheds light to the other central similarity between the two systems: the bath induced dissipation induces intrawell transitions only. In fact, we can read from the transition rates in Eq. (2.90), that two states localized in opposite wells

have a vanishing transition rate. In contrast to a real static double-well potential the dissipation induces transitions toward the top of the potential in one well (corresponding to the set  $\{|n\rangle\}$ , we refer to this set as ‘right’ well) and toward the bottom in the other well (corresponding to the set  $\{|N - n\rangle\}$ , we refer to this set as ‘left’ well) when only spontaneous emission is taken into account. Hence, dissipation tends to populate the state at the bottom of the ‘right’ well (that we have identified with the groundstate of the harmonic oscillator in the rotating frame).

At resonance, this mechanism is competing with tunnelling, which induces transition from the bottom of the ‘right’ well to the bottom of the ‘left’ well. When tunnelling is faster than dissipation the states at the top of the potential are favored because dissipation is faster in the ‘right’ well than in the ‘left’ well (see the transition rates in Eq. (2.93)). The time scale of this tunnelling transition and of dissipation are set by the inverse Rabi frequency of the narrowest avoided crossing  $\Omega_{N,0}^{-1}$  and the inverse coupling to the bath  $\gamma^{-1}$ . Away from the narrowest resonance, the tunnelling from the state at the bottom of the ‘left’ well to the right well is not possible and the oscillator is blocked in the ‘right’ well. The results for the quasienergy spectrum, the occupation of the state oscillating out-of-phase, the amplitude and the phase response indicate that a similar mechanism is present beyond the limit of validity of the leading order low temperature RWA. The investigation of such a mechanism is the focus of this section.

First, we check that the physics is still governed by the ratio between the Rabi frequency of the narrowest avoided crossing and the coupling to the bath, by considering the response at the multiple avoided crossings associated with the 6-photon antiresonance for varying coupling  $\gamma$ . We expect a transition from the in-phase antiresonant to the out-of-phase resonant behavior, when  $\gamma \approx \Omega_{N,0}$ . The amplitude and phase responses for different damping constants  $\gamma$  are shown in Fig. 2.10. The 6-photon antiresonance turns into a resonance when  $\gamma$  is decreased below the critical value  $\gamma_c = 0.001$ . For the same value of  $\gamma$ , the minimum in the phase response approaches  $-\pi$  indicating out-of-phase oscillation. The Rabi frequency  $\Omega_{6,0} \simeq 0.0005$ , given by the minimal splitting of the narrowest avoided crossing, shown in the inset of Fig. 2.10, is of the same order of magnitude, whereas the Rabi frequency of the second narrowest avoided crossing  $\Omega_{6,1} = 0.02$  is much larger than the threshold value of  $\gamma$ . This is the only resonance which is well separated from all the others, and is best suited to be compared with the analytical results of Section 2.5. The similarity with the 3-photon resonance in Fig 2.7 is striking.

However, two important differences can be noticed after a careful inspection: First, the resonant behavior seems to be compatible with a stronger coupling to the bath. In fact, here, we have  $\Omega_{6,0}/\gamma_c = 0.5$ , whereas for the 3-photon resonance in the RWA it is  $\Omega_{6,3}/\gamma_c = 2$ . Second, the width of the antiresonance is much larger than the width of the resonance. The width of the resonance, as expected, is related to  $\Omega_{6,0}$ , whereas the width of the antiresonance seems more close to the Rabi frequency of the second narrowest avoided crossing  $\Omega_{6,1}$ . These two observations indicate that the low temperature RWA neglects some mechanisms, which favor the resonant behavior and allow a small population of the out-of-phase state even far away from the narrowest avoided crossing. This mechanism can be identified with

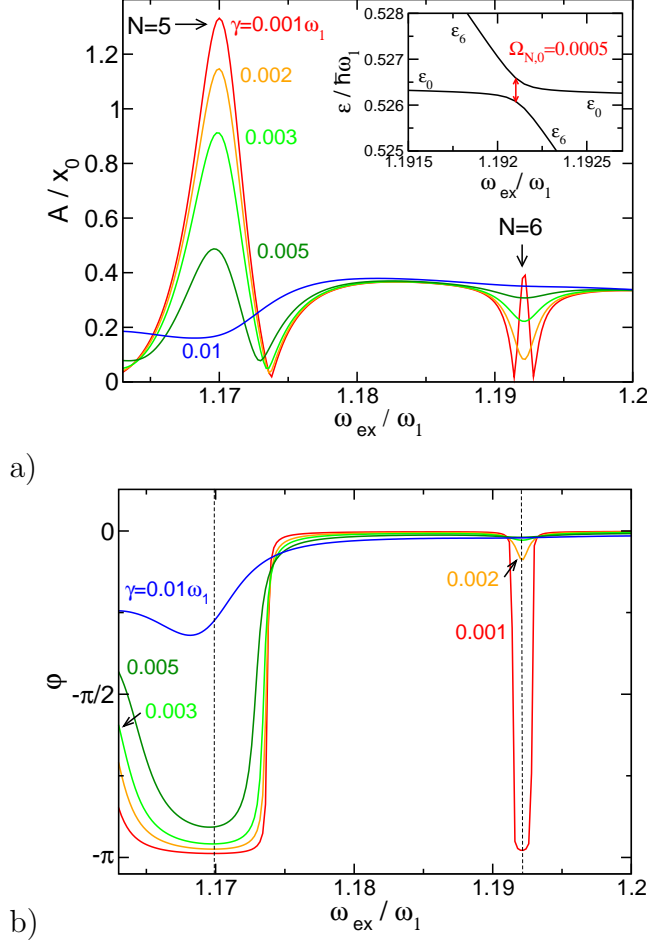


**Figure 2.10:** a) Five- and six-photon resonance of the response curve  $A(\omega_{\text{ex}})$  for different values of the damping constant  $\gamma$ . The inset shows the narrowest avoided crossing at the 6-photon resonance. Remaining parameters are  $f = 0.1f_0$ ,  $\alpha = 0.1\alpha_0$ ,  $T = 0.1T_0$ . b) Phase response  $\varphi(\omega_{\text{ex}})$  for the same parameter as above. The dashed vertical lines mark the  $N = 5$ - and the  $N = 6$ -photon transition.

a finite transition rate from the bottom of the ‘left’ well to its first excited state. Away from the narrowest avoided crossing, the presence of such a transition permits a subsequent  $(N - 2)$ -photon tunnelling process associated to the second narrowest avoided crossing. Consequently the system can escape from the ‘right’ well and a finite occupation of the state at the top of the quasipotential is expected even away from the narrowest avoided crossing. This scenario is illustrated schematically in Fig. 2.11.

### Temperature assisted tunnelling

An obvious mechanism yielding a transition from the bottom of the right well to its first excited state and a consequent broadening of the resonances (antiresonances) is the absorption of one photon from the bath. Such thermal processes can be neglected only when  $T \ll T_0$ . The effect of an increasing temperature on the 5-photon and 6-photon resonances is shown in Fig. 2.12. When temperature is increased from  $T = 0.1T_0$  to  $T = 0.2T_0$  the effect of the enhancement of the thermal processes is negligible around the 5-photon resonance whereas it is visible around the antiresonance. The reason is that when the oscillator is blocked in the ‘right’ well even a small increase in the thermal transition rate from the bottom of the ‘right’

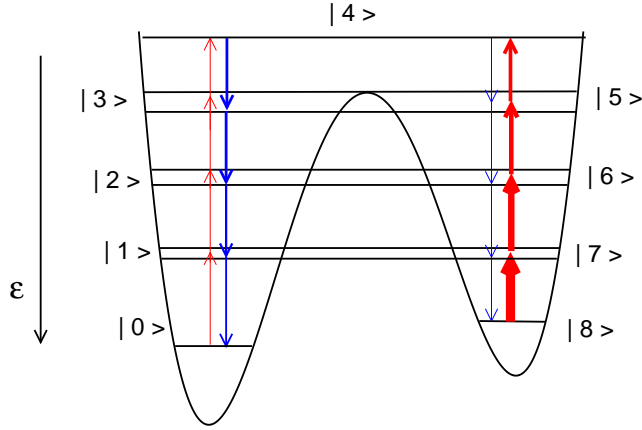


**Figure 2.11:** Schematic view of the quasipotential and localized states in the rotating frame for the case  $N = 8$  away from the narrowest avoided crossing. There are three pairs of extended states, but the two states at the bottom of the quasi-potential are localized in one well. The vertical arrows mark the bath-induced transitions with their thickness being proportional to the transition rate. The quasienergy axis indicates that the states on the bottom of this schematic quasipotential have larger quasienergy.

well activates the 4-photon tunnelling to the ‘left’ well and changes dramatically the stationary solution. This is even more apparent when the temperature is further increased and a transition to a resonant out-of-phase oscillation is observed. Such a behavior is clearly due to the interplay of a thermal transition to the first excited state of the ‘right’ well and the 4-photon tunnelling to the ‘left’ well.

### Driving induced dissipation

By increasing the driving strength, the multiple avoided crossings become broader, thereby enhancing resonant tunnelling. The increased tunnelling rate leads obviously to a broadening of the resonances in the amplitude response. However, there is a more subtle mechanism leading to the broadening of the resonances. When the driving is increased above the weak driving limit, a bath induced transition from the bottom of the ‘right’ well becomes possible and the  $(N - 2)$ -photon transition is activated as for the temperature assisted tunnelling. In fact, the assumption that the relaxation takes place towards the bottom (top) of the ‘right’ (‘left’) well is not based only in disregarding the thermal processes but also in using the leading order RWA. Within this approximation the two Floquet states in the rotating frame  $|\varphi_N\rangle \equiv e^{i\omega_{\text{ex}} a^\dagger at} |\phi_N(t)\rangle$  and  $|\varphi_0\rangle \equiv e^{i\omega_{\text{ex}} a^\dagger at} |\phi_0\rangle$ , which correspond to the pair of levels displaying the avoided crossing associated with the  $N$ -photon transition, are a superposition of the eigenstates of the harmonic oscillator in the rotating frame  $|N\rangle$  and  $|0\rangle$ . Exactly at resonance,  $|\varphi_N\rangle$  and  $|\varphi_0\rangle$  are given by a symmetric and an antisymmetric superposition, respectively, leading to a finite transition rate to

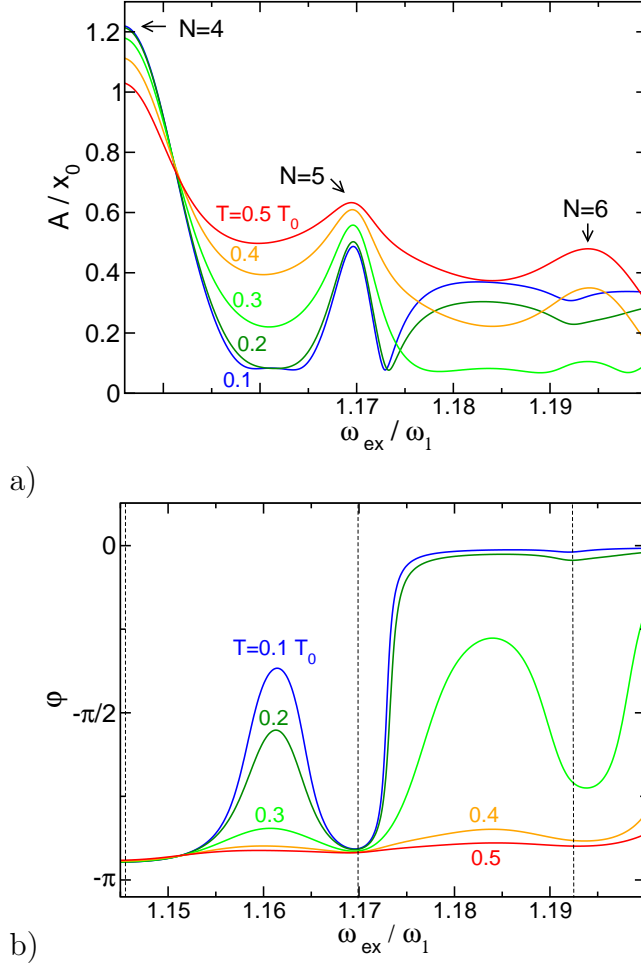


**Figure 2.12:** a) Five- and six-photon resonance of the response curve  $A(\omega_{\text{ex}})$  for different values of the temperature  $T$ . The six-photon resonance develops from an antiresonance for low  $T$  to a true resonance for higher  $T$ . Remaining parameters are  $f = 0.1f_0$ ,  $\alpha = 0.1\alpha_0$ ,  $\gamma = 0.005\omega_1$ . b) Phase shift  $\phi(\omega_{\text{ex}})$  for the same parameters as above. The dashed vertical lines mark the  $N = 5$ – and the  $N = 6$ –photon transition.

the states  $|\varphi_{(N-1)}\rangle \equiv e^{i\omega_{\text{ex}}a^\dagger t}|\phi_{(N-1)}(t)\rangle$  and  $|\varphi_1\rangle \equiv e^{i\omega_{\text{ex}}a^\dagger t}|\phi_1(t)\rangle$  (see Eqs. (2.90) and (2.93)). Away from resonance,  $|\varphi_0\rangle \simeq |0\rangle$  and at low temperature no bath-induced transition from this state is possible and at equilibrium the oscillator is stuck in this state. However, already at second order in perturbation theory a finite tunnelling rate to the states  $|\varphi_{N-1}\rangle$  and  $|\varphi_1\rangle$  is possible activating the broader  $(N-2)$ –photon transition. When moderate driving strengths are considered, this mechanism is favored also by the terms in the driving part of the Hamiltonian, which are fast oscillating in the rotating frame and are neglected in the RWA Hamiltonian Eq. (2.13). When also these terms are considered, the full Floquet solution are time-dependent also in the rotating frame. They can be expressed as vectors of the extended Hilbert space  $\mathcal{R} \otimes \mathcal{T}$ , as seen in Section 2.3.1. The general form in terms of the harmonic oscillator eigenstates  $|n\rangle$  and the  $m$ –photon state  $|m_\tau\rangle$  of the driving field is  $|\phi_\alpha\rangle = \sum_{n,m} c_{n,m}|n\rangle \otimes |m_\tau\rangle$ . The index  $n$  in the sum appearing in the dissipative transition rates Eq. (2.77) refers to the number of photons exchanged in the corresponding process.  $n > 0$  ( $n < 0$ ) corresponds to the emission (absorption) of  $n$ –photon from the driving field to the bath.

Within the RWA, the only relevant transitions describe the emission (absorption) of one photon always associated to the increment (reduction) of the harmonic oscil-

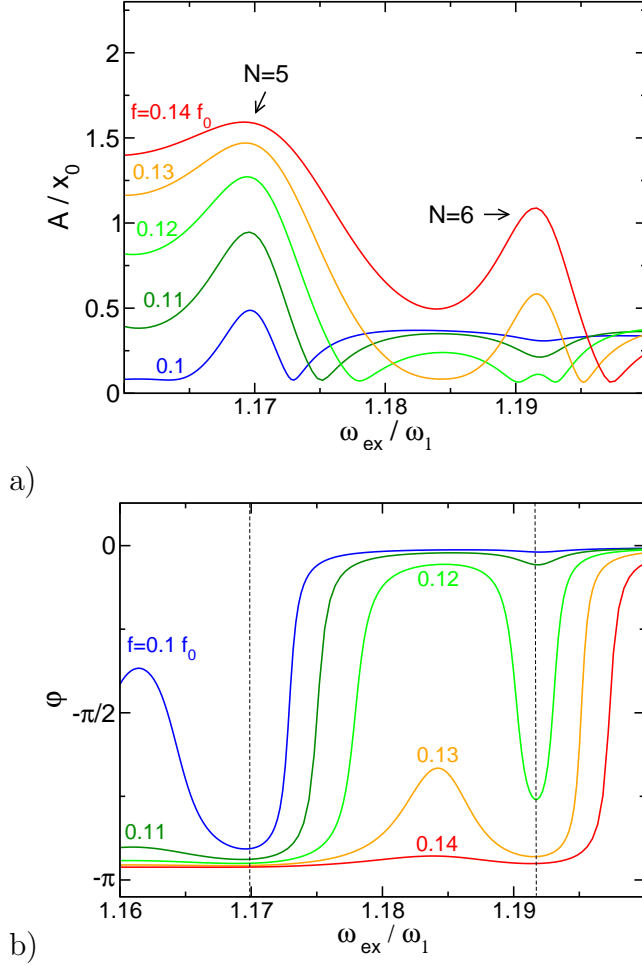


**Figure 2.13:** a) Five- and six-photon resonance of the response curve  $A(\omega_{\text{ex}})$  for different values of the driving amplitude  $f$ . The six-photon resonance develops from an antiresonance for small driving strengths to a true resonance for larger values of  $f$ . Remaining parameters are  $k_B T = 0.1\hbar\omega_1$ ,  $\alpha = 0.1\alpha_0$ ,  $\gamma = 0.005\omega_1$ . b) Phase response  $\phi(\omega_{\text{ex}})$  for the same parameter as above. The dashed vertical lines mark the  $N = 5$ – and the  $N = 6$ –photon transition.

lator occupation number by one. This is in general not true when stronger driving is considered. Even in the low temperature limit  $T \ll T_0$ , the excitation to a state with an higher occupation number is possible, when such a process is associated to the spontaneous emission of  $n$  photons from the driving field to the bath. Such low temperature bath-induced processes, as the thermal processes considered in the previous section, can activate the  $(N - 2)$ –photon transition, yielding a broadening of the resonances. The effect of an increasing driving strength on the 5–photon and the 6–photon resonance is shown In Fig. 2.13, the 5–photon resonance becomes broader while its phase shift approaches  $-\pi$ . The 6–photon antiresonance turns into a resonance while its phase shift varies from  $\simeq 0$  to  $\simeq -\pi$ .

### 2.6.3 Quantum relaxation in the driving induced bistability

The dynamic bistability of the steady state of the classical Duffing oscillator does not survive in the quantum system. The reason is that the system will escape the metastable state asymptotically via tunnelling, similar to the case of the driven double-well potential [97]. Note also that, as a consequence, the hysteretic behavior is suppressed if the control parameter  $\omega_{\text{ex}}$  is varied truly adiabatically.



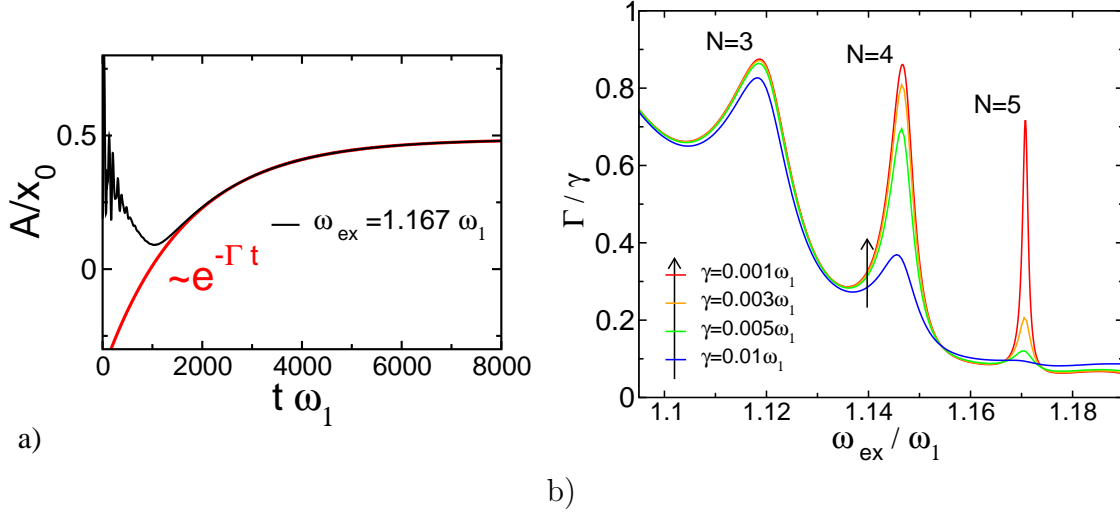


**Figure 2.14:** a) Time-resolved dynamics of the amplitude  $A$  for  $\omega_{\text{ex}} = 1.167\omega_1$  (black solid line). Fast transient oscillations occur as relaxation in the metastable well. The long-time dynamics is governed by a slow exponential decay to the globally stable state characterized by a rate  $\Gamma$  (relaxation rate). The red solid line shows a fit to an exponential  $e^{-\Gamma t}$ . The other parameters are:  $\alpha = 0.1\alpha_0$ ,  $f = 0.1f_0$ ,  $k_B T = 0.1\hbar\omega_1$  and  $\gamma = 0.005\omega_1$ . b) Relaxation rate  $\Gamma$  as a function of the driving frequency for different damping strengths. The peaks correspond to resonant tunnelling in the dynamic bistability. The other parameters are the same as in a).

Nevertheless, signatures of the dynamic bistability and tunnelling can be found if we consider how the steady state is reached. For this, we show in Fig. 2.14 a) the time evolution of the amplitude  $A$  (local maxima of the vibrations) starting with the ground state of the undriven oscillator as the initial state [98]. We observe fast oscillations at short times. They decay, on the time scale  $\gamma^{-1}$  associated to the relaxation of the damped oscillator in a metastable state. Then, starting from a metastable state at intermediate times, a slow exponential decay towards the asymptotically globally stable state can be observed. During this process no oscillation is visible indicating that it can be associated with a relaxation transition rather than with the decay of a coherence.

The inverse timescale of this slow process is the quantum relaxation rate  $\Gamma$  for the nonlinear oscillator. It is determined by the smallest absolute value of the real part of the eigenvalues of the operator  $\mathcal{S}$  in Eq. (2.61). Results for the quantum relaxation rate  $\Gamma$  as function of the control parameter  $\omega_{\text{ex}}$  are shown in Fig. 2.14 b) for different damping constants  $\gamma$ .

In the monostable region (not shown in the figure), the relaxation rate  $\Gamma$  is close to  $\gamma$ , which is the relaxation rate of the monostable damped harmonic oscillator. In the bistable region, it decreases sharply, thereby defining a separation of time scales. Most importantly, it displays resonances at the same values of the frequencies where the avoided crossings of the quasienergy levels occur (see dashed vertical lines). This results are very similar to the corresponding results for a static double-

well potential [97]. This similarity is not surprising, having extensively analyzed in sections 2.5.2 and 2.6.2 the formal analogy between the two systems. In fact, the results can be qualitatively explained in terms of that analysis. The quasipotential defines two wells and the dissipation is characterized by intrawell transitions. For this reason the dissipation is much slower than in the monostable region or for the harmonic damped oscillator, characterized by the relaxation rate  $\gamma$ . Around the multiple avoided crossing this separation of time scales does not take place when the two wells are connected through resonant multiphoton transitions. For this reason, provided that the tunnelling is not destroyed by the system-bath interaction, peaks in the relaxation rate appear.

## 2.7 Conclusions and outlook

In this chapter, we have investigated the dynamics of the quantum Duffing oscillator. Starting from the solution of the coherent problem, we have subsequently included the influence of the environment by means of a Born-Markovian master equation. In particular, we have laid the focus on the deep quantum regime solving the problem for a broad range of parameter, by means of analytical as well as numerical approaches.

We have identified the double-well quasipotential governing the coherent dynamics. The dissipative dynamics is characterized by inter-well tunnelling transitions and intra-well bath-induced transitions. The complex interplay of tunnelling and dissipation gives rise to a rich phenomenology, which remained unaddressed in previous works. The two main features are:

- (i) The lineshape of the nonlinear response displays resonances as well as antiresonances corresponding to degenerate multi-photon transitions for the coherent system. These structures are visible as long as the coherent tunnelling is faster than the dissipative processes.
- (ii) The quantum relaxation rate  $\Gamma$  associated to the slowest relaxation process decreases below the linear relaxation rate  $\gamma$  in the bistable region, thereby defining a separation of time-scales. The effect might be reduced around the multiple avoided level crossings, if the oscillator can switch between the two wells via resonant multiphoton transitions. As a consequence the relaxation rate as a function of the driving frequency displays peaks, if the tunnelling is not suppressed by the coupling to the bath.

The formalism developed in this chapter could represent an effective tool to investigate more general problems. For instance the dynamics of a driven nonlinear oscillator parametrically coupled to a two level system, describing a SQUID coupled to a flux qubit by a mutual inductance. Another interesting generalization of the Duffing oscillator model is the bichromatically driven nonlinear oscillator. The investigation of its dissipative dynamics in the deep quantum regime will be the subject of a future publication. In Appendix C of this thesis, we preliminarily present the derivation of the corresponding master equation.

# 3 Nanoscale atomic waveguides with suspended carbon nanotubes

In this chapter we present the proposal of an experimentally viable set up for the realization of a one-dimensional (1D) ultracold atom gas in a nanoscale magnetic waveguide formed by a single doubly-clamped suspended carbon nanotubes (CNT).

The experimental techniques for manipulating alkali cold atom clouds via electromagnetic fields has been rapidly evolving throughout the past quarter of the century. This path led in 1995 to the realization of the first Bose-Einstein condensate in diluted gases [99] and more recently to the realization of 1D gases of bosons and fermions [32–34]. A comprehensive review on this topic goes beyond the scope of this work, we refer the interested reader to Refs. [15, 100, 101]. Nevertheless, an introductory section is devoted to the fundamental problem of the interaction between alkali atoms and the electromagnetic field. In passing, we sketch also the most important experimental applications.

## 3.1 Introduction: Alkali atoms in electromagnetic fields

As we shall detail below, the interaction of an atom with the electromagnetic field is specified by its ground-state configuration and its low-energy excitations. For this reason, we start by shortly reviewing the electronic structure of the alkali atoms.

The ground-state electronic structure of alkali atoms is simple: all electrons but one occupy closed shells and the remaining one is in an s-orbital in an higher shell. The only degree of freedom which is not fixed is the orientation of the valence electron spin. Therefore the doubly degenerate ground-state has the total spin  $S = 1/2$ , total orbital momentum  $L = 0$  and total angular momentum  $J = 1/2$  and is denoted in standard notation by  $^2S_{1/2}$ .

The lowest energy excitation consists in an intra-shell transition of the valence electron from the orbit with zero angular momentum to the orbit with one quantum unit of angular momentum ( $ns \rightarrow np$  transition). This process yields a doublet in the excitation spectrum due to spin-orbit interaction. The lowest (highest) energy level of the doublets  $^2P_{3/2}$  ( $^2P_{1/2}$ ) is fourfold (doubly) degenerate. The corresponding states are characterized by the electron spin being opposite to (aligned with) the orbital angular momentum.

In Table 3.1, we list the wavelengths associated to the  $nS_{1/2} \rightarrow nP_{3/2}$  transitions between the ground-state  $^2S_{1/2}$  and the lowest energy excited state  $^2P_{3/2}$ . They are relevant for experiments where atoms are trapped by means of laser light. In fact, when the wavelength associated to the laser field is close to the one associated to the  $nS_{1/2} \rightarrow nP_{3/2}$  transition, the atoms experience a strong field-dependent potential. We shall detail this effect in Section 3.1.1.

Isotope	$Z$	$I$	$\lambda_{sp}$ (nm)	$\Delta E_{hf}$ (MHz)
$^1\text{H}$	1	1/2	122	1420
$^6\text{Li}$	3	1	671	228
$^7\text{Li}$	3	3/2	671	804
$^{23}\text{Na}$	11	3/2	589	1772
$^{39}\text{K}$	19	3/2	767	462
$^{40}\text{K}$	19	4	767	-1286
$^{41}\text{K}$	19	3/2	767	254
$^{85}\text{Rb}$	37	5/2	780	3036
$^{87}\text{Rb}$	37	3/2	780	6835
$^{133}\text{Cs}$	55	7/2	852	9193

**Table 3.1:** Proton number  $Z$ , nuclear spin  $I$ , wave-length  $\lambda_{sp}$  of the  $nS_{1/2} \rightarrow nP_{3/2}$  transition and hyperfine splitting  $\Delta E_{hf}$  for the different alkali atoms

In many applications, e.g. in traps operating by means of not too strong magnetic fields or almost resonant laser light, the hyperfine splitting, due to the coupling between the electron angular momentum and the nuclear spin, becomes relevant. This interaction is given in terms of the operators for the nuclear spin  $\mathbf{I}$  and electronic angular momentum  $\mathbf{J}$  as

$$H_{hf} = A \mathbf{I} \cdot \mathbf{J} \quad (3.1)$$

where  $A$  is a constant which depends on the element considered. Since this Hamiltonian is invariant under rotation, it conserves the total angular momentum operator  $\mathbf{F} = \mathbf{I} + \mathbf{J}$ . A basis of eigenstates is given by the eigenvectors of  $F$  and  $F_z$ , denoted by  $|F, m_F\rangle$ . When the hyperfine interaction is taken into account, the ground-state level of the alkali atoms splits into a doublet. The two levels forming the doublets correspond to the total angular momentum  $F = I + 1/2$  (electronic spin aligned with the magnetic spin) and  $F = I - 1/2$  (electronic spin opposite to the magnetic spin), respectively. The hyperfine splitting is given by  $\Delta E_{hf} = (I + 1/2)A$ . The corresponding numerical values are listed in Table 3.1 for the different alkali atoms.

### 3.1.1 Zeeman interaction with an external magnetic field

When an alkali atom is in its electronic ground-state configuration, the only relevant coupling of the atom degrees of freedom to an external magnetic field is the one of the valence electron spin. However, many experiments with cold atoms are carried out in presence of an external field, whose interaction with the electron spin is of the same order or smaller than the hyperfine electron-nuclear spin coupling. In this regime, it is necessary to take the hyperfine interaction into account in order to investigate the dynamics of the electron spin.

We first consider uniform magnetic fields pointing in the  $z$  direction. The spin part of the Hamiltonian then reads

$$H_S = A \mathbf{I} \cdot \mathbf{S} + g_S \mu_B S_z B_z \quad (3.2)$$

with  $g_S \approx 2$  being the Landé factor for the electron spin and  $\mu_B$  the Bohr magneton. In the weak field limit, relevant for most experimental applications, the problem is formally equivalent to the Zeeman effect in presence of spin-orbit interaction. The hyperfine term is governing the dynamics and the coupling to the magnetic field is regarded as a small perturbation. The total angular momentum is thus still approximately conserved, and the states  $|F, m_F\rangle$  are approximate eigenstates. At first order in perturbation theory, the energy level splittings are given by

$$H_S = \frac{A}{2}[(F(F+1) - S(S+1) - I(I+1))] + g_F \mu_B m_F B_z, \quad (3.3)$$

with the Landé factor being

$$g_F = g_S \frac{F(F+1) + S(S+1) - I(I+1)}{2F(F+1)}. \quad (3.4)$$

Let us now consider the more general case of an atom moving in a space-dependent field. When the hyperfine splitting is much larger than the Zeeman splitting, we can consider  $F$  as a constant of motion, and drop the corresponding hyperfine term from the spin part of the Hamiltonian Eq. (3.3). Thus, if the field varies slowly with respect to the atomic lengthscale  $a_0 = 0.52\text{\AA}$ , the total Hamiltonian for an atom moving in a weak space-dependent magnetic field reads

$$H = \frac{\mathbf{P}^2}{2m} - \boldsymbol{\mu} \cdot \mathbf{B}(\mathbf{R}). \quad (3.5)$$

In the above equation  $\boldsymbol{\mu} = -g_F \mu_B \mathbf{F}$  is the atom magnetic moment, whereas  $\mathbf{R}$  and  $\mathbf{P}$  are the center-of-mass (COM) position and momentum operators, respectively. It is convenient to introduce the local rotation  $U(\mathbf{R})$ , which rotates the magnetic fields to be parallel to the  $z$  axis. The Hamiltonian in the rotated frame reads

$$H' = U^\dagger(\mathbf{R}) H U(\mathbf{R}) = \frac{\mathbf{P}^2}{2m} + \Delta T + g_F \mu_B F_z |\mathbf{B}(\mathbf{R})|. \quad (3.6)$$

The additional term  $\Delta T$  appears because the kinetic term is not invariant under a local rotation. When it is neglected, the eigenstates in the rotated frame are the states  $|F, m_F\rangle$ , whose spin follows adiabatically the direction of the field. We refer to this approximation as adiabatic approximation.

According to the sign of  $g_F m_F$  an atom is attracted to or repelled from regions of high field. The states corresponding to  $g_F m_F$  positive (negative) are referred to as *weak-field (strong-field) seeking states*. The term  $\Delta T$  causes non-adiabatic spin flip transitions from weak-field seeking to strong-field seeking states. This transition are often referred to as Majorana spin flips.

Since there cannot be a maximum of the magnetic field in free space [102], atoms in a strong-field seeking state can not be trapped by means of a purely magnetic confinement. Conversely, there are many alternative strategies for designing a minimum of the magnetic field by means of wire and bias fields, thereby trapping atoms in weak-field seeking states. One refers to such traps as *magnetic traps*. The most

simple configuration, the so-called *side-guide*, is illustrated below in the framework of our proposal for a nanowaveguide. For a comprehensive review on this subject see Ref. [15].

Let us mention in passing that the adiabatic approximation is not valid near a zero minimum of the magnetic field. Such a minimum constitutes an hole in the trap, since the rate of non-adiabatic spin flip transition diverges while it is approached. This problem can be circumvented in a number of ways, for instance, by applying laser radiation near the node of the field.

The spin flip transitions play an important role also in the framework of *evaporative cooling*. By selectively removing the most energetic atoms, the remaining one are cooled once the system thermalizes via elastic scattering. This can be effectively achieved in a magnetic trap by means of a radio frequency radiation, which induces spin flip transitions. Since the resonant frequency for these transitions is proportional to the intensity of the magnetic field, sweeping the frequency of the radiation above a certain threshold corresponds to removing the most energetic atoms, which can explore the external region of the potential.

### 3.1.2 Dynamical Stark interaction with a laser field

A second mechanism permitting confinement and cooling of neutral atoms is the dynamical Stark effect, which describes the interaction of the electric field with the dipole moment it induces on the atom.

Let us consider an atom immersed in a standing-wave

$$\mathbf{E}(\mathbf{x}, t) = E_0(\mathbf{x}) \operatorname{Re}[\boldsymbol{\varepsilon}(z) \exp(-i\omega_{\text{las}}t)], \quad (3.7)$$

obtained by two counterpropagating laser beams whose wave-length  $\lambda_{\text{las}} = 2\pi c/\omega_{\text{las}}$  is of the order of magnitude of the wave-length  $\lambda_{\text{sp}}$  associated to the  $nS_{1/2} \rightarrow nP_{3/2}$  transition (listed in Table 3.1). For definiteness, we assume that the beams propagate along the  $z$  axis. Since the electric field is uniform on the atomic length-scale  $a_0$ , we can apply the dipole approximation, yielding the interaction term

$$H_I(t) = -\mathbf{d} \cdot \mathbf{E}(\mathbf{R}, t) = -e \sum_i E_0(\mathbf{R}) \operatorname{Re}[\mathbf{r}_i \cdot \boldsymbol{\varepsilon}(Z) \exp(-i\omega_{\text{las}}t)]. \quad (3.8)$$

Here,  $\mathbf{d}$  is the dipole operator given in terms of the positions of the electrons relative to the atomic nucleus as  $\mathbf{d} = e \sum_i \mathbf{r}_i$ .

In the absence of an external field the mean value of the dipole operator vanishes, since the atomic states are approximately eigenstates of the parity operator (when the weak nuclear interaction is neglected). A weak electric field perturbs the orbit of the valence electron only. It is thus safe to disregard the interaction with the inner-shell electrons.

Moreover, it is reasonable to treat the coupling between the COM and the valence electron coordinates adiabatically by regarding the slow COM degrees of freedom as fixed, when the fast electron dynamics is considered. The latter is governed by the usual Hartree-Fock atomic Hamiltonian with an additional time periodic driving term associated to the dipole interaction in Eq. (3.8). The Floquet theorem assures

us that, for a fixed atom position  $\mathbf{R}$ , the electron dynamics is described in terms of a set of time-periodic Floquet states, see Section 2.3.1. These vectors change continuously, while the atom position  $\mathbf{R}$  changes, and coincide with the unperturbed atomic states in the region outside the laser field. One often refers to these Floquet states as dressed states. In the absence of any non-adiabatic transition, such as the absorption (emission) of a photon, the atoms remain in the dressed states, which coincide with the unperturbed ground-state outside the laser field. Since the unperturbed ground-state is doubly degenerate, but the interaction with the laser field splits the degeneracy, there are two relevant Floquet states. In the following, we refer to these states as the dressed ground-states or simply dressed states and denote them as  $|\phi_{\mathbf{R}}^{\pm}(t)\rangle$ , thereby pointing out that the atom position enters as a parameter. One can regard the meanvalue of the dipole interaction on this state and on the period  $T_{\omega} = 2\pi/\omega$ ,

$$V_{\pm}(\mathbf{R}) = \frac{1}{T_{\omega}} \int_0^{T_{\omega}} dt (\langle \phi_{\mathbf{R}}^{\pm}(t) | \otimes \langle \mathbf{R} |) H_I(t) (| \mathbf{R} \rangle \otimes | \phi_{\mathbf{R}}^{\pm}(t) \rangle), \quad (3.9)$$

as an effective potential experienced by the atoms moving in the laser field. The description of the atom dynamics in terms of this effective potential is often referred to as dressed atom picture, since the energy of interest is that of the atom with its accompanying perturbation produced by the radiation field.

In principle it would have been possible to evaluate the above defined dressed potential by means of a very simple leading order perturbative calculation, without introducing the Floquet solutions. In fact, this is the approach of standard textbooks [100]. However, motivated by the formal analogy to the problem considered in Chapter 2, it is worth to spend here some more efforts to comment on the driven dynamics of the valence electron.

In most applications, the detuning of the laser field  $\Delta \equiv \omega_{\text{las}} - 2\pi c/\lambda_{sp}$  is much smaller than the spin-orbit splitting but is still larger than the hyperfine splitting. In this limit, it is reasonable to introduce a *rotating-wave approximation* (RWA) similar to the one presented in Section 2.3.2. In this case, it consist in:

- (i) considering the six-dimensional Hilbert space  $\mathcal{H}_R$  composed of the doubly degenerate  $S_{1/2}$  and the fourfold degenerate  $P_{3/2}$  resonant levels,
- (ii) introducing a transformation that rotates the level  $P_{3/2}$  with frequency  $\omega_{\text{las}}$ ,
- (iii) dropping the oscillating terms, which describe transitions from the  $S_{1/2}$  ( $P_{3/2}$ ) to the  $P_{3/2}$  ( $S_{1/2}$ ) level accompanied by the emission (absorption) of one photon.

This procedure yields the  $6 \times 6$  time-independent RWA Hamiltonian matrix  $\tilde{H}$ . It is convenient to project the RWA Hamiltonian onto a basis of eigenstates of  $J$  and  $J_z$  for  $\mathcal{H}_R$ , which we denote as  $|j, m_j\rangle^1$ . Since the polarization  $\epsilon$  is orthogonal to the  $z$ -axis, a finite off-diagonal element of  $\tilde{H}$  is possible only for those states whose total angular momentum and its component along the  $z$ -axis differ by one. Hence in this basis, the RWA Hamiltonian has the block form  $\tilde{H} = \tilde{H}_+ \oplus \tilde{H}_-$ . The two blocks correspond to the three dimensional Hilbert spaces  $\mathcal{H}_{\pm} \equiv |1/2, \pm 1/2\rangle \oplus |3/2, \mp 1/2\rangle \oplus |3/2, \pm 3/2\rangle$ .

---

<sup>1</sup>We do not indicate explicitly the orbit occupied by the valence electron. It is understood that it is  $ns$  when  $j = 1/2$  and  $np$  when  $j = 3/2$ .

Let us first consider the special case of a circularly polarized electric field with positive sense about the  $z$ -axis ( $\boldsymbol{\varepsilon} = (\hat{e}_x + i\hat{e}_y)/\sqrt{2}$ ). The absorption of one photon is always accompanied with the excitation of the valence electron to a state with component of the angular momentum along the  $z$ -axis larger by one unit. Hence, the two blocks composing the RWA Hamiltonian have the simple form

$$\tilde{H}_+ = \begin{pmatrix} 0 & 0 & \Omega_{>}/2 \\ 0 & -\Delta & 0 \\ \Omega_{>}/2 & 0 & -\Delta \end{pmatrix}, \quad \tilde{H}_- = \begin{pmatrix} 0 & \Omega_{<}/2 & 0 \\ \Omega_{<}/2 & -\Delta & 0 \\ 0 & 0 & -\Delta \end{pmatrix}. \quad (3.10)$$

The corresponding quasienergy spectrum as a function of the detuning  $\Delta$  is shown schematically in Fig. 3.1. The straight line corresponds to the two non-interacting degenerate states  $|3/2, 3/2\rangle$  and  $|3/2, -1/2\rangle$ . The two one-photon avoided crossings, are due to the resonant interaction of the pairs  $|1/2, 1/2\rangle, |3/2, 3/2\rangle$  and  $|1/2, -1/2\rangle, |3/2, 1/2\rangle$ . The corresponding Rabi frequencies are given by

$$\begin{aligned} \Omega_{>} &= eE_0(\mathbf{R})|\langle 1/2, 1/2 | \mathbf{r} \cdot [\boldsymbol{\sigma}_+ \equiv (\hat{e}_x + i\hat{e}_y)/\sqrt{2}] | 3/2, 3/2 \rangle|, \\ \Omega_{<} &= eE_0(\mathbf{R})|\langle 1/2, -1/2 | \mathbf{r} \cdot [\boldsymbol{\sigma}_+ \equiv (\hat{e}_x + i\hat{e}_y)/\sqrt{2}] | 3/2, 1/2 \rangle|, \end{aligned} \quad (3.11)$$

respectively. The Rabi frequencies in the above equation depend on the field strength and on the atom species, whereas their ratio is fixed by the ratio of the relevant Clebsh-Gordon coefficients:  $\Omega_{>}/\Omega_{<} = 1/(1/\sqrt{3}) = \sqrt{3}$ . The dressed states  $|\phi_{\mathbf{R}}^{\pm}(t)\rangle$  (in the static frame) are given by

$$\begin{aligned} |\phi_{\mathbf{R}}^+(t)\rangle &= \cos \frac{\theta_{>}}{2} |1/2, 1/2\rangle - e^{-i\omega_{\text{las}} t} \sin \frac{\theta_{>}}{2} |3/2, 3/2\rangle \\ |\phi_{\mathbf{R}}^-(t)\rangle &= \cos \frac{\theta_{<}}{2} |1/2, -1/2\rangle - e^{-i\omega_{\text{las}} t} \sin \frac{\theta_{<}}{2} |3/2, 1/2\rangle \end{aligned} \quad (3.12)$$

with the angles  $\theta_{\gtrless}$  defined via  $\tan \theta_{\gtrless} = -\Omega_{\gtrless}/\Delta$ .

In presence of an arbitrary polarization, the dynamics is very similar. The spectrum is qualitatively the same: there are two avoided level crossings, and a degenerate non-interacting level. The dressed states becomes

$$|\phi_{\mathbf{R}}^{\pm}(t)\rangle = \cos \frac{\theta_{\pm}}{2} |g_{\pm}\rangle - e^{-i\omega_{\text{las}} t} \sin \frac{\theta_{\pm}}{2} |e_{\pm}\rangle, \quad (3.13)$$

with  $|g_{\pm}\rangle = |1/2, \pm 1/2\rangle$  and  $|e_{\pm}\rangle$  being a superposition of  $|3/2, \pm 3/2\rangle$  and  $|3/2, \mp 1/2\rangle$ . The angles  $\theta_{\pm}$  are defined via  $\tan \theta_{\pm} = -\Omega_{\pm}/\Delta$  in terms of the Rabi frequencies  $\Omega_{\pm} = eE_0(\mathbf{R})|\langle g_{\pm} | \mathbf{r} \cdot \boldsymbol{\varepsilon} | e_{\pm} \rangle|$ . The latter equation yields two Rabi frequencies, which fulfill  $\Omega_{<} \leq \Omega_{\pm} \leq \Omega_{>}$ . In presence of linear polarization the two avoided crossing are degenerate. The corresponding Rabi frequency is  $\Omega_{\pm} = \sqrt{2/3} \Omega_{>}$ .

By expanding Eq. (3.13) up to first order in  $\theta$  and plugging it into Eq. (3.9) we get

$$V(\mathbf{R})_{\pm} = -\frac{1}{2} \alpha_{\pm}(\omega_{\text{las}}) [E_0(\mathbf{R})]^2, \quad (3.14)$$



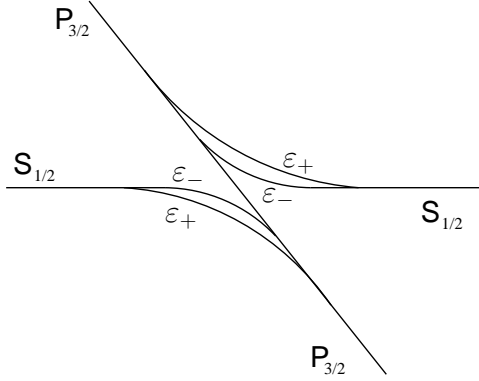


**Figure 3.1:** Schematic view of the crossing displayed by the  $S_{1/2}$  doublet and  $P_{3/2}$  quadruplet varying the detuning  $\Delta$  for a fixed non-linear polarization  $\epsilon$ . Away from resonance there are two degenerate levels. At resonance the doublet splits and each state form an avoided crossing with a state belonging to the quadruplet. The remaining two state composing the quadruplet do not mix with the doublet and define a straight line. We denote by  $\epsilon_+$  and  $\epsilon_-$ , the two levels which correspond to the degenerate unperturbed ground-state when the laser field perturbation is switched-off adiabatically.

with the dynamical polarizability

$$\alpha_{\pm}(\omega_{\text{las}}) \approx -\frac{e^2 |\langle e_{\pm} | \mathbf{r} \cdot \epsilon | g_{\pm} \rangle|^2}{\Delta}. \quad (3.15)$$

We can conclude that the dipole induced by an electric field aligns in the direction of (opposite to) the field if its frequency is below (above) the characteristic frequency  $\omega_{sp}$  associated with the relevant  $ns \rightarrow np$  transition. As a consequence, the atoms are attracted by (repelled from) regions of high field. One refers to laser fields whose frequencies are below (above)  $\omega_{sp}$  as red-detuned (blue-detuned) fields.

So far, we have implicitly assumed that the atomic excited states have an infinitely long life-time, thereby neglecting spontaneous emission. We can include phenomenologically a finite lifetime  $1/\Gamma_e$  of the  $np$  configuration for the valence electron by adding the imaginary part  $i\Gamma_e/2$ , to its energy. The dressed state describing the atom in the laser field is a dynamical superposition of a  $ns$  and a  $np$  state. Hence, by phenomenologically introducing a finite lifetime of the  $np$  configuration, one should expect non-adiabatic transitions from the dressed ground-state to an excited dressed state. In fact, the effective potential becomes complex. We formally write it as

$$V_{\pm} = V_{a\pm} + i\Gamma_{g\pm}/2. \quad (3.16)$$

We interpret its real part

$$V_{a\pm}(\mathbf{R}) = -\frac{1}{2}\alpha'_{\pm}(\omega_{\text{las}})[E_0(\mathbf{R})]^2, \quad (3.17)$$

with

$$\alpha'_{\pm}(\omega) \approx -\frac{\Delta e^2 |\langle e_{\pm} | \mathbf{r} \cdot \epsilon | g_{\pm} \rangle|^2}{\Delta^2 + (\Gamma_e/2)^2}, \quad (3.18)$$

as the potential experienced by the atom in the dressed ground-state while moving adiabatically in the field. On the other side,  $\Gamma_g$ , given by

$$\Gamma_{g\pm}(\mathbf{R}) = -\frac{1}{2}\alpha''_{\pm}(\omega_{\text{las}})[E_0(\mathbf{R})]^2, \quad (3.19)$$

with

$$\alpha''_{\pm}(\omega_{\text{las}}) \approx \frac{(\Gamma_e/2)e^2|\langle e_{\pm}|\mathbf{r} \cdot \boldsymbol{\varepsilon}|g_{\pm}\rangle|^2}{\Delta^2 + (\Gamma_e/2)^2}, \quad (3.20)$$

is the loss rate from the dressed ground-state, due to non-adiabatic transitions.

By using several laser beams, it is possible to design a variety of potentials. The building block is often a standing-wave created by two counter propagating beams. One can then superpose more than one standing-wave. Interference effects between different standing waves are avoided by either slight detuning of the two laser frequencies or by choosing two orthogonal polarizations. The resulting potentials are characterized by arrays or lattices of local minima. For example, by superposing two horizontal orthogonal standing-waves, one achieves a 2D lattice of 1D tubes. One refers to these ensembles of local minima as *optical traps*.

The emission of one photon with momentum  $q = c/\omega_{\text{las}}$  causes an energy variation of the order  $E_c = q^2/2m$ . This energy is called recoil energy and is associated with the minimal temperature which can be achieved when spontaneous emission is not negligible. In order to obtain a BEC or a degenerate 1D quantum-gas at the dilute densities characteristic of typical samples, one has to cool the atoms below the recoil energy. In the ultracold regime, it is thus very important to suppress spontaneous emission. This is achieved by confining the atoms in regions of low-field, thereby using blue-detuned laser beams. In order to further reduce  $\Gamma_g$ , it is advisable to detune them by at least 10%.

The non-adiabatic transition can be exploited to cool atoms moving in a laser field down to the recoil temperature. The most simple set up is based on two counterpropagating beams with orthogonal polarization. The resulting standing wave has a position dependent polarization. The resulting effective potentials  $V_{a\pm}$  have the form  $V_0[-2 \pm \sin(4\pi z/\lambda_{\text{las}})]$ . The maxima of  $V_{a+}$  (the potential experienced by an atom in the dressed state  $|\phi^+\rangle$ ) correspond to minima of  $V_{a-}$  (the potential experienced by an atom in the dressed state  $|\phi^-\rangle$ ) and vice versa.  $V_{a+}$  displays a minimum, when the laser light has  $\boldsymbol{\sigma}_+$  polarization. At the corresponding positions, the state  $|e_-\rangle \equiv |3/2, 1/2\rangle$  and  $|e_+\rangle \equiv |3/2, 3/2\rangle$  are resonantly populated. Spontaneous emission of a photon with longitudinal polarization (with respect to the  $z$  axis along which the two beams are propagating) causes a transition from  $|e_-\rangle$  to the unperturbed ground-states  $|g_+\rangle \equiv |1/2, 1/2\rangle$ . As a consequence a net population flow from the higher energy  $|\phi^-\rangle$  dressed state to the lower energy  $|\phi^+\rangle$  dressed state results. An analogous flow to the lower energy state takes place when  $V_{a-}$  displays a minimum and the light has  $\boldsymbol{\sigma}_-$  polarization. As a result the atoms continuously climb potential barriers and are thereby cooled. This cooling mechanism through non-adiabatic transition is known as *Sisyphus cooling*.

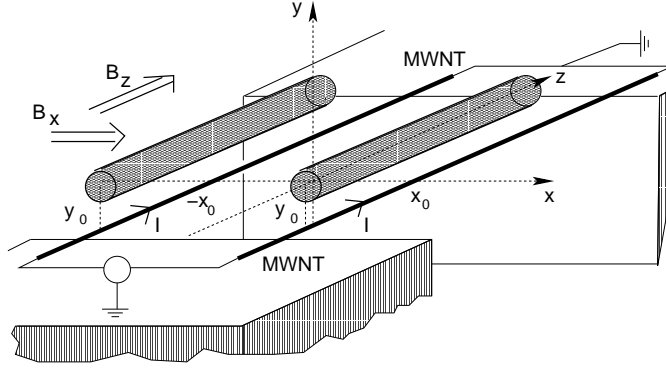


**Figure 3.2:** Sketch of the proposed device. A current-carrying suspended NT is positioned at  $(-x_0, 0, z)$  and together with the transverse magnetic field  $B_x$ , a 1D trapping potential is formed. The shaded region indicates the atom gas. A similar two-wire setup allows the creation of a bistable potential.

### 3.2 The setup for a nanowaveguide

In this section, we return to the main topic in the focus of this chapter: The proposal for a nanoscale magnetic waveguide to confine ultracold atoms to 1D. A typical proposed setup is sketched in Fig. 3.2. The setup employs a single suspended doubly-clamped NT (left NT in Fig. 3.2, the second suspended NT on the right will be used to create a double-well potential, see below), where nanofabrication techniques routinely allow for trenches with typical depths and lengths of several  $\mu\text{m}$  [22]. To minimize decoherence and loss effects [19], the substrate should be insulating apart from thin metal strips to electrically contact the NTs. Since strong currents (hundreds of  $\mu\text{A}$ ) are necessary, thick multiwall nanotubes (MWNTs) or ‘ropes’ [22] are best suited. The suspended geometry largely eliminates the influence of the substrate. A transverse magnetic field  $B_x$  is required to create a stable trap while a longitudinal magnetic field  $B_z$  suppresses Majorana spin flips [103, 104]. With this single-tube setup, neutral atoms in a weak-field seeking state can be trapped. Studying various sources for decoherence, heating or atom loss, and estimating the related time scales, we find that, for reasonable parameters, detrimental effects are small. As a concrete example, we shall consider  $^{87}\text{Rb}$  atoms in the weak-field seeking hyperfine state  $|F, m_F\rangle = |2, 2\rangle$ .

We next describe the setup in Fig. 3.2, where the (homogeneous) current  $I$  flows through the left NT positioned at  $(-x_0, 0, z)$ . With regard to the decoherence properties of the proposed trap, it is advantageous that the current flows homogeneously through the NT, as disorder effects are usually weak in NTs [22]. Neglecting boundary effects due to the finite tube length  $L$ , the magnetic field at  $\mathbf{x} = (x, y, z) = (\mathbf{x}_\perp, z)$  is given by

$$\mathbf{B}(\mathbf{x}) = \frac{\mu_0 I}{2\pi} \frac{1}{(x + x_0)^2 + y^2} \begin{pmatrix} -y \\ x + x_0 \\ 0 \end{pmatrix} + \begin{pmatrix} B_x \\ 0 \\ B_z \end{pmatrix} \quad (3.21)$$

with the vacuum permeability  $\mu_0$ . To create a trapping potential minimum,

let us write  $B_x = \mu_0 I / (2\pi y_0)$ . Then the transverse confinement potential is  $V(\mathbf{x}_\perp) = \mu |\mathbf{B}(\mathbf{x})|$ , where  $\mu = m_F g_F \mu_B$  with the Landé factor  $g_F$  and the Bohr magneton  $\mu_B$ . It has a minimum along the line  $(-x_0, y_0, z)$ , with the distance between the atom cloud and the wire being  $y_0$ . Under the adiabatic approximation,  $m_F$  is a constant of motion, and the potential is harmonic very close to the minimum of the trap, i.e.,  $V(\mathbf{x}) \simeq \mu B_z + \frac{1}{2} m \omega^2 [(x + x_0)^2 + (y - y_0)^2]$ , with frequency  $\omega = [\mu / (m B_z)]^{1/2} \mu_0 I / (2\pi y_0^2)$  and associated transverse confinement length  $l_0 = (\hbar / m \omega)^{1/2} \ll y_0$ , where  $m$  is the atom mass. The adiabatic approximation is valid as long as  $\omega \ll \omega_L$  with the Larmor frequency  $\omega_L = \mu B_z / \hbar$ . Non-adiabatic Majorana spin flips to a strong-field seeking state generate atom loss [15, 104] characterized by the rate  $\Gamma_{\text{loss}} \simeq (\pi \omega / 2) \exp(1 - 1/\chi)$ , with  $\chi = \hbar \omega / (\mu B_z)$  [103]. For convenience, we switch to a dimensionless form of the full potential  $V(\mathbf{x}_\perp)$  by measuring energies in units of  $\hbar \omega$  and lengths in units of  $l_0$ ,

$$\chi V = \left( 1 + \chi \frac{d^2 [(x + x_0)^2 - dy + y^2]^2 + d^4 (x + x_0)^2}{[(x + x_0)^2 + y^2]^2} \right)^{1/2}, \quad (3.22)$$

which depends only on  $d = y_0 / l_0$  and  $\chi$ . The trap frequency then follows as

$$\omega = \frac{m \chi \mu^2}{\hbar^3} \left( \frac{\mu_0 I}{2\pi d^2} \right)^2. \quad (3.23)$$

Note that a real trap also requires a longitudinal confining potential with frequency  $\omega_z \ll \omega$ .

To obtain an estimate for the design of the nanotrap, we choose realistic parameters:  $\chi = 0.067$ , corresponding to a rate of spin flip transition per oscillation period  $\Gamma_{\text{loss}} / \omega \sim 10^{-6}$ . Decreasing  $d$  increases the trap frequency. However,  $d$  cannot be chosen too small, for otherwise the potential is not confining anymore (and the harmonic approximation becomes invalid). Using  $V(\infty) = \chi^{-1} (1 + \chi d^2)^{1/2}$  for the potential at  $|\mathbf{x}_\perp| \rightarrow \infty$ , we now show that for  $d \sim 5$ , the harmonic approximation breaks down. To see this, note that for  $d = 10$ , the potential provides a confining barrier (in units of the trap frequency  $\omega$ ) of  $V(\infty) - V(0, 0, z) = 23.8$ , while for  $d = 5$ , we get only  $V(\infty) - V(0, 0, z) = 9.8$ . Thus exceedingly small values of  $d$  would lead to unwanted thermal atom escape processes out of the trap. To illustrate the feasibility of the proposed trap design, we show in Table 3.2 several parameter combinations with realistic values for the MWNT current together with the resulting trap parameters. In practice, first the maximum possible current should be applied to the NT, with some initial field  $B_x$ . After loading of the trap, the field  $B_x$  should be increased, the cloud thereby approaching the wire with a steepening of the confinement. At the same time,  $y_0$  and consequently  $d$  decrease. This procedure can be used to load the nanotrap from a larger magnetic trap (ensuring mode matching). For a given current, there is a corresponding lower limit  $y_{\text{min}}$  for stable values of  $y_0$  from the requirement  $d < 5$ , as already mentioned above. To give an example, the confining potential is shown in Fig. 3.3a) for  $I = 100 \mu\text{A}$ , representing a reasonable current through thick NTs [22],  $d = 10$ ,  $x_0 = l_0$  and  $\Gamma_{\text{loss}} / \omega = 10^{-6}$  (where  $\chi = 0.067$ ). The resulting trap frequency is  $\omega = 2\pi \times 4.6 \text{ kHz}$  and the associated transverse magnetic field is  $B_x = 0.14 \text{ G}$ .

$I(\mu\text{A})$	$d$	$\omega(\text{kHz})$	$y_0(\text{nm})$	$l_0(\text{nm})$
1000	10	$2\pi \times 460$	144	14
250	5	$2\pi \times 460$	72	14
250	10	$2\pi \times 28.7$	576	58
100	5	$2\pi \times 73.8$	180	36
100	10	$2\pi \times 4.6$	1440	144
50	5	$2\pi \times 18.4$	360	72
25	5	$2\pi \times 4.6$	720	144

**Table 3.2:** Trap frequencies  $\omega$ , distances  $y_0$  of the atomic cloud from the NT wire, and oscillator lengths  $l_0$  for  $\chi = 0.067$  and various  $I, d$ .

### 3.3 Influence of destructive effects

For stable operation, it is essential that destructive effects like atom loss, heating or decoherence are small.

(i) One loss process is generated by non-adiabatic Majorana spin flips as discussed above. It is sufficiently suppressed by the choice  $\chi = 0.0067$  yielding  $\Gamma_{\text{loss}}/\omega \sim 10^{-6}$ .

(ii) Atom loss may also originate from noise-induced spin flips, where current fluctuations cause a fluctuating magnetic field generating the Majorana spin flip rate [18]

$$\gamma_{\text{sf}} \simeq \left( \frac{\mu_0 \mu}{2\pi \hbar y_0} \right)^2 \frac{S_I(\omega_L)}{2}, \quad S_I(\omega) = \int dt e^{-i\omega t} \langle I(t)I(0) \rangle. \quad (3.24)$$

At room temperature and for typical voltages  $V_0 \approx 1$  V, we have  $\hbar\omega_L \ll k_B T \ll eV_0$ , and  $S_I(\omega_L)$  is expected to equal the shot noise  $2eI/3$  of a diffusive wire. For the parameters above, a rather small escape rate results,  $\gamma_{\text{sf}} \approx 0.051$  Hz. If a (proximity-induced) supercurrent is applied to the MWNT, the resulting current fluctuations could be reduced even further.

(iii) Thermal NT vibrations might create decoherence and heating, and could even cause a transition to the first excited state of the trap. Using a standard elasticity model for a doubly clamped wire in the limit of small deflections, the maximum mean square displacement is [105]

$$\sigma^2 = \langle \phi^2(L/2) \rangle = \frac{k_B T L^3}{192 Y M_I}, \quad (3.25)$$

where  $\phi(z)$  is the NT transverse displacement,  $L$  the (suspended) NT length,  $T$  the temperature,  $Y$  the Young modulus, and  $M_I$  the NT's moment of inertia. For  $L = 10\mu\text{m}$  and typical material parameters from Ref. [22], we find  $\sigma \approx 0.2$  nm at room temperature. This is much smaller than the transverse size  $l_0$  of the atomic cloud. Small fluctuations of the trap center could cause transitions to excited transverse trap states. Detailed analysis shows that the related decoherence rate is also negligible, since the transverse fundamental vibration mode of the NT has the fre-

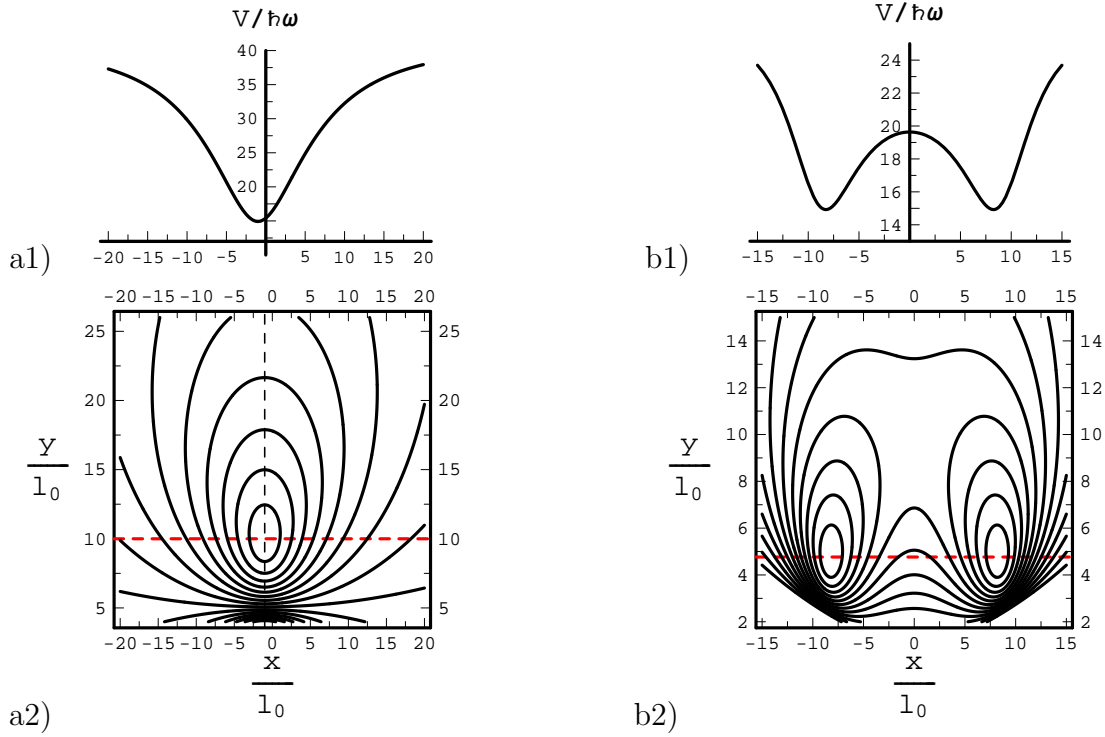


**Figure 3.3:** (a) Transverse trapping potential of the nanoscale waveguide for  $I = 100 \mu\text{A}$ ,  $d = 10$ ,  $\chi = 0.067$  and  $x_0 = l_0$ . The resulting trap frequency is  $\omega = 2\pi \times 4.6$  kHz while  $y_0 = 1440$  nm, corresponding to  $B_x = 0.14$  G. (a1) shows a cut along  $y = y_{\min}$  through the contour plot shown in (a2), see horizontal dashed line. (b) Bistable potential for the double-wire configuration for  $\chi = 0.067$ ,  $I = 100 \mu\text{A}$ ,  $x_0 = 200$  nm and  $y_0 = 100$  nm. (b1) displays a cut along  $y = y_{\min}$  through the contour shown in (b2), see dashed line.

quency

$$\omega_f = \frac{\beta_1^2}{L^2} \sqrt{\frac{Y M_I}{\rho_L A_c}}, \quad (3.26)$$

with  $\beta_1 \simeq 4.73$ , the mass density  $\rho_L$ , and the cross-sectional area  $A_c$ . For the above parameters,  $\omega_f = 2\pi \times 11.9$  MHz is much larger than the trap frequency itself. Due to the strong frequency mismatch, the coupling of the atom gas to the NT vibrations is therefore negligible.

(iv) Another decoherence mechanism comes from current fluctuations in the NTs. Following the analysis of Ref. [20], the corresponding decoherence rate is

$$\frac{\gamma_c}{\omega} = \frac{3\pi}{4\hbar} k_B T \frac{\sigma_0 A}{y_0^3} \left( \frac{\mu_0 \mu_B}{2\pi} \right)^2 \frac{\chi}{\hbar\omega}, \quad (3.27)$$

where  $\sigma_0$  is the NT conductivity and  $A$  the cross-sectional area through which the current runs in the NT. For the corresponding parameters we find  $\gamma_c/\omega < 10^{-8}$ .

(v) Another potential source of atom loss could be the attractive Casimir-Polder force between the atoms and the NT surface. The Casimir-Polder interaction poten-

tial between an infinite plane and a neutral atom is given by  $V_{\text{CP}} = -C_4/r^4$  [19, 106]. For a metallic surface and  $^{87}\text{Rb}$  atoms,  $C_4 = 1.8 \times 10^{-55} \text{ Jm}^4$ , implying that at a distance of  $1 \mu\text{m}$  from the surface, the characteristic frequency associated with the Casimir-Polder interaction is  $V_{\text{CP}}/\hbar = 2\pi \times 0.29 \text{ kHz}$ . This represents a fundamental decoherence limit in the kHz regime for conventional on-chip traps with typical current-carrying wire widths  $\approx 10 \mu\text{m}$ . Instead, for our particular design in the nanometer scale, the surface of a NT with a diameter of a few nm covers only a small portion of an infinite plane for distances above 100 nm. Hence, the impact of the Casimir-Polder interaction should be strongly reduced in our setup. A more detailed estimate, however, goes beyond the scope of this work.

(vi) A further possible mechanism modifying the shape of the confining potential is the influence of the electric field  $E$  between the two contacts of the nanowire and the macroscopic leads which is created by the transport voltage  $V$ . This field depends strongly on the detailed geometry of the contacts. However, the electric field can in general be reduced if the total length  $L_{\text{tot}}$  of the NT is increased. (Note that  $L_{\text{tot}}$  can be different from the length  $L$  over which the NT is suspended). Due to the small intrinsic NT resistivity, the influence of the contact resistance then decreases for longer NTs.

### 3.4 Number of trapped atoms and size of atom cloud

Next we address the important issue of how many atoms can be loaded in such a nanotrap. This question strongly depends on the underlying many-body physics which determines for instance the density profile of the atom cloud. Since the trap frequencies given in Table 3.2 exceed typical thermal energies of the cloud, we will consider the 1D situation. Within the framework of two-particle s-wave scattering in a parabolic trap, the effective 1D interaction strength  $g_{1\text{D}} = -2\hbar^2/(ma_{1\text{D}})$  is related to the 3D scattering length  $a$  according to [28]

$$a_{1\text{D}} = -\frac{l_0^2}{a} \left( 1 - \mathcal{C} \frac{a}{\sqrt{2}l_0} \right), \quad (3.28)$$

where  $\mathcal{C} \simeq 1.4603$ . Interestingly,  $g_{1\text{D}}$  shows a confinement-induced resonance (CIR) for  $a = \sqrt{2}l_0/\mathcal{C}$  [28]. For nearly parabolic traps respecting parity symmetry, this CIR is split into three resonances as will be detailed in Chapter 4. However, for the typical trap frequencies displayed in Table 3.2, corresponding to non-resonant atom-atom scattering, the parabolic confinement represents a very good approximation. For free bosons in 1D, the full many-body problem can be solved analytically [107]. It turns out that the governing parameter is given by  $n|a_{1\text{D}}|$ , where  $n$  is the atom density in the cloud. For weak interactions (large  $n|a_{1\text{D}}|$ ), a Thomas-Fermi (TF) gas results, while in the opposite regime, the Tonks-Girardeau (TG) gas is obtained.

For realistic traps with an additional longitudinal confining potential with frequency  $\omega_z \ll \omega$ , the problem has been addressed in Ref. [108]. The corresponding governing parameter is  $\eta = n_{\text{TF}}|a_{1\text{D}}|$  where  $n_{\text{TF}} = [(9/64)N^2(m\omega_z/\hbar)^2|a_{1\text{D}}|]^{1/3}$  is the

$\omega(\text{kHz})$	$a_{1D}(\text{nm})$	$N$	$\eta$	$\ell(\mu\text{m})$
$2\pi \times 460$	-26.65	30	0.11	7.7
$2\pi \times 460$	-26.65	50	0.15	10
$2\pi \times 73.8$	-223	30	0.67	7.3
$2\pi \times 73.8$	-223	50	0.94	8.7
$2\pi \times 73.8$	-223	100	1.49	11
$2\pi \times 28.76$	-603	30	2.55	5.3
$2\pi \times 28.76$	-603	50	3.58	6.3
$2\pi \times 28.76$	-603	100	5.72	7.9

**Table 3.3:** Typical results for the longitudinal size  $\ell$  of the  $^{87}\text{Rb}$  cloud for realistic values of the transversal trap frequency  $\omega$  and the atom number  $N$ , where  $\omega_z = 2\pi \times 0.1$  kHz. For  $\eta$ , see text.

cloud density in the center of the trap in the TF approximation. Small  $\eta$  characterizes a TG gas whereas large  $\eta$  corresponds to the TF gas. The longitudinal size  $\ell$  of the atom cloud in terms of the atom number  $N$  and the longitudinal (transversal) trap frequencies  $\omega_z$  ( $\omega$ ) has been computed in Ref. [108], with the result

$$\ell = \left[ \frac{3N(\hbar/m\omega_z)^2}{|a_{1D}|} \right]^{1/3} \quad (3.29)$$

in the TF regime and

$$\ell = [2N(\hbar/m\omega_z)]^{1/2} \quad (3.30)$$

in the TG regime. In order to determine the cloud size  $\ell$ , we first calculate  $\eta$  for fixed  $N, \omega_z$  and  $\omega$ , and then use the respective formula, Eq. (3.29) or (3.30). In the crossover region, both expressions yield similar results that also match the full numerical solution [108]. Typical results for realistic parameters are listed in Table 3.3 for  $\omega_z = 2\pi \times 0.1$  kHz. From these results, we conclude that the length of the suspended NT should be in the  $\mu\text{m}$ -regime in order to trap a few tens of  $^{87}\text{Rb}$  atoms.

To summarize the discussion of the monostable trap, we emphasize that the proposed nanotrap is realistic, with currents of a few 100  $\mu\text{A}$  and lengths of few  $\mu\text{m}$  of the suspended parts of NT. No serious decoherence, heating or loss mechanisms are expected for reasonable parameters of this nanotrap.

### 3.5 Double-well potential with two carbon nanotubes

In order to illustrate the advantages of the miniaturization to the nanoscale, let us consider a setup which allows two stable minima separated by a tunnelling barrier. The simplest setup consists of two parallel NTs carrying co-propagating currents  $I$ , a (small) longitudinal bias field  $B_z$  and a transverse bias field  $B_x$ . Such a double-well



potential for 1D ultracold atom gases would permit a rich variety of possible applications. Experiments to study Macroscopic Quantum Tunnelling and Macroscopic Quantum Coherence phenomena [63] between strongly correlated 1D quantum gases could then be performed. In addition, qubits forming the building blocks for a quantum information processor could be realized. The rich tunability of the potential shape, including tuning the height of the potential barrier as well as the tunnelling distance, is a particularly promising feature.

To realize this potential, we propose to place a second current-carrying NT at  $(+x_0, 0, z)$ , where the condition  $x_0 > y_0$  guarantees the existence of two minima located at  $y_0(\pm\sqrt{x_0^2/y_0^2 - 1}, 1)$ . By tuning the transversal magnetic field  $B_x$  and the current  $I$ ,  $y_0$  and thus the location of the minima can be modified. Around these minima, the potential is parabolic with frequency

$$\omega = \left[ \frac{\mu^2 \chi}{m \hbar} \left( \frac{\mu_0 I}{2\pi} \right)^2 \frac{1}{y_0^2} \left( \frac{1}{y_0^2} - \frac{1}{x_0^2} \right) \right]^{1/3}. \quad (3.31)$$

Similar to the considerations above, we obtain the potential in units of  $\hbar\omega$ , which depends only on  $d_x = x_0/l_0$ ,  $d_y = y_0/l_0$  and  $\chi$ ,

$$\begin{aligned} \chi V = & \left( 1 + \frac{\chi d_y^4}{1 - d_y^2/d_x^2} \left\{ \left[ \frac{-y}{(x + d_x)^2 + y^2} + \frac{-y}{(x - d_x)^2 + y^2} + \frac{1}{d_y} \right]^2 \right. \right. \\ & \left. \left. + \left[ \frac{x + d_x}{(x + d_x)^2 + y^2} + \frac{x - d_x}{(x - d_x)^2 + y^2} \right]^2 \right\} \right)^{1/2}. \end{aligned} \quad (3.32)$$

Figure 3.3 b) shows the corresponding bistable potential for the particular case of  $\chi = 0.067$ ,  $I = 200 \mu\text{A}$ ,  $y_0 = 100 \text{ nm}$  and  $x_0 = 200 \text{ nm}$ . The two minima are clearly discerned. To see how the frequency in the single well develops if the current in the second wire is turned on, we introduce the reference frequency  $\omega_0$  in the single-well case with a fixed current  $I$  and a fixed transverse field  $B_x$ , such that  $y_0 = x_0/2$ . Then we obtain the ratio

$$\frac{\omega}{\omega_0} = \left[ \frac{1}{16} \left( \frac{x_0}{y_0} \right)^4 \left( 1 - \frac{y_0^2}{x_0^2} \right) \right]^{1/3}. \quad (3.33)$$

For decreasing  $B_x$  and keeping  $I$  constant, we find that  $\omega$  decreases as shown in Fig. 3.4 (black solid line and left scale), while the distance  $y_0$  of the atom cloud increases. In the limit  $x_0 = y_0$ , the two minima merge and the potential becomes quartic and monostable, implying that  $\omega \rightarrow 0$ . For the above parameter set, we find  $\omega_0 = 2\pi \times 291 \text{ kHz}$ . Since one could obtain the same  $\omega_0$  for a larger current  $I$  and a correspondingly larger distance  $x_0$ , one gets the same trap frequency for a fixed ratio of  $y_0/x_0$ . However,  $d_x$  and  $d_y$  themselves would change and since the parabolic frequency  $\omega$  is fixed, only the non-linear corrections to the parabolic potential will be modified. This in turn influences the height of the potential barrier and the

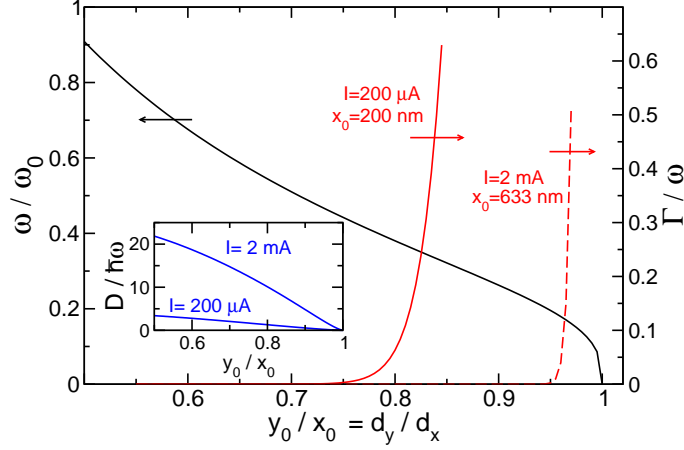


**Figure 3.4:** Trap frequency  $\omega$  in the bistable potential (left scale) and tunnelling rate  $\Gamma$  within the WKB-approximation (right scale) as a function of the ratio  $y_0/x_0 = d_y/d_x$ . For the definition of  $\omega_0$ , see text. The tunnelling rate  $\Gamma$  is computed for  $^{87}\text{Rb}$  atoms with  $\chi = 0.067$  and  $x_0 = 200$  nm for two values of the current  $I$  given in the figure.

tunnelling rate between the two wells. Next we study the influence of the length scale  $x_0$  on these two quantities.

Taking the full potential into account, we calculate the barrier height and the tunnelling rate in WKB approximation. The barrier height  $D$  separating the two stable wells,

$$\frac{D}{\hbar\omega} = \chi^{-1} \left( 1 + \chi d_y^2 \frac{1 - d_y/d_x}{1 + d_y/d_x} \right)^{1/2} - \chi^{-1}, \quad (3.34)$$

is shown as a function of  $y_0/x_0$  for two values of  $I$  in the inset of Fig. 3.4. Note that the barrier height is of the order of a few multiples of the energy gap in the wells, implying that the potential is in the deep quantum regime, favoring quantum-mechanical tunnelling between the two wells. The corresponding tunnelling rate  $\Gamma$  for the lowest-lying pair of energy eigenstates follows in WKB approximation as

$$\frac{\Gamma}{\omega} = e^{-\int_{x_a}^{x_b} dx \sqrt{2[V(x, d_y) - 1]}}, \quad (3.35)$$

where  $x_{a/b}$  are the (dimensionless) classical turning points in the inverted potential at energy  $E = \hbar\omega$ , which is approximately the ground-state energy of a single well. The integral in Eq. (3.35) is calculated along the line connecting the two minima corresponding to  $y = y_0$ . Results for  $\Gamma$  are shown in Fig. 3.4 (red solid lines and right scale) as a function of  $y_0/x_0$  for two different values of the current  $I$  and the distance  $x_0$  yielding the same  $\omega_0$ . Note that for the smaller current,  $I = 200 \mu\text{A}$ ,  $\Gamma$  assumes large values already for large frequencies  $\omega$ . This also implies that the detrimental effects discussed above are less efficient. On the other hand, for large currents, the

tunnelling regime is entered only for much smaller trap frequencies. For the above parameters, we find  $\omega_0 = 2\pi \times 291$  kHz. For the smaller current, the tunnelling regime starts at frequencies of around  $\omega = 0.37\omega_0 = 2\pi \times 108$  kHz, corresponding to a temperature of  $T = 32$   $\mu$ K, while for the larger current, the tunnelling regime is entered at  $\omega = 0.18\omega_0 = 2\pi \times 52$  kHz corresponding to  $T = 16$   $\mu$ K.

A potential drawback of the double wire configuration could be the transverse NT deflection due to their mutual magnetic repulsion. For an estimate, note that the NT displacement field  $\phi(z, t)$  obeys the equation of motion  $\rho_L \ddot{\phi} = -Y M_I \phi'''' + \mu_0 I^2 / (4\pi x_0)$ . The static solution under the boundary conditions  $\phi(0, L) = \phi'(0, L) = 0$  is  $\phi(z) = \mu_0 [Iz(z - L)]^2 / (96\pi Y M_I x_0)$ . Using again parameters from Ref. [22], we find the maximum displacement  $\phi(L/2) \approx 0.03$  nm for  $L = 10\mu$ m. Hence the mutual magnetic repulsion of the NTs is very weak. Finally, we note that a potential misalignment of the two NT wires is no serious impediment for the design. Experimentally available techniques could be combined which allow on one hand to move a NT on a substrate by an atomic force microscope [109], while on the other hand, the NTs can be suspended and contacted after being positioned [110].

### 3.6 Conclusions

To conclude, we propose a nanoscale waveguide for ultracold atoms based on doubly clamped suspended nanotubes. All common sources of imperfection can be made sufficiently small to enable stable operation of the setup. Two suspended NTs can be combined to create a bistable potential in the deep quantum regime. When compared to conventional atom-chip traps employed in present experiments, such nanotraps offer several new and exciting perspectives that hopefully motivate experimentalists to realize this proposal.

First, higher trap frequencies can be achieved while at the same time using smaller wire currents. This becomes possible here because both the spatial size of the atom cloud and its distance to the current-carrying wire(s) would be reduced to the nanometer scale, and because NTs allow typical current densities of  $10\mu$ A/nm<sup>2</sup>, which should be compared to the corresponding densities of  $10$  nA/nm<sup>2</sup> in noble metals. For the case of a single-well trap, the resulting trap frequencies go beyond standard chip traps [15]. Large trap frequencies at low currents are generally desirable, since detrimental effects like decoherence, Majorana spin flips, or atom loss will then be significantly reduced.

Second, regarding our proposal of a bistable potential with strong tunnelling, the miniaturization towards the nanoscale represents a novel opportunity to study coherent and incoherent tunnelling of a macroscopic number of cold atoms. The proposed bistable nanotrap is characterized by considerably reduced tunnelling distances, thus allowing for large tunnelling rates at large trap frequencies. Note that the energy scale associated with tunnelling is larger than thermal energies for realistic temperatures. Such a bistable device could then switch between the two stable states on very short time scales. Within our proposal the parameters of the bistable

potential can be tuned over a wide range by modifying experimentally accessible quantities like the current or magnetic fields.

A third advantage of this proposal results from the homogeneity of the currents flowing through the NTs. As NTs are characterized by long mean free paths, they often constitute (quasi-)ballistic conductors, where extremely large yet homogeneous current densities are possible. This distinguishes NTs from the conventionally used wires and could allow to overcome the fragmentation problem [15]. Fragmentation of the atom cloud is presently one of the main impediments to progress in the field of atom-chip traps.

Detection certainly constitutes an experimental challenge in this truly 1D limit. However, we note that single-atom detection schemes are currently being developed, which would also allow to probe the tight 1D cloud here, e.g., by combining cavity quantum electrodynamics with chip technology [16], or by using additional perpendicular wires/tubes ‘partitioning’ the atom cloud [111]. This may then allow to study interesting many-body physics in 1D in an unprecedented manner.

# 4 Confinement-induced resonances in arbitrary quasi-one-dimensional traps

In the previous section, we illustrated the proposal for a nanodevice, which would allow the manipulation of a 1D degenerate quantum gas of alkali atoms. In order to reach the quantum regime, it is necessary to cool the atoms in the cloud down to the nano-Kelvin regime, below the temperature associated to the recoil energy. The only means to achieve such low temperature is the evaporative cooling method. This technique requires a large ratio of two-body elastic scattering, which permits the thermalization between two subsequent rf sweeps, over three-body inelastic events, which cause loss of atoms and recombination into molecules (at such low temperatures the stable phase is the solid phase). For this reason, the ultracold cloud are usually extremely diluted with average inter-particle distances being an order of magnitude larger than the Van der Waals particle-particle interaction.

In this regime, the low-energy two-body scattering dominates the dynamics. The cloud can be modeled as an ensemble of 1D particles interacting via a two-body zero-range potential. The strength of the potential is determined by the solution of the two-body problem in presence of a tight transversal confinement.

In the focus of this chapter is the latter problem. We develop a formalism to solve it in the most general case of a two-component ultracold atom gas experiencing an arbitrary transverse confining potential. The key feature is that, except for the special case of a one-component gas in a parabolic trap, the COM and the relative degrees of freedom do not decouple. For this reason, the problem is much more involved than a normal scattering problem. Nevertheless, it is possible to formally derive the bound state and the low-energy scattering solutions. In particular, it is shown that for certain values of the *s-wave scattering length* a confinement-induced-resonance (CIR) of the 1D interaction strength results. These resonances are formally analogous to the well-known Feshbach resonances. In order to evaluate their locations for experimentally relevant cases, it is necessary to rely on partially numerical treatments.

The chapter is organized as follows: The introductory Section 4.1 is devoted to the scattering in free space. In Sec. 4.2, we develop the formalism to address the scattering in a confined geometry. Section 4.3 presents the bound-state solution, while Sec. 4.4 contains the analysis for the scattering solutions, including the analogy to Feshbach resonances. In Sec. 4.5 we discuss the special case of harmonic confinement, and in Sec. 4.6 a particular example of a non-parabolic confinement is illustrated. Finally, we conclude in Sec. 4.7. Technical details have been delegated to Appendix E. We set  $\hbar = 1$  throughout this part again.

## 4.1 Introduction: Scattering in free space

Before considering the main subject in the focus of this chapter, i.e. the scattering of two particles experiencing a tight transversal confinement, we give a short overview to the theory of quantum elastic scattering in free space. In particular, we will concentrate on the low-energy *s-wave* scattering relevant for ultracold atom collisions.

We first consider the more general problem of two particle *elastic scattering*, i.e., energy-conserving processes that do not alter the internal state of the particles, and we will assume that two distinguishable particles interact through a central potential  $U(r)$ . This problem is equivalent to the scattering of a single particle of reduced mass  $\mu = m_1 m_2 / (m_1 + m_2)$  by a static potential, since the center-of-mass (COM) degrees of freedom are decoupled from the relative ones. For an extensive review on this topic, see standard quantum mechanics text-books, for example [113].

The wave function for the relative coordinate in a state of definite energy  $E = k^2/2\mu$  is the sum of an incoming plane wave and an outgoing scattered wave:

$$\psi(\mathbf{r}) = e^{i\mathbf{k}\cdot\mathbf{r}} + \psi_{\text{sc}}(\mathbf{r}). \quad (4.1)$$

The plane wave is normalized so that the current density is equal to the plane wave velocity  $\mathbf{v} = \mathbf{k}/m$ . At large distances the outgoing scattered wave becomes spherical, and the wave function assumes the asymptotic form

$$\psi(\mathbf{r}) \simeq e^{i\mathbf{k}\cdot\mathbf{r}} + f_e(k, \theta, \varphi) \frac{e^{ikr}}{r}. \quad (4.2)$$

Due to the spherical symmetry of the potential, the solution has rotational symmetry with respect to the direction of the incident plane wave (which we take to be the  $z$  direction) and the scattering amplitude  $f_e$  depends only on the angle  $\theta$  between the incoming and the outgoing relative momenta and on the energy of the incoming wave. The latter property allows to expand the wave function for the relative motion on the basis of Legendre polynomials  $P_l(\cos \theta)$ ,

$$\psi(\mathbf{r}) = \sum_{l=0}^{\infty} A_l P_l(\cos \theta) R_l(r). \quad (4.3)$$

The radial wave functions  $R_l(r)$  satisfy the equation

$$R_l''(r) + \frac{2}{r} R_l'(r) + \left[ k^2 - \frac{l(l+1)}{r^2} - 2\mu U(r) \right] R_l(r) = 0, \quad (4.4)$$

and at large interparticle separations, where we can neglect both the centrifugal barrier and the potential, they have the asymptotic form

$$R_l(r) \simeq \frac{1}{kr} \sin \left( kr - \frac{\pi}{2} l + \delta_l \right) \quad (4.5)$$

expressed for each angular momentum component in terms of an appropriate phase shift  $\delta_l$ . The coefficients  $A_l$  are fixed by comparing Eq. (4.3) with Eq. (4.2). Using the asymptotic expansion for a plane wave (valid at large distances)

$$e^{ikz} \simeq \frac{1}{kr} \sum_{l=0}^{\infty} i^l (2l+1) P_l(\cos \theta) \sin \left( kr - \frac{\pi}{2} l \right) \quad (4.6)$$

and imposing that the solution contains only outgoing spherical components, one finds

$$A_l = i^l (2l+1) e^{i\delta_l} \quad (4.7)$$

and

$$f_e(k, \theta) = \sum_{l=0}^{\infty} (2l+1) f_l(k) P_l(\cos \theta), \quad (4.8)$$

$f_l(k)$  is defined as

$$f_l(k) \equiv \frac{1}{k \cot \delta_l - ik}. \quad (4.9)$$

The probability per unit time that the scattered particle will pass through a surface element  $dS = r^2 d\Omega$  is  $\mathbf{v} dS |f_e|^2 / r^2$ , and its ratio to the current density in the incoming wave and to the solid angle  $d\Omega$  is the *differential cross section*

$$\frac{d\sigma}{d\Omega} = |f_e(k, \theta)|^2. \quad (4.10)$$

The total scattering cross-section is obtained by integrating the former expression over the whole solid angle:

$$\sigma = 2\pi \int_{-1}^{+1} d(\cos \theta) |f_e(k, \theta)|^2. \quad (4.11)$$

Using the explicit expression (4.8) for the scattering amplitude and the orthogonality relation for the Legendre polynomials,

$$\int_{-1}^{+1} d(\cos \theta) P_m(\cos \theta) P_n(\cos \theta) = \frac{2}{2m+1} \quad \text{if } m = n, \quad 0 \text{ otherwise}, \quad (4.12)$$

the total scattering cross-section can be expressed in terms of the phase shifts as

$$\sigma = \frac{4\pi}{k^2} \sum_{l=0}^{\infty} (2l+1) \sin^2 \delta_l. \quad (4.13)$$

In the case of indistinguishable boson (fermion), we have to consider the symmetric (antisymmetric) incoming wave

$$\psi_{\text{in}}(z) = \frac{1}{\sqrt{2}} (e^{ikz} \pm e^{-ikz}). \quad (4.14)$$

The corresponding differential and total scattering cross sections are

$$\frac{d\sigma}{d\Omega} = \frac{1}{2} |f_e(k, \theta) \pm f_e(k, \pi - \theta)|^2, \quad (4.15)$$

and

$$\sigma = \frac{8\pi}{k^2} \sum_{l^\pm} (2l+1) \sin^2 \delta_l, \quad (4.16)$$

respectively. The  $+$  ( $-$ ) sign applies to bosons (fermions) and  $l^+$  ( $l^-$ ) indicates that the sum is over the even (odd) integers.

#### 4.1.1 Low energy scattering

If an interaction decreasing asymptotically with a power-law dependence  $U(r) \simeq r^{-n}$   $n > 3$  is considered, it is shown [113], that in the limit  $k \rightarrow 0$  we have

$$f_l \propto \begin{cases} k^{2l} & \text{if } l < (n-3)/2, \\ k^{n-3} & \text{else.} \end{cases} \quad (4.17)$$

From this equation we can read off that, for low energies,  $f_l \ll f_0$  for any  $l > 0$ , and that the scattering amplitude tends to a constant value

$$\lim_{k \rightarrow 0} f_e(k, \theta) = \lim_{k \rightarrow 0} f_0(k) = -a. \quad (4.18)$$

yielding the asymptotic solution

$$\psi(\mathbf{r}) = e^{i\mathbf{k} \cdot \mathbf{r}} - a \frac{e^{ikr}}{r}. \quad (4.19)$$

Since the scattered wave (the second term of the left side of the above equation) decays over the length  $a$ , this constant can be interpreted as the correlation length associated to the particle-particle interaction. However, in the literature, one commonly refers to it as *scattering length*.

The total cross section for distinguishable particles follows from Eqs. (4.13) and (4.18) as

$$\sigma = 4\pi a^2 \quad (4.20)$$

On the other side, in the case of indistinguishable bosons, Eqs. (4.14) and (4.18) yield

$$\sigma = 8\pi a^2. \quad (4.21)$$

The total cross section for identical fermions vanishes, since it contains no  $s$ -wave contribution due to symmetry reasons.

We can conclude that, for any potential decreasing faster than  $1/r^3$ , the low energy scattering is isotropic and is described in terms of the scattering length  $a$  only.

The scattering length  $a$  can be determined accurately from a variety of experiments, e. g. photoassociative spectroscopy or analysis of Feshbach resonances, and



plays a central role in the theory of cold collisions. When only low energy states are involved in a collision process, we will see that the scattering length is the only parameter entering an effective interaction that can be substituted for the full two-body potential. This is very appealing, since the original potential is deep and has a complicated structure, that cannot generally be calculated analytically.

The above results has been derived starting from the formula in Eq. (4.17), valid when the wavelength of the incoming wave  $2\pi/k$  is the longest length scale in the problem. In particular,  $1/k$  should be larger than the scattering length  $a$ . In the following, we study in detail the the  $s$ -wave Schrödinger equation, corresponding to Eq. (4.4) with  $l = 0$ . We will show that the scattering is described in terms of the scattering length  $a$  only even for  $1/k < a$  provided that it is still larger than the microscopic range of the potential  $\alpha$ <sup>1</sup>. In this limit the cross section is energy dependent. Moreover, by solving Eq. (4.4) for small negative energy, we will explore the connection between the low energy scattering and the bound states near the threshold of the continuum spectrum.

We start by substituting  $\chi(r) = rR_0(r)$  in Eq. (4.4) with  $l = 0$  yielding

$$\chi''(r) + 2\mu[E - U(r)]\chi(r) = 0. \quad (4.22)$$

In the above equation, we have also substituted  $k^2$  with  $2\mu E$ , in this way pointing out that also negative energies are considered here. Note that, on one hand, one can neglect the term  $2\mu E\chi(r)$  for  $r \ll 1/\sqrt{2\mu|E|} \equiv 1/k$ . On the other hand, the term  $2\mu U(r)\chi(r)$  is negligible in the region  $r \gg \alpha$ . Hence, in the low energy limit  $1/k \gg \alpha$ , one can solve Eq. (4.22) separately in the regions  $r \ll 1/k$  and  $r \gg \alpha$  by neglecting the terms  $2\mu E\chi(r)$  and  $2\mu U(r)\chi(r)$ , respectively. One can then connect the two solutions in the region  $\alpha \ll r \ll 1/k$ , where both of them are valid. We denote these two approximate solutions as  $\chi_U(r)$  and  $\chi_E(r)$ , respectively. The solutions of Eq. (4.22), which correspond to a physical state, obey the boundary condition  $\chi(0) = 0$ . Each acceptable solution satisfy a different normalization condition, but the ratio  $\chi'(r)/\chi(r)$  is determined by the boundary condition at the origin. Thus, one can impose the matching condition

$$\frac{\chi'_U(r)}{\chi_U(r)} = \frac{\chi'_E(r)}{\chi_E(r)} = \varpi \quad \text{for } \alpha \ll r \ll 1/k \quad (4.23)$$

to connect the two solutions.  $\varpi$  is a constant, which depends only on the shape of the confining potential. In fact, it does not depend on the exact position  $r$  where the matching condition in Eq. (4.23) is imposed, as it follows from  $\chi''(r) \simeq 0$ , valid in the whole region  $\alpha \ll r \ll 1/k$ . Moreover, it must be independent from the energy since  $\chi_U(r)$  does not depend on this quantity. We can thus apply the same matching condition to different asymptotic solutions  $\chi_E(r)$  corresponding either to a low energy scattering solution or to a spherical symmetric bound state near the threshold of the continuum limit, when  $E$  is positive or negative, respectively.

---

<sup>1</sup>a reasonable quantitative definition of  $\alpha$  is  $1/(2\mu\alpha^2) = |U(\alpha)|$  (the length above which the kinetic energy exceeds the potential energy).

**s-wave low energy scattering**

We first consider the case  $E > 0$ . The function  $\chi_E(r)$  is the  $s$ -wave asymptotic solution

$$\chi_E(r) = A \sin(kr + \delta_0). \quad (4.24)$$

The multiplicative factor  $A$  in the above equation is fixed by the normalization condition and does not influence  $\varpi$ . By applying the matching condition Eq. (4.23) to  $\chi_E(r)$  we find

$$\cot \delta_0 = \frac{\varpi}{k}. \quad (4.25)$$

Note that the  $s$ -wave frequency shift  $\delta_0$  is not supposed to be small. In fact, the validity of this result is restricted only by the condition  $k \ll 1/\alpha$  and not by  $k \ll \varpi$ . The above equation together with Eq. (4.9) and the assumption that the contributions of the higher angular momentum modes are negligible for  $k \ll 1/\alpha$ , yields the scattering amplitude

$$f_e(k) = f_0(k) = \frac{1}{\varpi - ik}, \quad (4.26)$$

and the energy dependent cross section

$$\sigma = \frac{2\pi}{\varpi^2 + k^2}. \quad (4.27)$$

When  $k \ll |\varpi|$ , we find

$$f_e(k) = \varpi^{-1} \quad (4.28)$$

and

$$\sigma = \frac{2\pi}{\varpi^2}, \quad (4.29)$$

thereby identifying

$$\varpi = -a^{-1}. \quad (4.30)$$

In the opposite limit  $|a|$  is much larger than  $k^{-1}$  and the cross section saturates to the value  $\sigma = 4\pi/k^2$  and is said to be “unitarity limited”.

**Shape resonances**

Let us now consider the case  $E < 0$ . The asymptotic solution for a spherical symmetric bound state is

$$\chi_E(r) = A \exp\left(-\sqrt{-2\mu E}r\right). \quad (4.31)$$

By applying the matching condition Eq. (4.23) we get

$$a^{-1} = \sqrt{-2\mu E}. \quad (4.32)$$

Such equation has been derived under the assumption  $k = \sqrt{-2\mu E} \ll 1/\alpha$ . We can thus conclude that:

(i) On one hand, in presence of a scattering length  $a$ , which is positive and much larger than the range of the potential  $a \gg \alpha$ , there is a bound state with binding energy

$$E_B = (2\mu a^2)^{-1} \quad (4.33)$$

and size  $a$ .

(ii) Vice versa, if a potential has a bound state near the threshold of the continuum limit, meaning its binding energy fullfills the condition  $E_B \ll (2\mu\alpha^2)^{-1}$ , the scattering length  $a$  is very large in comparison to the microscopic length scale  $\alpha$  that characterizes the potential, resulting in a very large low-energy cross section.

In the literature, such a phenomenon is referred to as *shape resonance*, indicating that the scattering amplitude is resonant, when, due to the shape of the potential, a bound state close to the continuum threshold is present. By slightly changing the potential, the constant  $\varpi$  changes continuously. With an appropriate change, it can vanish and then assume a small negative value. The scattering length  $a$  changes accordingly from a large positive value to a large negative value. In the latter case, we say that the potential has a virtual bound state, having in mind that a small modification of the shape of the interaction could generate a real bound state.

### The Fermi pseudopotential

The total number of alkali atoms in an ultracold cloud is typically  $N \approx 10^4 - 10^7$  (up to  $10^{10}$  in BEC). A many-body description is appropriate for such a large ensemble of interacting particles. However, a many-body theory for particles interacting via the rather complicated Van der Waals potential would be hard to handle. For this reason, it is useful to consider few-body problems, in particular the two-body one, whose solutions can be employed as building blocks for a simplified effective many-body description.

Since the gas is very diluted, typical interparticle distances being an order of magnitude larger than the potential range, the three-body recombination is negligible. Moreover, the cloud is in the nano-Kelvin regime. Hence, an effective many-body theory of the metastable gas phase should include a two-body interaction term, which describes correctly the low-energy scattering. The bound state near the threshold of the continuum spectrum could be relevant if one is interested in studying the phase transition to a gas of diatomic molecules.

The main result of this section is that both the low-energy  $s$ -wave scattering and the bound state near the threshold of the continuum for a potential decreasing faster than  $1/r^3$  are described in terms of a single parameter, the scattering length  $a$ .

An effective interaction yielding the scattering amplitude

$$f_e(k) = -\frac{1}{a^{-1} + ik} \quad (4.34)$$

and whose range  $\alpha$  is much smaller than the modulus of the scattering length  $a$ , would reproduce the asymptotic scattering and shallow bound state (if present)

solutions of the original potential. The most convenient choice would be a zero-range interaction.

The potential, which responds to these requirements is the well known Fermi pseudopotential [112]

$$U(r) = \frac{2\pi a}{\mu} \delta(\mathbf{r}) \frac{\partial}{\partial r} r. \quad (4.35)$$

The derivative term has been introduced to regularize the contact potential at the origin, i.e. to give a definite meaning to the combination  $U(0)\psi(0)$  (remember that the asymptotic solution diverge like  $1/r$ ). In Appendix D we solve explicitly the two-body problem in free space using the pseudopotential to model the two-body interaction, in order to show explicitly that one recovers the scattering amplitude and the binding energy for the shallow bound state given in Eqs. (4.34) and (4.33), respectively.

In the following section we return to the main topic in the focus of this chapter: the scattering in presence of transversal confinement. In this different framework, the pseudopotential method has proved to be a reliable and powerful tool of investigation, and we, too, will adopt it. Since the derivation of the pseudopotential method as been carried out in free space, few comments on the extension of this method to a confined geometry are in order.

Note that the main assumption on which the pseudopotential method is based, is that there is a separation of length scales in the problem.

On one hand for short distances, one has to take into account the particle-particle interaction but the solution is not energy dependent. On the other hand, for large distances one can disregard the interaction term and recovers the asymptotic scattering or bound state solution. For intermediate distances, both solutions are valid and they can be connected by means of the matching condition given in Eq. (4.23), which depends on the shape of the potential only.

This is the only relevant information one needs to know in order to construct an effective low-energy theory. The pseudopotential is just the most convenient potential, which encodes such a matching condition.

In a confined geometry, very little changes: if the characteristic length associated with the confinement is much larger than the range of the potential  $\alpha$ , there is a separation of length scales. One is supposed to connect the short-distance solution with an asymptotic solution which depends on the confining potential and on the energy, but the matching condition remains the one in Eq. (4.23). It is thus clear, that the pseudopotential method is still valid.

## 4.2 The two-body problem in presence of transverse confinement

Let us consider the general case of two different atomic species with mass  $m_1$  and  $m_2$ . We denote the particle coordinates by  $\mathbf{x}_i = (\mathbf{x}_{\perp,i}, z_i)$  and their momenta by  $\mathbf{p}_i = (\mathbf{p}_{\perp,i}, p_{\parallel,i})$ . Different atoms may experience a different transversal confinement

potential  $V_i(\mathbf{x}_{\perp,i})$ . For ultracold atoms, only low-energy s-wave scattering is relevant, and the interaction between unlike atoms (and similarly, also the interaction between the same atoms) can be described by a Fermi pseudopotential  $U(|\mathbf{x}_1 - \mathbf{x}_2|)$ . Then the relevant Hamiltonian for two different atoms is given by

$$H = \frac{\mathbf{p}_1^2}{2m_1} + \frac{\mathbf{p}_2^2}{2m_2} + V_1(\mathbf{x}_{\perp,1}) + V_2(\mathbf{x}_{\perp,2}) + U(|\mathbf{x}_1 - \mathbf{x}_2|). \quad (4.36)$$

For further convenience, we transform to the relative/COM coordinates and momenta given by  $\mathbf{r} = (\mathbf{r}_{\perp}, z)$ ,  $\mathbf{R} = (\mathbf{R}_{\perp}, Z)$  and  $\mathbf{p} = (\mathbf{p}_{\perp}, p_{\parallel})$ ,  $\mathbf{P} = (\mathbf{P}_{\perp}, P_{\parallel})$ , respectively. This can be done by the canonical transformation

$$\begin{pmatrix} \mathbf{R} \\ \mathbf{r} \\ \mathbf{P} \\ \mathbf{p} \end{pmatrix} = \frac{1}{M} \begin{pmatrix} m_1 & m_2 & 0 & 0 \\ M & -M & 0 & 0 \\ 0 & 0 & M & M \\ 0 & 0 & m_2 & -m_1 \end{pmatrix} \begin{pmatrix} \mathbf{x}_1 \\ \mathbf{x}_2 \\ \mathbf{p}_1 \\ \mathbf{p}_2 \end{pmatrix}, \quad (4.37)$$

where  $M = m_1 + m_2$ . Since the confinement is assumed to be purely transversal, the longitudinal COM coordinate  $Z$  is free and decouples from the other degrees of freedom. Hence, we eliminate it by transforming into the longitudinal COM rest frame, where the state  $|\Psi\rangle$  of the system is determined by the set of coordinates  $(\mathbf{x}_{\perp,1}, \mathbf{x}_{\perp,2}, z)$  or, alternatively, by  $(\mathbf{R}_{\perp}, \mathbf{r}) = (\mathbf{R}_{\perp}, \mathbf{r}_{\perp}, z)$ . The transformed Hamiltonian takes the form

$$H = H_{\parallel} + H_{\perp,1} + H_{\perp,2} + U, \quad (4.38)$$

where

$$H_{\parallel} = \frac{p_{\parallel}^2}{2\mu}, \quad H_{\perp,i} = \frac{\mathbf{p}_{\perp,i}^2}{2m_i} + V_i(\mathbf{x}_{\perp,i}). \quad (4.39)$$

For a more compact notation, we introduce the non-interacting Hamiltonian  $H_0 = H - U$  and denote its eigenstates by

$$|k, \lambda_1, \lambda_2\rangle = e^{-ikz} \psi_{\lambda_1}^{(1)}(\mathbf{x}_{\perp,1}) \psi_{\lambda_2}^{(2)}(\mathbf{x}_{\perp,2}), \quad (4.40)$$

where  $\psi_{\lambda_i}^{(i)}$  are single-particle eigenstates of  $H_{\perp,i}$  for eigenvalue  $E_{\lambda_i}^{(i)}$ . Correspondingly, the two-particle Schrödinger equation is given by

$$(H_0 - E) \Psi(\mathbf{R}_{\perp}, \mathbf{r}) = -U(\mathbf{r}) \Psi(\mathbf{R}_{\perp}, \mathbf{r}). \quad (4.41)$$

The pseudopotential (4.35) can be enforced by the Bethe-Peierls boundary condition

$$\Psi(\mathbf{R}_{\perp}, \mathbf{r} \rightarrow 0) \simeq \frac{f(\mathbf{R}_{\perp})}{4\pi r} \left(1 - \frac{r}{a}\right), \quad (4.42)$$

leading to the inhomogeneous Schrödinger equation

$$(H_0 - E) \Psi(\mathbf{R}_{\perp}, \mathbf{r}) = \frac{f(\mathbf{R}_{\perp})}{2\mu} \delta(\mathbf{r}). \quad (4.43)$$

The solution of this equation can be formally obtained in terms of a solution of the homogeneous Schrödinger equation,  $(H_0 - E)\Psi_0 = 0$ , and the Green's function  $G_E = (H_0 - E)^{-1}$ ,

$$\Psi(\mathbf{R}_\perp, \mathbf{r}) = \Psi_0(\mathbf{R}_\perp, \mathbf{r}) + \int d\mathbf{R}'_\perp G_E(\mathbf{R}_\perp, \mathbf{r}; \mathbf{R}'_\perp, 0) \frac{f(\mathbf{R}'_\perp)}{2\mu}. \quad (4.44)$$

To determine  $f(\mathbf{R}_\perp)$ , we substitute Eq. (4.44) into Eq. (4.42) and find the integral equation

$$-\frac{f(\mathbf{R}_\perp)}{4\pi a} = \Psi_0(\mathbf{R}_\perp, 0) + \int d\mathbf{R}'_\perp \zeta_E(\mathbf{R}_\perp, \mathbf{R}'_\perp) f(\mathbf{R}'_\perp), \quad (4.45)$$

where we have defined the regularized integral kernel

$$\zeta_E(\mathbf{R}_\perp, \mathbf{R}'_\perp) = \lim_{r \rightarrow 0} \frac{1}{2\mu} \left( G_E(\mathbf{R}_\perp, \mathbf{r}; \mathbf{R}'_\perp, 0) - \delta(\mathbf{R}_\perp - \mathbf{R}'_\perp) \frac{\mu}{2\pi r} \right). \quad (4.46)$$

In Eqs. (4.44) and (4.45),  $\Psi_0$  can be expressed as a superposition of single-particle eigenstates  $|k, \lambda_1, \lambda_2\rangle$  with

$$\frac{k^2}{2\mu} + E_{\lambda_1}^{(1)} + E_{\lambda_2}^{(2)} = E. \quad (4.47)$$

We refer to the set of states with the same transverse occupation numbers  $\lambda_i$  but arbitrary longitudinal relative momentum as a *scattering channel* or, simply, *channel*. Each channel has a minimum energy given by  $E_{\lambda_1}^{(1)} + E_{\lambda_2}^{(2)}$ . Since the interaction is short-ranged, only states fulfilling Eq. (4.47) appear in the asymptotic solution. For each *open channel*,  $E > E_{\lambda_1}^{(1)} + E_{\lambda_2}^{(2)}$ , such that there are (at least) two such states having opposite momenta. For  $E$  just above  $E_0^{(1)} + E_0^{(2)}$ , there exists one open channel only. The corresponding solution given by Eq. (4.44) describes the scattering of two particles initially occupying the transverse ground-state. During the scattering process, the particles populate closed channels, but afterwards return into the single available open channel (quasi-1D picture). For  $E < E_0^{(1)} + E_0^{(2)}$ , all channels are closed and only bound-state solutions are possible. These are given by Eq. (4.44) with  $\Psi_0(\mathbf{R}_\perp, \mathbf{r}) = 0$ . In the following, we consider both classes of solutions in more detail.

### 4.3 Bound-state solutions

Let us consider the situation when all channels are closed and only bound states may occur. We define the binding energy of the bound states as

$$E_B = E_0 - E > 0, \quad (4.48)$$

where  $E_0 = E_0^{(1)} + E_0^{(2)}$  is the ground-state energy of  $H_0$ . To find bound states, we diagonalize the operator  $\zeta_E(\mathbf{R}_\perp, \mathbf{R}'_\perp)$  defined in Eq. (4.46), where Eq. (4.45) yields the condition

$$-\frac{f(\mathbf{R}_\perp)}{4\pi a} = \int d\mathbf{R}'_\perp \zeta_E(\mathbf{R}_\perp, \mathbf{R}'_\perp) f(\mathbf{R}'_\perp). \quad (4.49)$$

For given  $a$ , bound states with binding energy  $E_B = E_0 - E$  follow as solution of this eigenvalue problem. The bound-state wave function follows by inserting the corresponding eigenvector  $f(\mathbf{R}_\perp)$  into Eq. (4.44) with  $\Psi_0(\mathbf{R}_\perp, \mathbf{r}) = 0$ . In order to find a representation of  $\zeta_E(\mathbf{R}_\perp, \mathbf{R}'_\perp)$  allowing for straightforward analytical or numerical diagonalization, we use

$$G_E(\mathbf{R}_\perp, \mathbf{r}; \mathbf{R}'_\perp, 0) = \int_0^\infty dt e^{Et} G_t(\mathbf{R}_\perp, \mathbf{r}; \mathbf{R}'_\perp, 0), \quad (4.50)$$

with the imaginary-time evolution operator

$$G_t(\mathbf{R}_\perp, \mathbf{r}; \mathbf{R}'_\perp, 0) = \langle \mathbf{R}_\perp, \mathbf{r} | \exp[-H_0 t] | \mathbf{R}'_\perp, 0 \rangle \quad (4.51)$$

for  $H_0$ . The time evolution operator  $\exp[-H_0 t]$  can be factorized into the product  $\exp[-H_\parallel t] \exp[-H_{1,\perp} t] \exp[-H_{2,\perp} t]$ . The corresponding factors in  $G_t$  are

$$\langle z | \exp[-H_\parallel t] | z' \rangle = \left( \frac{\mu}{2\pi t} \right)^{1/2} e^{-(z-z')^2 \mu / 2t} \quad (4.52)$$

for the relative longitudinal coordinates and

$$\langle \mathbf{x}_{i,\perp} | \exp[-H_{i,\perp} t] | \mathbf{x}'_{i,\perp} \rangle = \sum_\lambda e^{-E_\lambda^{(i)} t} \psi_\lambda^{(i)}(\mathbf{x}_{i,\perp}) \bar{\psi}_\lambda^{(i)}(\mathbf{x}'_{i,\perp}) \quad (4.53)$$

for the transverse coordinates (the bar denotes complex conjugation). Thus  $G_t$  can be expressed in terms of the set of coordinates  $(\mathbf{x}_{\perp,1}, \mathbf{x}_{\perp,2}, z)$  as

$$G_t(\mathbf{R}_\perp, \mathbf{r}; \mathbf{R}'_\perp, 0) = \sqrt{\frac{\mu}{2\pi t}} e^{-z^2 \mu / 2t} \prod_{i=1,2} \sum_\lambda e^{-E_\lambda^{(i)} t} \psi_\lambda^{(i)}(\mathbf{x}_{\perp,i}) \bar{\psi}_\lambda^{(i)}(\mathbf{x}'_{\perp,i}). \quad (4.54)$$

This equation illustrates that for large imaginary times the integrand in Eq. (4.50) decays as  $\exp[-E_B t]$ . Notice that this representation is valid for  $E_B > 0$ . By using

$$\frac{\mu}{2\pi r} = \int_0^\infty dt \left( \frac{\mu}{2\pi t} \right)^{3/2} e^{-r^2 \mu / 2t} \quad (4.55)$$

we find

$$\zeta_E(\mathbf{R}_\perp, \mathbf{R}'_\perp) = \int_0^\infty \frac{dt}{2\mu} \left[ e^{Et} G_t(\mathbf{R}_\perp, 0; \mathbf{R}'_\perp, 0) - \left( \frac{\mu}{2\pi t} \right)^{3/2} \delta(\mathbf{R}_\perp - \mathbf{R}'_\perp) \right]. \quad (4.56)$$

To show that the integral in Eq. (4.56) converges also for small  $t$ , we expand  $G_t(\mathbf{R}_\perp, 0; \mathbf{R}'_\perp, 0)$  with respect to  $t$ , see Appendix E. We find

$$\begin{aligned} \lim_{t \rightarrow 0} G_t(\mathbf{R}_\perp, 0; \mathbf{R}'_\perp, 0) &= \left( \frac{\mu}{2\pi t} \right)^{3/2} \delta(\mathbf{R}_\perp - \mathbf{R}'_\perp) - t^{-1/2} \left( \frac{\mu}{2\pi} \right)^{3/2} \\ &\quad \times \left[ \frac{\mathbf{P}_\perp^2}{2M} + V_1(\mathbf{R}_\perp) + V_2(\mathbf{R}_\perp) \right]. \end{aligned} \quad (4.57)$$

Thus,  $\zeta_E$  can be regarded as a regular operator acting on the space  $\mathcal{L}^2$  of square-integrable functions. We note in passing that if the two single-particle transverse Hamiltonians  $H_{\perp,i}$  commute with the angular momentum operators  $L_z$ , then also  $\zeta_E$  commutes with  $L_z$ . This follows by observing that in this case we can choose for the eigenbasis  $\{\psi_\lambda^{(i)}\}$  a set of eigenvectors of  $L_z$ , and the product of two eigenvectors of  $L_z$  is still an eigenvector of  $L_z$ . Hence  $\zeta_E(\mathbf{R}_\perp, \mathbf{R}'_\perp)$  can be written as a sum of projectors onto states with definite angular momentum. A similar conclusion can be drawn regarding parity symmetry, when considering non-cylindrical confining potentials that obey this symmetry.

From Eq. (4.54) it is clear that the integrand in Eq. (4.50) decays as  $\exp[-E_B t]$  for large imaginary times and as  $\exp[-z^2 \mu / (2t)]$  for short imaginary times, yielding the condition  $z < 1/\sqrt{\mu E_B}$ . We can conclude that the longitudinal size of the bound state is  $a_B = 1/\sqrt{\mu E_B}$  provided that the overlap integral in Eq. (4.44)  $\int d\mathbf{R}'_\perp \bar{\psi}_0(\mathbf{R}'_\perp, 0) f(\mathbf{R}'_\perp) \neq 0$ , with

$$\psi_0(\mathbf{R}_\perp, \mathbf{r}_\perp) = \psi_0^{(1)}\left(\mathbf{R}_\perp + \frac{\mu}{m_1} \mathbf{r}_\perp\right) \psi_0^{(2)}\left(\mathbf{R}_\perp - \frac{\mu}{m_2} \mathbf{r}_\perp\right) \quad (4.58)$$

being the transverse non-interacting ground-state. For large  $E_B$ ,  $a_B$  is small and we have very tight pairs. This constitutes the *dimer limit*. On the other hand, for small  $E_B$ , atom pairs are very elongated. This regime is termed *BCS limit*. In the following, we investigate both limits in greater detail.

### 4.3.1 Dimer limit

For large binding energies, the atom-atom interaction dominates over the confinement. Due to the exponential factors in Eq. (4.56), only small imaginary times contribute significantly to the integral, and we can substitute  $G_t$  with the short-time expansion (4.57) as derived in the Appendix E, yielding

$$\begin{aligned} \zeta_E(\mathbf{R}_\perp, \mathbf{R}'_\perp) &\simeq \left(\frac{\mu}{2\pi}\right)^{3/2} \int_0^\infty \frac{dt}{2\mu} (t^{-3/2} (e^{Et} - 1) \delta(\mathbf{R}_\perp - \mathbf{R}'_\perp) \\ &\quad - e^{Et} t^{-1/2} \langle \mathbf{R}_\perp | H_\perp | \mathbf{R}'_\perp \rangle) . \end{aligned} \quad (4.59)$$

Hence, the operator  $\zeta_E$  now shares eigenfunctions with  $H_\perp = \mathbf{P}_\perp^2 / 2M + V_1(\mathbf{R}_\perp) + V_2(\mathbf{R}_\perp)$ . For (identical) parabolic confinement potentials,  $H_\perp$  is exactly the decoupled COM Hamiltonian. Let us denote the eigenfunctions and eigenenergies of  $H_\perp$  as  $\phi_\lambda(\mathbf{R}_\perp)$  and  $E_\lambda^{(\phi)}$ , respectively. Substituting  $\phi_\lambda(\mathbf{R}_\perp)$  into Eq. (4.49) yields after some algebra

$$-\frac{1}{4\pi a} = -\frac{\sqrt{2\mu|E|}}{4\pi} \left(1 + \frac{E_\lambda^{(\phi)}}{2|E|}\right) \simeq -\frac{\sqrt{2\mu E_B}}{4\pi}. \quad (4.60)$$

In the second relation, we have used Eq. (4.48). From this, we directly obtain the binding energy in the dimer limit  $a \rightarrow 0^+$  as

$$E_B \approx \frac{1}{2\mu a^2}, \quad (4.61)$$

which coincides with the result obtained in free (3D) space without confinement.



### 4.3.2 BCS limit

The scattering channel with lowest energy, corresponding to the transverse non-interacting ground-state  $\psi_0$ , opens at the energy threshold  $E = E_0$ . For  $E_B \rightarrow 0^+$ , as the energy approaches this threshold, the term with  $\lambda_1 = \lambda_2 = 0$  dominates in Eq. (4.54), and yields in Eq. (4.56) the contribution

$$\sqrt{\frac{1}{8\mu E_B}} \psi_0(\mathbf{R}_\perp, 0) \bar{\psi}_0(\mathbf{R}'_\perp, 0), \quad (4.62)$$

which diverges for  $E_B \rightarrow 0^+$ . All other channels are still closed at  $E = E_0$  and give finite contributions in Eq. (4.54). This observation suggests a useful separation of the total Hilbert space into a part  $\mathcal{H}_o$  corresponding to the open channel (or lowest-energy scattering channel) and a part  $\mathcal{H}_e$  perpendicular to that. With this separation, terms yielding a finite contribution at  $E_B \rightarrow 0^+$  can be summarized in the Green's function

$$\tilde{G}_t(\mathbf{R}_\perp, \mathbf{r}; \mathbf{R}'_\perp, 0) = \langle \mathbf{R}_\perp, \mathbf{r} | \exp[-\tilde{H}_0 t] | \mathbf{R}'_\perp, 0 \rangle, \quad (4.63)$$

where  $\tilde{H}_0$  is the projection of  $H_0$  onto the Hilbert subspace  $\mathcal{H}_e$ . We then define a new integral kernel,

$$\tilde{\zeta}_E(\mathbf{R}_\perp, \mathbf{R}'_\perp) = \int_0^\infty \frac{dt}{2\mu} \left[ e^{Et} \tilde{G}_t(\mathbf{R}_\perp, 0; \mathbf{R}'_\perp, 0) - \left( \frac{\mu}{2\pi t} \right)^{3/2} \delta(\mathbf{R}_\perp - \mathbf{R}'_\perp) \right], \quad (4.64)$$

which is also well-defined for energies above the threshold  $E = E_0$ .

For small  $E_B$ , Eq. (4.49) is most conveniently solved by expanding  $f(\mathbf{R}_\perp)$  in an orthonormal basis  $|j\rangle$  according to

$$|f\rangle = \sum_j f_j |j\rangle, \quad f_j = \int d\mathbf{R}_\perp \langle j | \mathbf{R}_\perp \rangle f(\mathbf{R}_\perp), \quad (4.65)$$

where the basis state  $|0\rangle$  corresponds to

$$\langle \mathbf{R}_\perp | 0 \rangle = c \psi_0(\mathbf{R}_\perp, 0), \quad (4.66)$$

with normalization constant  $c$ . Although  $\psi_0(\mathbf{R}_\perp, \mathbf{r})$  is a normalized element of the two-particle Hilbert space, this does not imply that  $\psi_0(\mathbf{R}_\perp, 0)$  is an element of the COM Hilbert space with norm unity. In fact, the normalization constant  $c$  has to be computed explicitly and generally depends on the particular confinement. In this basis, Eq. (4.49) assumes the compact form

$$-\frac{|f\rangle}{4\pi a} = \zeta_E |f\rangle = \left( \sqrt{\frac{1}{8\mu E_B}} \frac{|0\rangle\langle 0|}{c^2} + \tilde{\zeta}_E \right) |f\rangle. \quad (4.67)$$

$|0\rangle$  is an approximate eigenstate for small  $E_B$ , since all the matrix elements are finite apart from  $\langle 0 | \zeta_E | 0 \rangle$  which diverges according to

$$\langle 0 | \zeta_E | 0 \rangle \simeq \sqrt{\frac{1}{8\mu E_B}} \frac{1}{c^2} + \langle 0 | \tilde{\zeta}_E | 0 \rangle. \quad (4.68)$$

Substituting this in Eq. (4.67) yields

$$-\frac{1}{4\pi a} \simeq \sqrt{\frac{1}{8\mu E_B}} \frac{1}{c^2} + \langle 0 | \tilde{\zeta}_E | 0 \rangle. \quad (4.69)$$

Neglecting the last term, the relation for the binding energy  $E_B$  is solved in the BCS limit  $a \rightarrow 0^-$ ,

$$E_B \approx \frac{2a^2\pi^2}{\mu c^4}. \quad (4.70)$$

## 4.4 Scattering solutions

In this section, we focus on scattering solutions at low energies  $E$  slightly above  $E_0$ , where exactly one transverse channel is open. Then, the incoming state is given by

$$\Psi_0 = e^{ikz} \psi_0^{(1)}(\mathbf{x}_{1,\perp}) \psi_0^{(2)}(\mathbf{x}_{2,\perp}), \quad (4.71)$$

which describes two incoming atoms with (small) relative longitudinal momentum  $k = \sqrt{2m(E - E_0)}$  in the (transverse) single-particle ground-states  $\psi_0^{(1)}$  and  $\psi_0^{(2)}$ , respectively.

### 4.4.1 One-dimensional scattering length $a_{1D}$

As done in Sec. 4.3, we split off the contribution from the open channel,

$$G_E(\mathbf{R}_\perp, \mathbf{r}; \mathbf{R}'_\perp, 0) = \psi_0(\mathbf{R}_\perp, \mathbf{r}_\perp) \bar{\psi}_0(\mathbf{R}'_\perp, 0) \frac{i\mu}{k} e^{ik|z|} + \int_0^\infty dt e^{Et} \tilde{G}_t(\mathbf{R}_\perp, \mathbf{r}; \mathbf{R}'_\perp, 0), \quad (4.72)$$

where  $\tilde{G}_t(\mathbf{R}_\perp, z; \mathbf{R}'_\perp, 0)$  is the Green's function restricted to  $\mathcal{H}_e$ , which is well-defined also above  $E_0$ . Inserting Eq. (4.72) into Eq. (4.44) yields for  $|z| \rightarrow \infty$  the standard scattering solution,

$$\Psi(\mathbf{R}, \mathbf{r}) = \psi_0(\mathbf{R}_\perp, \mathbf{r}_\perp) (e^{ikz} + f_e(k) e^{ik|z|}), \quad (4.73)$$

with scattering amplitude

$$f_e(k) = \frac{i}{2k} \int d\mathbf{R}'_\perp \bar{\psi}_0(\mathbf{R}'_\perp, 0) f(\mathbf{R}'_\perp), \quad (4.74)$$

whereas for short distances, also the term  $\int d\mathbf{R}'_\perp \int_0^\infty dt e^{Et} \tilde{G}_t(\mathbf{R}_\perp, \mathbf{r}; \mathbf{R}'_\perp, 0) f(\mathbf{R}'_\perp)$  appears in the scattering solution. Since the energy is well below the continuum threshold for the closed channels, this must be regarded as a sum over localized states. Enforcing the boundary condition (4.42) then leads to an integral equation for  $f(\mathbf{R}_\perp)$ ,

$$\begin{aligned} -\frac{f(\mathbf{R}_\perp)}{4\pi a} &= \int d\mathbf{R}'_\perp \tilde{\zeta}_E(\mathbf{R}_\perp, \mathbf{R}'_\perp) f(\mathbf{R}'_\perp) \\ &+ \psi_0(\mathbf{R}_\perp, 0) + \frac{i\psi_0(\mathbf{R}_\perp, 0)}{2k} \int d\mathbf{R}'_\perp \bar{\psi}_0(\mathbf{R}'_\perp, 0) f(\mathbf{R}'_\perp). \end{aligned} \quad (4.75)$$

This integral equation is most conveniently solved by again expanding  $f(\mathbf{R}_\perp)$  in the orthonormal basis  $\{|j\rangle\}$  introduced in the previous section. Thereby, we can express Eq. (4.75) in compact notation,

$$-\frac{|f\rangle}{4\pi a} = \frac{|0\rangle}{c} + \frac{i}{2k} \frac{|0\rangle}{c^2} \langle 0|f\rangle + \tilde{\zeta}_E |f\rangle, \quad (4.76)$$

which is formally solved by

$$|f\rangle = \frac{-1/c}{1 - i/(ka_{1D})} \left( \tilde{\zeta}_E + \frac{1}{4\pi a} \right)^{-1} |0\rangle. \quad (4.77)$$

The parameter  $a_{1D}$  follows in the form

$$a_{1D} = -\frac{2c^2}{\langle 0|[\tilde{\zeta}_E + 1/(4\pi a)]^{-1}|0\rangle}. \quad (4.78)$$

From Eq. (4.74),  $f_e(k) = -1/(1 + ik a_{1D})$ , which allows to identify  $a_{1D}$  with the *1D scattering length*. Having introduced this parameter, the 1D atom-atom interaction potential can then be written in an effective form according to

$$V_{1D}(z, z') = g_{1D} \delta(z - z'), \quad (4.79)$$

with interaction strength  $g_{1D} = -1/(\mu a_{1D})$  [28]. For very low energies,  $k \rightarrow 0$ , we can now formally set  $E = E_0$  in Eq. (4.78). For a confining trap,  $\tilde{\zeta}_{E_0}$  is an Hermitian operator with discrete spectrum  $\{\lambda_n\}$  and eigenvectors  $|e_n\rangle$ , which eventually have to be determined for the particular Hamiltonian. Thus we find

$$g_{1D} = \frac{1}{2\mu c^2} \sum_n \frac{|\langle 0|e_n\rangle|^2}{\lambda_n + 1/(4\pi a)}. \quad (4.80)$$

This result has interesting consequences for the two-body interaction. The denominator can become singular for particular values of  $a$ , thereby generating a CIR. Every eigenvalue  $\lambda_n$  corresponds to a different CIR, unless the overlap  $\langle 0|e_n\rangle$  vanishes due to some underlying symmetry of the Hamiltonian. We anticipate that for identical parabolic confinement potentials, the decoupling of the COM motion implies that only one resonance is permitted. For confining potentials with cylindrical symmetry, there is a resonance for each eigenvector of  $\tilde{\zeta}_{E_0}$  with zero angular momentum. For confining potentials obeying parity symmetry, the eigenstates  $|e_n\rangle$  must be even. These two symmetries allow in principle for infinitely many resonances. In practice, however, only few of them can be resolved because the resonances become increasingly sharper when  $|\langle 0|e_n\rangle|^2 \rightarrow 0$ , making them difficult to detect.

#### 4.4.2 Interpretation of the CIR as Feshbach resonances

A very simple and illuminating analysis, similar to that for standard Feshbach resonances [39], is also possible for the CIR. The two-particle Schrödinger equation

can be rewritten as an effective Schrödinger equation for the scattering states in the open channel,  $(E - H_{\text{eff}})\mathcal{P}|\Psi\rangle = 0$ , with the effective Hamiltonian

$$H_{\text{eff}} = H_{\text{open}} + \mathcal{P}H\mathcal{M}\frac{1}{E - H_{\text{closed}}}\mathcal{M}H\mathcal{P}. \quad (4.81)$$

Here,  $H_{\text{open}} = \mathcal{P}H\mathcal{P}$  and  $H_{\text{closed}} = \mathcal{M}H\mathcal{M}$ , where  $\mathcal{P}$  and  $\mathcal{M}$  are projectors to open and closed channels, respectively. This equation can be expressed in terms of the closed-channel eigenstates  $|\Phi_n\rangle$ ,

$$H_{\text{eff}} = H_{\text{open}} + \mathcal{P}H \sum_n \frac{|\Phi_n\rangle\langle\Phi_n|}{E - E_n} H\mathcal{P}, \quad (4.82)$$

with  $H_{\text{closed}}|\Phi_n\rangle = E_n|\Phi_n\rangle$ . This implies that a Feshbach-like resonance is possible at zero momentum if two conditions are fulfilled. First, there exists a solution of  $(E_0 - H_{\text{closed}})|\Phi\rangle = 0$ , i.e.,  $|\Phi\rangle$  is a bound state of  $H_{\text{closed}}$  with energy  $E = E_0$ . Second,  $|\Phi\rangle$  must be coupled to the open channel,  $\mathcal{P}H|\Phi\rangle \neq 0$ .

Within the pseudopotential approximation, the equation  $(E_0 - H_{\text{closed}})|\Phi\rangle = 0$  is solved in terms of the Green's function

$$\mathcal{M}G_{E_0}(\mathbf{R}_\perp, \mathbf{r}; \mathbf{R}'_\perp, 0)\mathcal{M} = \int_0^\infty dt e^{E_0 t} \tilde{G}_t(\mathbf{R}_\perp, \mathbf{r}; \mathbf{R}'_\perp, 0) \quad (4.83)$$

by the state

$$\Phi(\mathbf{R}_\perp, \mathbf{r}) = \int d\mathbf{R}'_\perp \mathcal{M}G_{E_0}(\mathbf{R}_\perp, \mathbf{r}; \mathbf{R}'_\perp, 0)\mathcal{M} \frac{f(\mathbf{R}'_\perp)}{2\mu}, \quad (4.84)$$

together with the boundary condition

$$\Phi(\mathbf{R}_\perp, \mathbf{r} \rightarrow 0) \simeq \frac{f(\mathbf{R}_\perp)}{4\pi r} \left(1 - \frac{r}{a}\right). \quad (4.85)$$

This leads to the eigenvalue equation

$$-\frac{|f\rangle}{4\pi a} = \tilde{\zeta}_{E_0}|f\rangle, \quad (4.86)$$

which is solved by the eigenvectors  $|e_n\rangle$  introduced above. This yields  $a = -1/(4\pi\lambda_n)$ , implying that there is a bound state  $|\Phi\rangle$  of  $H_{\text{closed}}$  with energy equal to the energy of the incoming wave, corresponding to the resonances found in the previous subsection. The CIR is then in complete analogy to a zero-momentum Feshbach resonance. Due to the small but finite coupling to the closed channels, two incoming particles initially in the open channel visit the closed channels during the scattering process. This process is strongly intensified when a bound-state exists whose energy is close to the continuum threshold. Then, a scattering resonance results. Note that such a bound state can be occupied only virtually by two particles during the scattering process. Hence from now on we will refer to such a bound state as a virtual bound state.

It is also possible to recover the overlap condition  $\langle 0|e_n\rangle \neq 0$  in this framework. In fact,

$$\mathcal{P}H\Phi(\mathbf{R}_\perp, \mathbf{r}) = \mathcal{P}U(\mathbf{r})\Phi(\mathbf{R}_\perp, \mathbf{r}) = -\mathcal{P}\frac{\langle \mathbf{R}_\perp|e_n\rangle}{2\mu}\delta(\mathbf{r}) = -\psi_0(\mathbf{R}_\perp, \mathbf{r}_\perp)\delta(z)\frac{\langle 0|e_n\rangle}{2\mu c}, \quad (4.87)$$

since  $|\Phi\rangle$  fulfills Eq. (4.85) with  $f(\mathbf{R}) = \langle \mathbf{R}_\perp|e_n\rangle$ . Hence, the two overlap conditions

$$\mathcal{P}H|\Phi\rangle \neq 0 \quad \Leftrightarrow \quad \langle 0|e_n\rangle \neq 0 \quad (4.88)$$

are equivalent. When they are not fulfilled, there exists a virtual bound state with energy  $E_0$ , but it is not coupled to the incoming wave.

## 4.5 Special case of harmonic confinement

In the previous sections, we have formulated the theory for a general confining potential and for two different atomic species. As a simple illustration, we now consider the case of harmonic confinement,  $V_i(\mathbf{x}_i) = m_i\omega_i^2\mathbf{x}_{i\perp}^2/2$ . In COM and relative coordinates,

$$V_{\text{conf}}(\mathbf{R}_\perp, \mathbf{r}_\perp) = \frac{1}{2}(m_1\omega_1^2 + m_2\omega_2^2)|\mathbf{R}_\perp|^2 + \frac{1}{2}\left(\frac{\mu^2}{m_1}\omega_1^2 + \frac{\mu^2}{m_2}\omega_2^2\right)|\mathbf{r}_\perp|^2 + \mu(\omega_1^2 - \omega_2^2)\mathbf{r}_\perp \cdot \mathbf{R}_\perp. \quad (4.89)$$

In general, the COM and the relative coordinates do not decouple, and in order to find the scattering and bound-state solutions, we have to follow the procedure outlined in the previous sections. To that end, we label the single-particle transverse states by quantum numbers  $\lambda = \{m, n\}$ , where  $m$  is the integer angular momentum and  $n$  the integer radial quantum number. The eigenenergies and -states of the 2D harmonic oscillator

$$E_\lambda^{(i)} = \omega_i\epsilon_{n,m}, \quad \psi_\lambda^{(i)} = \frac{1}{a_i}\psi_{n,m}\left(\frac{\mathbf{x}_\perp}{a_i}\right), \quad (4.90)$$

with the oscillator lengths  $a_i = (m_i\omega_i)^{-1/2}$ ,  $i = 1, 2$ , can be expressed in terms of the quantities

$$\epsilon_{n,m} = 2n + |m| + 1 \quad \text{and} \quad \psi_{n,m}(\mathbf{x}_\perp) = e^{im\phi} R_{n,m}(|\mathbf{x}_\perp|), \quad (4.91)$$

where

$$R_{n,m}(\rho) = \frac{1}{\sqrt{\pi}} \left( \frac{n!}{(n+|m|)!} \right)^{1/2} e^{-\rho^2/2} \rho^{|m|} L_n^{|m|}(\rho^2), \quad (4.92)$$

with  $L_n^{|m|}(x)$  being the standard Laguerre polynomials. A convenient choice for the orthonormal basis  $|j\rangle$  introduced in Eq. (4.65) is then given by

$$\langle \mathbf{R}_\perp|j\rangle = \langle \mathbf{R}_\perp|m, n\rangle = \frac{1}{a_M}\psi_{n,m}\left(\frac{|\mathbf{R}_\perp|}{a_M}\right), \quad (4.93)$$

with the length scale  $a_M = (m_1\omega_1 + m_2\omega_2)^{-1/2}$ . In particular, we find for  $|0\rangle = |0, 0\rangle$  that  $\langle \mathbf{R}_\perp | 0 \rangle$  fulfills Eq. (4.66) with  $c = \sqrt{\pi}a_1a_2/a_M$ .

The single-particle imaginary-time propagator for a 2D harmonic oscillator with length scale  $a_0$  and frequency  $\omega$  is given by

$$\begin{aligned} & \sum_\lambda e^{-\omega\epsilon_\lambda t} \frac{1}{a_0^2} \psi_\lambda \left( \frac{\mathbf{x}_\perp}{a_0} \right) \bar{\psi}_\lambda \left( \frac{\mathbf{x}'_\perp}{a_0} \right) \\ &= \frac{1}{\pi a_0^2} \frac{e^{-\omega t}}{1 - e^{-2\omega t}} \exp \left[ -\frac{\mathbf{x}_\perp^2 + \mathbf{x}'_\perp{}^2}{2a_0^2} \coth(\omega t) + \frac{\mathbf{x}_\perp \cdot \mathbf{x}'_\perp}{a_0^2 \sinh(\omega t)} \right]. \end{aligned} \quad (4.94)$$

Inserting this into Eq. (4.54) with  $\mathbf{x}_{\perp,i} = \mathbf{R}_\perp$ ,  $\mathbf{x}'_{\perp,i} = \mathbf{R}'_\perp$  and  $z = 0$ , we find

$$\begin{aligned} G_t(\mathbf{R}_\perp, 0; \mathbf{R}'_\perp, 0) &= \sqrt{\frac{\mu}{2\pi t}} \frac{\beta(1-\beta)}{\pi^2 a_M^4} \frac{e^{-\omega_1 t}}{1 - e^{-2\omega_1 t}} \frac{e^{-\omega_2 t}}{1 - e^{-2\omega_2 t}} \\ &\quad \times \exp \left[ -\frac{\mathbf{R}_\perp^2 + \mathbf{R}'_\perp{}^2}{2a_M^2} f(t) + \frac{\mathbf{R}_\perp \cdot \mathbf{R}'_\perp}{a_M^2} g(t) \right], \end{aligned} \quad (4.95)$$

where we have introduced  $\beta = a_M^2/a_1^2$  and

$$\begin{aligned} f(t) &= \beta \coth(\omega_1 t) + (1 - \beta) \coth(\omega_2 t), \\ g(t) &= \beta \sinh^{-1}(\omega_1 t) + (1 - \beta) \sinh^{-1}(\omega_2 t). \end{aligned} \quad (4.96)$$

In order to compute explicitly the operators  $\zeta_E$  and  $\tilde{\zeta}_E$ , we still have to project onto the discrete basis  $\{|j\rangle\}$  and to perform the imaginary-time integral for each matrix element. In general, this cannot be achieved analytically, and one has to resort to a numerical evaluation. Only for  $\omega_1 = \omega_2$ , a complete analytical solution is possible. Since the COM degrees of freedom separate, this solution is a trivial extension of Ref. [28]. Nonetheless, along with the general analysis of the previous section, it provides a physical picture for weak interaction between the COM and the relative degrees of freedom.

#### 4.5.1 Identical frequencies

For  $\omega_1 = \omega_2 = \omega$ , the COM and relative coordinates separate,  $H = H_{\text{rel}} + H_{\text{COM}}$ , with

$$H_{\text{rel}} = \frac{\mathbf{p}^2}{2\mu} + \frac{1}{2}\mu\omega^2 \mathbf{r}_\perp^2 + V(\mathbf{r}), \quad H_{\text{COM}} = \frac{\mathbf{P}^2}{2M} + \frac{1}{2}M\omega^2 \mathbf{R}_\perp^2. \quad (4.97)$$

In this case, we can consider the two-particle system being (asymptotically) in the ground-state of the decoupled COM Hamiltonian, and just solve the relative problem [28, 29]. Moreover, with  $f(t) = \coth(\omega t)$  and  $g(t) = \sinh^{-1}(\omega t)$ , the Green's function (4.95) simplifies to

$$G_t(\mathbf{R}_\perp, 0; \mathbf{R}'_\perp, 0) = \sqrt{\frac{\mu}{2\pi t}} \frac{\beta(1-\beta)}{\pi a_M^2} \frac{e^{-\omega t}}{1 - e^{-2\omega t}} \sum_{n,m} e^{-\omega\epsilon_{n,m} t} \frac{1}{a_M^2} \psi_{n,m} \left( \frac{\mathbf{R}_\perp}{a_M} \right) \bar{\psi}_{n,m} \left( \frac{\mathbf{R}'_\perp}{a_M} \right). \quad (4.98)$$

In this case,  $|n, m\rangle$  is an eigenstate of the decoupled Hamiltonian  $H_{\text{COM}}$ , and describes the COM motion also for finite  $\mathbf{r}$ . Moreover,  $a_M = (M\omega)^{-1/2}$  and  $a_\mu = a_M/(\beta(1-\beta)) = (\mu\omega)^{-1/2}$  are the characteristic lengths associated with  $H_{\text{COM}}$  and  $H_{\text{rel}}$ , respectively. Inserting Eq. (4.98) into Eq. (4.56) and rescaling  $t$  by  $2\omega$ , we obtain

$$\zeta_E = \sum_{n,m} \frac{|n, m\rangle\langle n, m|}{4\pi a_\mu} \int_0^\infty \frac{dt}{(\pi t)^{1/2}} \left( \frac{e^{-\Omega_{n,m}(E)t}}{1 - e^{-t}} - \frac{1}{t} \right), \quad (4.99)$$

with  $\Omega_{n,m}(E) = (1 + \epsilon_{n,m} - E/\omega)/2$ . The integral on the rhs of Eq. (4.99) is related to the integral representation of the Hurvitz zeta function  $\zeta(1/2, \Omega_{n,m})$  [27, 114].

### Bound states

The condition given in Eq. (4.49) for a bound state with transverse configuration  $|n, m\rangle$  translates into

$$\zeta\left(\frac{1}{2}, \Omega_{n,m}\right) = -\frac{a_\mu}{a}. \quad (4.100)$$

The zeta function is monotonic, and has the asymptotic scaling behavior

$$\zeta\left(\frac{1}{2}, \Omega \ll 1\right) \approx \Omega^{-1/2}, \quad \zeta\left(\frac{1}{2}, \Omega \gg 1\right) \approx -2\sqrt{\Omega}. \quad (4.101)$$

Inverting Eq. (4.100), we recover the bound-state energy found in Ref. [29]. The corresponding result is plotted in Fig. 4.1. As an immediate consequence of the decoupling of the COM degrees of freedom, the  $\epsilon_\lambda$ -fold degenerate energies corresponding to excited transverse configurations follow from the COM transverse ground-state by a shift along the ordinate in steps of  $\omega$ . This is indicated by the dotted curves in Fig. 4.1. Notice that for energies above  $E_0 = 2\omega$ , corresponding to  $E_B = 2\omega\Omega_{0,0}(E) < 0$ , there exists an open channel, but the solutions associated with COM excited states are orthogonal to it. For this reason, the relevant condition for a bound state to exist with transverse configuration  $|n, m\rangle$  is  $\Omega_{n,m}(E) > 0$ . From the scaling behaviors in Eq. (4.101), we find the limiting behaviors of the energy of the bound state at  $|a_\mu/a| \gg 1$  as

$$\begin{aligned} E_{B,n,m} &\approx \frac{1}{2\mu a^2} \quad \text{for } a > 0, \\ E_{B,n,m} &\approx \frac{2a^2}{\mu a_\mu^4} \quad \text{for } a < 0, \end{aligned} \quad (4.102)$$

see Eqs. (4.61) and (4.70), with  $c = \sqrt{\pi}a_\mu$  and  $E_{B,n,m} = \omega\Omega_{n,m}$ . Hence, in this highly degenerate case, there is exactly one bound state for each transverse configuration and each scattering length  $a$ .

### Scattering states

In order to identify resonant bound states of the closed channel, and the corresponding zero-momentum CIR, we subtract the contribution of the lowest-energy

scattering channel in Eq. (4.99), and obtain

$$\begin{aligned}\tilde{\zeta}_E &= \zeta_E - \frac{|0,0\rangle\langle 0,0|}{4\pi a_\mu} \int_0^\infty \frac{dt}{(\pi t)^{1/2}} e^{-\Omega_0(E)t} \\ &= \sum_{n,m} \frac{|n,m\rangle\langle n,m|}{4\pi a_\mu} \zeta(1/2, \tilde{\Omega}_{n,m}(E)),\end{aligned}\quad (4.103)$$

with  $\tilde{\Omega}_{0,0}(E) = \Omega_{0,0}(E) + 1$  and  $\tilde{\Omega}_{n,m}(E) = \Omega_{n,m}(E)$  for  $n + |m| > 0$ . Hence the curve corresponding to the COM ground-state is shifted vertically by  $2\omega$  and coincides with the curve corresponding to the excited states  $|1,0\rangle$ ,  $|0,2\rangle$  and  $|0,-2\rangle$ . Moreover, the coupling condition in Eq. (4.88) becomes  $\langle 0,0|n,m\rangle \neq 0$ , and is fulfilled only for  $n = m = 0$ . Though there are in principle infinitely many closed-channel bound states with energy  $2\omega$  (one for each curve), only one scattering resonance exists, since only one of them is coupled to the incoming scattering wave. Inserting Eq. (4.103) into Eq. (4.80) we recover for the 1D interaction strength  $g_{1D}$  the well known result [28]

$$g_{1D} = 2\omega a_\mu \left( \frac{a_\mu}{a} - \mathcal{C} \right)^{-1}. \quad (4.104)$$

### Physical picture for the weakly interacting case

When  $\omega_1 \neq \omega_2$  but  $\omega_1 \approx \omega_2$ , a weak coupling to the COM degrees of freedom is generated, with two important consequences: (i) the degeneracies of the bound-state energies are lifted, and (ii) the coupling to the other higher-lying bound states is non-zero. Since the operators  $\tilde{\zeta}_E$  and  $\zeta_E$  commute with the  $z$ -component  $L_z$  of the angular momentum, the bound states are still labeled by the quantum numbers  $\{n, m\}$ . As far as the scattering solutions are concerned, the incoming wave is coupled only to states with angular momentum quantum number  $m = 0$ . Since  $\langle 0,0|\tilde{\zeta}_E|0,0\rangle \approx \langle 1,0|\tilde{\zeta}_E|1,0\rangle$ , a small off-diagonal element  $\langle 0,0|\tilde{\zeta}_E|1,0\rangle$  is sufficient to couple the bound state with  $\{n, m\} = \{1, 0\}$  to the incoming wave, yielding an additional CIR. As far as bound states are concerned, solutions with  $E > E_0$  and  $m = 0$  leak into the open channel, and cannot be regarded as localized bound states. Hence, for  $|a_\mu/a| \gg 1$  and  $a < 0$ , there is only one bound state with zero angular momentum. In the opposite dimer limit, however, we encounter many dimer bound states.

#### 4.5.2 The case $\omega_1 \neq \omega_2$ : Relation to experiments

The case  $\omega_1 \neq \omega_2$  is relevant for experiments involving two different atom species trapped in magnetic or optical traps [115–117]. For instance, in optical traps the confining potential depends on the detuning  $\Delta = \omega_{\text{las}} - hc/\lambda$  of the laser frequency  $\omega_{\text{las}}$  from the characteristic frequency  $hc/\lambda$  associated with the optical transition  $ns \rightarrow np$ , and is therefore different for two different atom species. This conclusion also applies to magnetic traps if the atoms are confined in hyperfine states with different projection of the magnetic moment along the magnetic field. As a concrete



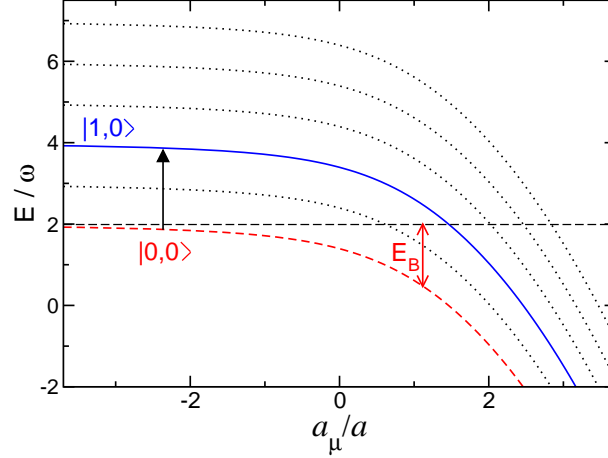


**Figure 4.1:** Bound state energies  $E$  as a function of  $a_\mu/a$  for harmonic confinement with equal frequency  $\omega$  for both atoms. The dashed red curve indicates the bound state energy of the ground-state  $|0,0\rangle$ . Its binding energy  $E_B$  is given by the distance to the horizontal dashed line indicating the continuum threshold for the open channel. The blue curve marks the bound state energy of the virtual bound state relevant for the low-energy scattering. It is obtained by a vertical shift of the ground-state energy by  $2\omega$ , and coincides with the three-fold degenerate bound-state energy indicated as solid curve. The black dotted curves give the bound-state energies of the excited transverse states, obtained by a vertical shift of the ground-state result.

example, let us consider a mixture of bosonic  $^{87}\text{Rb}$  atoms and fermionic  $^{40}\text{K}$  atoms. Sympathetic cooling has allowed to create an ultracold mixture of these two elements. By loading such a gas into a dipole trap and sweeping an external magnetic field, it has been possible [117] to identify three heteronuclear Feshbach resonances and to measure the 3D interspecies scattering length  $a = -14$  nm. It seems feasible to tune the magnetic field near a Feshbach resonance and to observe the interspecies CIR. It is hence very interesting to know how many of them can be expected and to study their locations.

The confining potential for a neutral atom in a standing optical wave  $\mathbf{E}(\mathbf{r}, t) = \mathbf{E}_0(\mathbf{r})\text{Re}[\exp(-i\omega_{\text{las}}t)]$  is  $V_{\text{conf}}(\mathbf{r}) = -(\varepsilon_0/4)\alpha'\mathbf{E}_0^2(\mathbf{r})$ , where  $\alpha' = -e^2/(2m_e\omega_{\text{las}}\varepsilon_0\Delta)$  is the real part of the polarizability [101]. Let us consider a red-detuned laser field corresponding to  $\Delta < 0$  and  $\alpha' > 0$ . In this configuration, the atoms are trapped around the maximum of the electric field. For a mixture of two species, each species experiences its own detuning  $\Delta_K$  ( $\Delta_{\text{Rb}}$ ) given by the two transition wavelengths  $\lambda_K = 767$  nm and  $\lambda_{\text{Rb}} = 780$  nm. Within a parabolic approximation for the potential around its minimum, the ratio  $\omega_K/\omega_{\text{Rb}}$  of trap frequencies for K

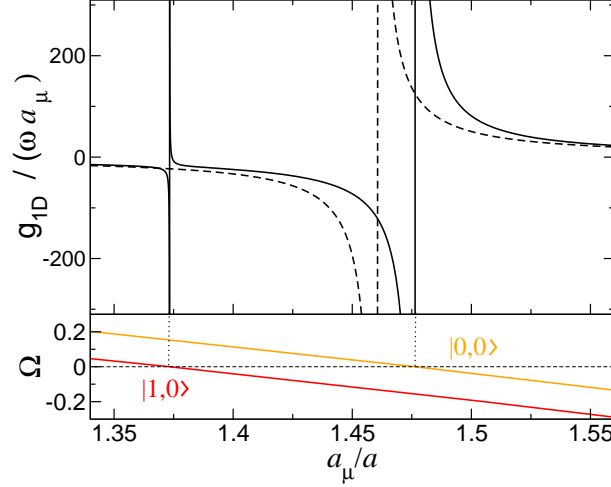


**Figure 4.2:** Upper viewgraph: CIR in the effective interspecies 1D interaction constant  $g_{1D}$  as a function of  $a_\mu/a$ . We consider a two-component atom gas of  $^{40}\text{K}$  and  $^{87}\text{Rb}$ , with average detuning  $\Delta = -0.1\omega_{\text{las}}$  (solid line). For comparison, we also show the result for the case when the two species experience the same trap frequency (dashed line). Lower viewgraph: Dimensionless binding energy  $\Omega$  for the two states  $|0,0\rangle$  and  $|1,0\rangle$ .

and Rb atoms becomes

$$\frac{\omega_K}{\omega_{\text{Rb}}} = \left( \frac{\Delta_{\text{Rb}}}{\Delta_K} \frac{m_{\text{Rb}}}{m_K} \right)^{1/2}. \quad (4.105)$$

Let us estimate this ratio for typical parameters. In order to suppress spontaneous emission, we assume an average detuning of  $\Delta = (\Delta_K + \Delta_{\text{Rb}})/2 = -0.1\omega_{\text{las}}$ , yielding  $\omega_{\text{las}} = 5hc(\lambda_K^{-1} + \lambda_{\text{Rb}}^{-1})/11$  and  $\Delta_{\text{Rb}}/\Delta_K = (5\lambda_K^{-1} - 6\lambda_{\text{Rb}}^{-1})/(5\lambda_{\text{Rb}}^{-1} - 6\lambda_K^{-1}) = 0.84$ . Taking also into account the mass ratio  $m_{\text{Rb}}/m_K = 87/40$ , we have  $\omega_K/\omega_{\text{Rb}} = 1.35$ , indicating a substantial coupling of COM and relative degrees of freedom.

Using Eq. (4.95), we can project the Green's function  $G_t(\mathbf{R}_\perp, 0; \mathbf{R}'_\perp, 0)$  on the appropriate basis defined in Eq. (4.65) and then compute numerically  $\tilde{\zeta}_E$  by performing the imaginary-time integration, see Appendix E. Then  $\tilde{\zeta}_{E_0}$  can be diagonalized, and the effective interspecies 1D interaction constant  $g_{1D}$  follows according to Eq. (4.80). The results are shown in the upper viewgraph of Fig. 4.2 in terms of the characteristic length  $a_\mu = \sqrt{2/(\mu(\omega_K + \omega_{\text{Rb}}))}$ . We find two resonances, indicating that the discussion of Sec. 4.5.1 applies to this particular case. In order to illustrate the interpretation of the CIR in terms of Feshbach-type resonances with bound states of the closed channels, we also plot in the lower viewgraph of Fig. 4.2 the dimensionless binding energy  $\Omega = 2(E - \omega_K + \omega_{\text{Rb}})/(\omega_K + \omega_{\text{Rb}})$  of the corresponding bound state. As expected, the resonances occur at those values of  $a_\mu/a$  for which the energy of the bound state of the closed channels coincides with the continuum threshold of the open channel.

## 4.6 Non-parabolic confining potentials

Describing the potential created by an optical or a magnetic guide as parabolic is to some extent a simplification which has to be verified. In fact, even though the lower-energy transverse states can rather well be approximated by the eigenfunctions of a 2D harmonic oscillator, in every real trap the confinement is to some degree non-parabolic. For resonant scattering, we expect to have a virtual occupation of many non-parabolic transverse states. As a consequence, the location of the CIR will be slightly moved, and new resonances could be created. This can already be seen from an analysis similar to the one in Sec. 4.5.1 for small non-parabolic corrections. In order to tackle the problem quantitatively, a full numerical treatment is required since no analytical expression for the Green's function is in general available, in contrast to Sec. 4.5.

As an example, we consider the small non-parabolicity due to the presence of a longitudinal magnetic bias field  $B_z$  in a magnetic waveguide containing a single-species gas. This is necessary to avoid Majorana spin flips [103] and the subsequent escape of atoms out of the trap. A magnetic trapping potential is formed according to  $V_{\text{conf}}(\mathbf{x}) = \mu_m |\mathbf{B}(\mathbf{x})|$ , where  $\mathbf{B}(\mathbf{x})$  is the applied magnetic field and  $\mu_m = m_F g_F \mu_B$ , with  $m_F$  being the magnetic quantum number of the atom in the hyperfine state  $|F, m_F\rangle$ ,  $g_F$  the Landé factor and  $\mu_B$  the Bohr magneton. Assuming that apart from the longitudinal bias field, the remaining magnetic fields create a parabolic and isotropic confinement in the transverse direction, the total confinement is given by

$$\chi V_{\text{conf}}(\mathbf{x}) = \sqrt{1 + 2\chi(x^2 + y^2)}, \quad (4.106)$$

where we have scaled energy in units of the parabolic trapping frequency  $\omega$  and length in units of  $a_\mu = (\mu\omega)^{-1/2}$ . The parameter  $\chi = \omega/(\mu_m B_z)$  is related to the Majorana spin flip rate  $\Gamma_{\text{loss}}$  [103]. The 1D effective interaction strength  $g_{1D}$  can be calculated following our general approach. We compute  $\tilde{\zeta}_{E_0}$  numerically as outlined in Appendix E. The results are shown in Fig. 4.3 for  $\chi = 0.067$ , which corresponds to  $\Gamma_{\text{loss}} = 10^{-6}\omega$ . We find two resonances reflecting the cylindrical symmetry of the potential (4.106) and the weakness of non-parabolic corrections. The degeneracy of the parabolic case (shown in Fig. 4.3) is lifted and the original CIR is split into two nearby resonances. As expected, the effect of the non-parabolic transverse states shows up only in the deep resonant region, making the parabolic solution a very good approximation away from the resonant region. In turn, this requires a good experimental resolution in order to observe the two CIR.

## 4.7 Conclusions

To conclude, we have presented the general solution for two-body s-wave scattering in a two-component ultracold atom gas longitudinally confined to one dimension by an arbitrary trapping potential. The underlying key property is that the center-of-mass and the relative degrees of freedom of the two-particle problem do not decouple,

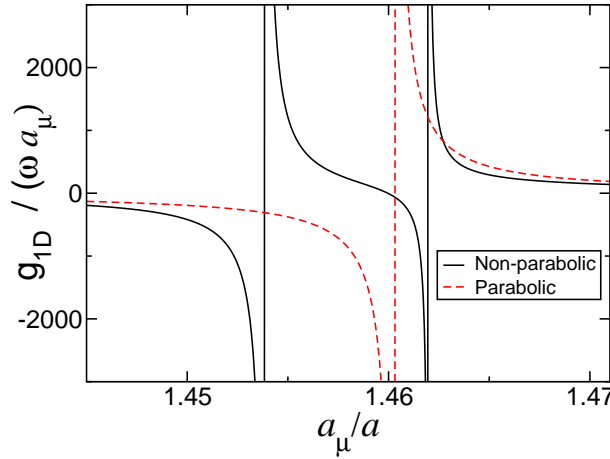


**Figure 4.3:** 1D effective interaction strength  $g_{1D}$  for the non-parabolic potential of Eq. (4.106) (black solid line) for  $\chi = 0.067$  corresponding to  $\Gamma_{\text{loss}} = 10^{-6}\omega$ . For comparison, the parabolic case is also shown (red dashed line).

as it is the case for a one-component gas and a pure parabolic confinement. Thus, no reduction to an effective single-particle problem is possible and the full coupled system has to be solved. In the framework of the pseudopotential approach, we derive the energy of the bound state when all transverse channels are closed. Simple analytical results were obtained in the limiting cases of the dimer as well as the BCS limit. Moreover, scattering solutions have been obtained when just one transverse channel is open. The effective 1D interaction constant  $g_{1D}$  can be calculated after diagonalizing a reduced Green's function. This can be achieved analytically for the special case of parabolic confinement, where the well-known confinement-induced resonance is recovered. For a two-component gas, as well as for a non-parabolic confinement, more than one CIR occur, which reflect the symmetry properties of the confining potential. These findings were illustrated by applying our formalism to experimentally relevant questions. We are confident that once the CIR has been verified experimentally, also the effects of a non-parabolic trapping potential will be discerned.

# 5

## Summary

In this thesis, the interplay of decoherence, nonlinear effects and driving is studied in different physical situations and contexts.

The first system is the Duffing oscillator in the deep quantum regime. Our approach is to start from a solution of the coherent problem thereafter including the dissipative effects by means of a Floquet Born-Markovian master equation. Both analytical and numerical calculations are presented, revealing a rich phenomenology. Most interestingly, we find that (i) in correspondence to the coherent multiphoton transitions, the dissipative system displays an out-of-phase resonant response or, alternatively, an in-phase antiresonant one. These two behaviors are the result of a complex interplay between tunnelling in an effective bistable quasipotential and dissipation. Moreover, (ii) the dynamical bistability determines a separation of time scales. This phenomenon is suppressed by the multiphoton resonances. Around these resonances, the oscillator can switch between two different configurations via multiphoton tunnelling transitions. As a consequence, peaks in the quantum relaxation rate result. The formalism developed in this context is generalized to the bichromatic driven dissipative nonlinear oscillator.

A further class of investigated systems consists of ultracold atoms in reduced dimensions in a nonlinear waveguide. Most importantly, we propose an experimentally viable setup for the realization of one-dimensional ultracold atom gases in a nanoscale magnetic waveguide formed by single doubly-clamped suspended carbon nanotubes. We show that all common decoherence and atom loss mechanisms are small guaranteeing a stable operation of the trap. Since the extremely large current densities in carbon nanotubes are spatially homogeneous, our proposed architecture allows to create a very regular non-parabolic trapping potential for the atom cloud. Adding a second nanowire allows to create a double-well potential with a moderate tunneling barrier which is desired for tunneling and interference experiments with the advantage of tunneling distances being in the nanometer regime.

Finally, we address and solve the two-particle s-wave scattering problem for ultracold atom gases confined in arbitrary quasi-one-dimensional trapping potentials, allowing for two different atom species. As a consequence, the center-of-mass and relative degrees of freedom do not factorize. We derive bound state solutions and obtain the general scattering solution, which exhibits several resonances in the 1D scattering length induced by the confinement. We apply our formalism to two experimentally relevant cases: (i) interspecies scattering in a two-species mixture, and (ii) the two-body problem for a single species in a non-parabolic trap.



# A Model for the driven suspended nanoresonator

In this Appendix, we show how one can derive from the model for a freely suspended nanomechanical beam the effective Hamiltonian for a single degree of freedom, given in Eq. (2.6), which is the focus of chapter 2.

For this, we consider a freely suspended nanomechanical beam of total length  $L$  and mass density  $\sigma = m/L$  which is clamped at both ends (*doubly clamped boundary conditions*) and which is characterized by its bending rigidity  $\mu = YI$  being the product of Young's elasticity modulus  $Y$  and the moment of inertia  $I$ . In addition, we allow for a mechanical force  $F_0 > 0$  which compresses the beam in longitudinal direction. Moreover, the beam is excited to transverse vibrations by a time-dependent driving field  $F(t) = f \cos(\omega_{\text{ext}} t)$ . In a classical description, the transverse deflection  $\phi(s, t)$  characterizes the beam completely, where  $0 \leq s \leq L$ . Then, the Lagrangian of the vibrating beam follows from elasticity theory as [68]

$$\mathcal{L}(\phi, \dot{\phi}, t) = \int_0^L ds \left[ \frac{\sigma}{2} \dot{\phi}^2 - \frac{\mu}{2} \frac{\phi'^2}{1 - \phi'^2} - F_0 \left( \sqrt{1 - \phi'^2} - 1 \right) + F(t) \phi \right]. \quad (\text{A.1})$$

Before we study the dynamics of the driven beam, we consider first the undriven system with  $F(t) \equiv 0$ .

For the case of small deflections  $|\phi'(s)| \ll 1$ , the Lagrangian can be linearized and the time-dependent Euler-Lagrange equations can be solved by the eigenfunctions  $\phi(s, t) = \sum_n \phi_n(s, t) = \sum_n \mathcal{A}_n(t) g_n(s)$ , where  $g_n(s)$  are the normal modes which follow as the solution of the characteristic equation. For the doubly clamped nano-beam, we have  $\phi(0) = \phi(L) = 0$  and  $\phi'(0) = \phi'(L) = 0$ . However, it turns out that this situation is closely related to the simpler case that the nano-beam is also fixed at both ends but its ends can move such that the bending moments at the ends vanish, i.e.,  $\phi(0) = \phi(L) = 0$  and  $\phi''(0) = \phi''(L) = 0$  (*free boundary conditions*). For the case of free boundary conditions, the characteristic equation yields the normal modes  $g_n^{\text{free}}(s) = \sin(n\pi s/L)$  and the corresponding frequency of the  $n$ -th mode follows as

$$\omega_n^{\text{free}} = \left( \frac{\mu(n\pi/L)^2 - F_0}{\sigma} \right)^{1/2} \frac{n\pi}{L}. \quad (\text{A.2})$$

At the critical force  $F_c = \mu(\pi/L)^2$ , the fundamental frequency  $\omega_1^{\text{free}}(F_0 \rightarrow F_c)$  vanishes as  $\sqrt{\epsilon}$ , where  $\epsilon = (F_c - F_0)/F_c$  is the distance to the critical force, and the well-known Euler instability occurs.

For the case of doubly clamped boundary conditions, the characteristic equation yields a transcendental equation for the normal modes which cannot be solved analytically. However, close to the Euler instability  $F_0 \rightarrow F_c$ , the situation simplifies again. After expanding, one finds for the fundamental frequency

$\omega_1(F_0 \rightarrow F_c) = \sqrt{\epsilon}\omega_0$ , with the frequency scale  $\omega_0 = (4/\sqrt{3})\sqrt{\mu/\sigma}(\pi/L)^2$ . Approaching the Euler instability, the frequencies of the higher modes  $\omega_{n \geq 2}$  remain finite, while the fundamental frequency  $\omega_1(F_0 \rightarrow F_c)$  vanishes again like  $\sqrt{\epsilon}$ . Hence, the dynamics at low energies close to the Euler instability will be dominated by the fundamental mode alone which simplifies the treatment of the nonlinear case, see below. The fundamental mode  $g_1(s)$  can also be expanded close to the Euler instability and one obtains in zero-th order in  $\epsilon$

$$g_1(s) \simeq \sin^2\left(\frac{\pi s}{L}\right). \quad (\text{A.3})$$

Since the fundamental mode vanishes when  $F_0 \rightarrow F_c$ , one has to include the contributions beyond the quadratic terms  $\propto \phi'^2, \phi''^2$  of the transverse deflections in the Lagrangian. The next higher order is quartic and yields terms  $\propto \phi'^4, \phi'^2\phi''^2$ . Inserting again the normal mode expansion in the Lagrangian generates self-coupled modes  $\sum_k \mathcal{A}_k^4$  as well as couplings terms  $\sum_{k,l} \mathcal{A}_k^2 \mathcal{A}_l^2$  between the modes. This interacting field-theoretic problem cannot be solved any longer. However, since the normal mode dominates the dynamics at low energies closed to the Euler instability, one can neglect the higher modes in this regime. Hence, we choose the ansatz  $\phi(s, t) = \mathcal{A}_1(t)g_1(s)$  in the regime  $F_0 \rightarrow F_c$  and restrict the discussion in the rest of our work to this regime. The so-far classical field theory can be quantized by introducing the canonically conjugate momentum  $\mathcal{P} \equiv -i\hbar\partial/\partial\mathcal{A}_1$  and the time-dependent driving force can straightforwardly be included. Note that when the driving frequency is close to the fundamental frequency of the beam, the fundamental mode will dominate also in absence of a static longitudinal compression force. However, a compression force helps to enhance the nonlinear effect which are in the focus of this work. After all, an effective quantum mechanical time-dependent Hamiltonian results which describes the dynamics of a single quantum particle with “coordinate”  $\mathcal{X} \equiv \mathcal{A}_1$  in a time-dependent anharmonic potential. It reads

$$H(t) = \frac{\mathcal{P}^2}{2m_{\text{eff}}} + \frac{m_{\text{eff}}\omega_1^2}{2}\mathcal{X}^2 + \frac{\alpha}{4}\mathcal{X}^4 + \mathcal{X}F(t) \quad (\text{A.4})$$

with the effective mass  $m_{\text{eff}} = 3\sigma L/8$  and the nonlinearity parameter  $\alpha = (\pi/L)^4 F_c L(1 + 3\epsilon)$ .



# B Van Vleck perturbation theory

This Appendix has a double purpose: on one hand, to briefly introduce the perturbative Van Vleck formalism for quasidegenerate Hamiltonians, and, on the other hand, to outline the derivation of the effective Hamiltonian in Eq. (2.22).

In the literature, several different formulations of the Van Vleck formalism are available. In this Appendix, we follow the approach of Ref. [75]. Here, a single set of quasidegenerate eigenvalues is considered. The corresponding unperturbed eigenvectors define the model space  $\mathcal{H}_M$ . The Hilbert space is divided into the model space and its orthogonal space  $\mathcal{H}_M \oplus \mathcal{H}_M^\perp$ . A transformation is then defined, which transforms the Hamiltonian into a two-block diagonal form. An alternative approach would be to consider several sets of quasidegenerate eigenvalues, thereby obtaining a many-block diagonal effective Hamiltonian [74]. However, the former approach leads to much more compact formulae when high order corrections are considered. Moreover, it implies no loss of generality. In fact, when many sets of quasidegenerate eigenvalues are present, one can focus on one set only at a time, thereby computing the different blocks of the effective Hamiltonian one after the other.

In the present context the model space is defined by a pair of harmonic oscillator states:  $\mathcal{H}_M = |n\rangle \oplus |N-n\rangle$ . Any operator  $A$  can be partitioned into a block diagonal part  $A_D$  and a block off-diagonal part  $A_X$

$$A = A_D + A_X, \quad A_D = PAP + QAQ, \quad A_X = PAQ + QAP. \quad (\text{B.1})$$

Here,  $P$  and  $Q$  are the projectors onto  $\mathcal{H}_M$  and  $\mathcal{H}_M^\perp$  respectively. For a product of two operators we have

$$(AB)_D = A_D B_D + A_X B_X, \quad (AB)_X = A_X B_D + A_D B_X \quad (\text{B.2})$$

The effective Hamiltonian can be written as

$$H' = e^{iS} H e^{-iS}, \quad (\text{B.3})$$

where  $S$  is an hermitian matrix and its block diagonal part vanish  $S_D = 0$ . We can then use the Baker-Campbell-Hausdorff formula in Eq. (B.3) which reads

$$H' = H + [iS, H] + \frac{1}{2!}[iS, [iS, H]] + \dots, \quad (\text{B.4})$$

substitute the expansions  $S = \sum_{n=1}^{\infty} \varepsilon^n S_n$  and  $H' = H_0 + \sum_{n=1}^{\infty} \varepsilon^n H'_n$  and compute order by order  $H'$  and  $S$ . At first order, we have

$$[iS_1, H_0] = -V_X \quad (\text{B.5})$$

and

$$H'_1 = V_D \quad (\text{B.6})$$

for the block diagonal and the block off-diagonal parts, respectively. Here, by using  $S_D = 0$ , we get

$$\langle \alpha | S_1 | \beta \rangle = -i \frac{\langle \alpha | V | \beta \rangle}{E_\alpha - E_\beta} \quad (\text{B.7})$$

for  $\alpha$  and  $\beta$  belonging to different subspaces,  $\langle \alpha | S_1 | \beta \rangle = 0$  otherwise, and

$$H'_1 = PVP + QPQ. \quad (\text{B.8})$$

To second order, we have

$$\langle \alpha_1 | H'_2 | \alpha_2 \rangle = \frac{\varepsilon^2}{2} \sum_{\beta} \left( \frac{1}{E_{\alpha_1} - E_{\beta}} + \frac{1}{E_{\alpha_2} - E_{\beta}} \right) \langle \alpha_1 | V | \beta \rangle \langle \beta | V | \alpha_2 \rangle, \quad (\text{B.9})$$

with  $|\alpha_1\rangle, |\alpha_2\rangle \in \mathcal{H}_{\mathcal{M}}$ ,  $|\beta\rangle \in \mathcal{H}_{\mathcal{M}}^\perp$ .

In general, higher order corrections are rather cumbersome [75]. However, the situation simplifies once one observes that finite corrections to the diagonal elements of order  $\varepsilon^m$  to the effective  $2 \times 2$  Hamiltonian matrix would yield only a resonance shift of the same order. Hence, at the true resonant frequency, the only finite contributions to the effective Hamiltonian are the off-diagonal one  $\langle n | H'_m | N - n \rangle$ . With this simplification in mind, one can straightforwardly check that the lowest order correction is

$$\langle n | H'_n | N - n \rangle = \varepsilon^{N-2n} \langle n | V | n+1 \rangle \prod_{i=1}^{N-2n-1} \frac{\langle n+i | V | n+i+1 \rangle}{E_n - E_{n+i}}. \quad (\text{B.10})$$

with  $E_i$  being the eigenvalues of  $H_0$ . By plugging into the above equation

$$E_n - E_{n+i} = \frac{\nu}{2} i(N - 2n - i), \quad (\text{B.11})$$

$$\langle n+i | V | n+i+1 \rangle = \frac{\nu(N+1)}{2} \sqrt{n+i+1}, \quad (\text{B.12})$$

we get the same off-diagonal elements as in the Hamiltonian matrix in Eq. (2.22).

# C A Floquet master equation for a bichromatically driven system

In this Appendix, we derive a master equation describing a bichromatically driven anharmonic oscillator coupled to a smooth thermal bath by combining the RWA together with Floquet theory.

We first consider the isolated system; its coherent dynamics is governed by the Hamiltonian

$$H_S = \frac{\mathcal{P}^2}{2m} + \frac{1}{2}\omega^2\mathcal{X}^2 + \frac{\alpha}{4}\mathcal{X}^4 + f_1\mathcal{X}\cos(\omega_1t) + f_2\mathcal{X}\cos(\omega_2t + \theta). \quad (\text{C.1})$$

For weak anharmonicity  $\alpha \ll \omega$ , weak driving  $f_{1,2} \ll \alpha$  and a small detuning from the characteristic frequency of the anharmonic oscillator  $|\omega_{1,2} - \omega| \ll \omega$ , a RWA is meaningful. As usual, we switch to the rotating frame by means of the canonical transformation  $R = \exp[i\Omega_1 a^\dagger at]$ . Then, we disregard all the fast oscillating terms from the transformed Hamiltonian. This yields the Schrödinger equation

$$\left[-i\frac{d}{dt} + \tilde{H}(t)\right]|\tilde{\psi}_\alpha(t)\rangle = 0, \quad (\text{C.2})$$

with the RWA Hamiltonian

$$\tilde{H}(t) = \tilde{\omega}\hat{n} + \frac{\nu}{2}\hat{n}(\hat{n} + 1) + \mu_1(a + a^\dagger) + \mu_2(ae^{i(\delta t + \theta)} + a^\dagger e^{-i(\delta t + \theta)}). \quad (\text{C.3})$$

Here, we have introduced the detunings  $\tilde{\omega} = \omega - \omega_1$  and  $\delta = \omega_2 - \omega_1$ , the driving strengths  $\mu_{1/2} = (x_0/2^{3/2})f_{1/2}$  and the nonlinearity parameter  $\nu = 3\hbar\alpha/(4\omega_1^2)$ . Within this approximation, the Hamiltonian in the rotating frame  $\tilde{H}(t)$  is time-periodic with period  $T_\delta = 2\pi/\delta$ . We can thus use the Floquet theory, introduced in Section 2.3.1, to compute the solutions of the Schrödinger equation in the rotating frame.

The Floquet theorem, given in Eq. (2.7), assures us that the solutions in the rotating frame have the form

$$|\tilde{\psi}_\alpha(t)\rangle = e^{-i\varepsilon_\alpha t}|\phi_\alpha(t)\rangle$$

where  $|\phi_\alpha(t)\rangle$  is a set of  $T_\delta$ -periodic states solving the eigenvalue problem in Eq. (2.8) with  $\tilde{H}(t)$  instead of  $H_S(t)$ . From the Floquet states  $|\phi_\alpha(t)\rangle$ , we can extract a set of equal times orthonormal (approximate) solutions of the original problem by transforming back to the static frame

$$|\psi_\alpha(t)\rangle = e^{-i\varepsilon_\alpha t}e^{-i\omega_1 a^\dagger at}|\phi_\alpha(t)\rangle. \quad (\text{C.4})$$

We can now include the weak coupling to a smooth thermal bath and proceed in the derivation of the master equation. Since this derivation is analogous to the one for monochromatic driving detailed in Section 2.4.3, we will be more sketchy here.

We select all the Floquet solutions  $\{|\phi_\alpha(t)\rangle\}$  from a single Brillouin zone. We perform a transformation to the static frame, thereby obtaining the complete set  $\{e^{-i\omega_1 a^\dagger at}|\phi_\alpha(t)\rangle\}$  in the static frame. We then project the density matrix onto this set, such that the matrix elements read

$$\varrho_{\alpha\beta}(t) = \langle\phi_\alpha(t)|e^{i\omega_1 a^\dagger at}\varrho(t)e^{-i\omega_1 a^\dagger at}|\phi_\beta(t)\rangle. \quad (\text{C.5})$$

Performing the derivative one obtains

$$\dot{\varrho}_{\alpha\beta}(t) = -i(\varepsilon_\alpha - \varepsilon_\beta)\varrho_{\alpha\beta}(t) + \langle\phi_\alpha(t)|e^{i\omega_1 a^\dagger at}\mathcal{L}\varrho e^{-i\omega_1 a^\dagger at}|\phi_\beta(t)\rangle. \quad (\text{C.6})$$

For the dissipative term, we need to compute

$$\begin{aligned} X_{\alpha\beta}(t) &= \langle\phi_\alpha(t)|e^{i\omega_1 a^\dagger at}\mathcal{X}e^{-i\omega_1 a^\dagger at}|\phi_\beta(t)\rangle \\ &= \frac{x_0}{\sqrt{2}}e^{-i\omega_1 t}\langle\phi_\alpha(t)|a|\phi_\beta(t)\rangle + \frac{x_0}{\sqrt{2}}e^{i\omega_1 t}\langle\phi_\alpha(t)|a^\dagger|\phi_\beta(t)\rangle \\ &= \frac{x_0}{\sqrt{2}}e^{-i\omega_1 t}\sum_n e^{-in\delta t}A_{\alpha\beta,n} + \frac{x_0}{\sqrt{2}}e^{i\omega_1 t}\sum_n e^{-in\delta t}A_{\beta\alpha,-n}^*, \end{aligned} \quad (\text{C.7})$$

The Fourier transform of the mean value of the destruction operator  $A_{\alpha\beta,n}$  can be expressed in terms of the Fourier transform of the Floquet states as

$$A_{\alpha\beta,n} = \sum_j \langle\hat{\phi}_{\alpha j}|a|\hat{\phi}_{\beta j+n}\rangle. \quad (\text{C.8})$$

We can now compute the matrix elements of the operators involved in the dissipative part in Eq. (C.6) and find for the terms in Eq. (2.61)

$$(P+Q)_{\alpha\beta} = \frac{x_0}{\sqrt{2}}\sum_n (e^{-i\omega_1 t}e^{-in\delta t}N_{\alpha\beta,-n}^- A_{\alpha\beta,n} + e^{i\omega_1 t}e^{-in\delta t}N_{\alpha\beta,-n}^+ A_{\beta\alpha,-n}^*) \quad (\text{C.9})$$

and

$$(P-Q)_{\alpha\beta} = -\frac{x_0}{\sqrt{2}}\sum_n (e^{-i\omega_1 t}e^{-in\delta t}N_{\alpha\beta,n}^+ A_{\alpha\beta,n} + e^{i\omega_1 t}e^{-in\delta t}N_{\alpha\beta,n}^- A_{\beta\alpha,-n}^*). \quad (\text{C.10})$$

Here,  $N_{\alpha\beta,n}^\pm$  are defined as

$$N_{\alpha\beta,n}^\pm = N(\varepsilon_\alpha - \varepsilon_\beta \pm \omega_1 + n\delta) \quad N(\varepsilon) = J(|\varepsilon|)[n_{th}(|\varepsilon|) + \Theta(-\varepsilon)], \quad (\text{C.11})$$

in terms of the bath density of states  $J(|\varepsilon|)$  and the bosonic thermal occupation number  $n_{th}(|\varepsilon|)$ .

As discussed in Section 2.3.1,  $N(\varepsilon)$  diverges for  $s < 1$  at low energies indicating that the perturbative approach adopted here is not appropriate for sub-Ohmic but only for (super-)Ohmic baths. Moreover, in the calculation, we have neglected the quasienergy Lamb shifts, whose order of magnitude is  $\gamma_s$ .

We have now the matrix elements in the RWA Floquet basis for all the operators appearing in the Markovian master equation. We avoid writing down its complete

expression because it would be too cumbersome. Instead, we perform a moderate rotating-wave approximation consisting in averaging the time-dependent terms in the bath part over the driving period  $T_\delta$ . In this way, we obtain

$$\dot{\varrho}_{\alpha\beta}(t) = \sum_{\alpha'\beta'} [-i(\varepsilon_\alpha - \varepsilon_\beta)\delta_{\alpha\alpha'}\delta_{\beta\beta'} + \mathcal{L}_{\alpha\beta,\alpha'\beta'}] \varrho_{\alpha'\beta'}(t), \quad (\text{C.12})$$

with the dissipative transition rates

$$\begin{aligned} \mathcal{L}_{\alpha\beta,\alpha'\beta'} = & \frac{x_0^2}{2} \sum_n (N_{\alpha\alpha',-n}^- + N_{\beta\beta',-n}^-) A_{\alpha\alpha',n} A_{\beta\beta',n}^* + (N_{\beta\beta',n}^+ + N_{\alpha\alpha',n}^+) A_{\alpha'\alpha,n}^* A_{\beta'\beta,n} \\ & - \delta_{\alpha\alpha'} \frac{x_0^2}{2} \sum_{n\alpha''} N_{\alpha''\beta',n}^+ A_{\beta'\alpha'',n} A_{\beta\alpha'',n}^* + N_{\alpha''\beta',-n}^- A_{\alpha''\beta',n}^* A_{\alpha''\beta,n} \\ & - \delta_{\beta\beta'} \frac{x_0^2}{2} \sum_{n\beta''} N_{\beta''\alpha',n}^+ A_{\alpha,\beta'',n} A_{\alpha'\beta'',n}^* + N_{\beta''\alpha',-n}^- A_{\beta''\alpha,n}^* A_{\beta''\alpha',n}. \end{aligned} \quad (\text{C.13})$$

A discussion about the validity of the rotating-wave approximation in the context of this master equation for bichromatically driven systems would change very little with respect to the one at the end of Section 2.4.3 for monochromatically driven systems.

In that case, we have concluded that this approximation is reliable provided that one defines carefully the borders of the Brillouin zone and that its width, given by the driving frequency  $\omega_{\text{ex}}$ , is much smaller than the coupling to the bath  $\gamma_s$ . The latter condition sets the limits of validity for the Markovian approximation as well. Hence in that context, the rotating-wave approximation is not more restrictive than the ordinary Markovian approximation.

In the actual context, the width of the Brillouin zone is given by the difference  $\delta$  between the two driving frequencies. The limit of validity of the rotating-wave approximation is thus set by the condition  $\gamma_s \ll \delta$ , which is more restrictive than the condition  $\gamma_s \ll \omega_1, \omega_2$  for the ordinary Markovian approximation.

Let us now check that, in the limit  $f_2 \rightarrow 0$ , we correctly recover the RWA master equation derived in Section 2.4.4. For  $f_2 = 0$ , the Floquet solutions  $\{|\phi_\alpha\rangle\}$  are time independent. As a consequence, only those matrix elements are finite, whose Fourier index is zero. Moreover, we can identify the matrix elements  $X_{\alpha\beta,1} = x_0/(\sqrt{2})A_{\alpha\beta,0}$ ,  $X_{\alpha\beta,-1} = x_0/(\sqrt{2})A_{\beta\alpha,0}^*$  and  $N_{\alpha\beta,\pm 1} = N_{\alpha\beta,0}^\pm$ . Keeping this in mind, direct comparison shows that, in this limit, the dissipative transition rates in Eqs. (2.83) and (C.13) coincide.



# D Pseudopotential method for the two-body problem in free space

In this Appendix, we want to show that to model the interaction with the Fermi pseudopotential, given in Eq. (4.35), leads to the scattering amplitude and the binding energy for the shallow bound state given in Eqs. (4.34) and (4.33), respectively.

The pseudopotential is enforced by requiring the boundary condition as  $r \rightarrow 0$ :

$$\psi(\mathbf{r} \rightarrow 0) \simeq \frac{f}{4\pi r}(1 - r/a), \quad (\text{D.1})$$

leading to the inhomogeneous Schrödinger equation

$$\left(-\frac{1}{2\mu}\Delta - E\right)\psi(\mathbf{r}) = \frac{f}{2\mu}\delta(\mathbf{r}) \quad (\text{D.2})$$

The outgoing (retarded) solutions are given by

$$\psi(\mathbf{r}) = \psi_0(\mathbf{r}) + \int d\mathbf{r}' G_E(\mathbf{r}, \mathbf{r}') (f/2\mu)\delta(\mathbf{r}') = \psi_0(\mathbf{r}) + \frac{f}{2\mu}G_E(\mathbf{r}, 0), \quad (\text{D.3})$$

where  $\psi_0$  is a solution to the homogeneous ( $f = 0$ ) problem, and the two-body Green's function admits the integral representation

$$G_E(\mathbf{r}, \mathbf{r}') = \int \frac{d^3\mathbf{k}}{(2\pi)^3} \frac{e^{i\mathbf{k}' \cdot (\mathbf{r} - \mathbf{r}')}}{k'^2 - E - i0^+} \quad (\text{D.4})$$

with  $k = \sqrt{2\mu E}$ . Now we must enforce the boundary condition (D.1), which gives from (D.3) the equation

$$\psi_0(0) + \frac{f}{2\mu} \left( G_E(\mathbf{r}, 0) - \frac{\mu}{2\pi r} \right)_{r \rightarrow 0} = -\frac{f}{4\pi a}. \quad (\text{D.5})$$

For  $E > 0$ ,  $\psi_0(\mathbf{r})$  is the incoming wave  $e^{ikz}$ . Moreover Eq. (D.4) yields

$$G_E(\mathbf{r}, 0) = \frac{\mu}{2\pi r} e^{ikr}. \quad (\text{D.6})$$

Hence, we immediately get from Eq. (D.5)

$$f(k) = -\frac{4\pi a}{1 + ika}, \quad (\text{D.7})$$

corresponding to the scattering solution

$$\psi(\mathbf{r}) = e^{ikz} + \frac{f(k)}{4\pi r} e^{ikr}. \quad (\text{D.8})$$

We can thus identify  $f_e(k)$  with  $f(k)/(4\pi)$ , thereby recovering the expected result Eq. (4.34).

For a bound state,  $E < 0$ , we need to choose  $\psi_0 = 0$  and  $f$  drops out from Eq. (D.5). Moreover Eq. (D.4) yields

$$G_E(\mathbf{r}, 0) = \frac{\mu}{2\pi r} \exp\left(-\sqrt{-2\mu E}r\right). \quad (\text{D.9})$$

By plugging into Eq. (D.5), we get

$$a^{-1} = \sqrt{-2\mu E}. \quad (\text{D.10})$$

This boundary condition can be regarded as an equation for the binding energy of the pseudopotential bound states in terms of the scattering length  $a$ . There is just one bound state for any positive value of the scattering length. As expected, its binding energy is equal to the one of a shallow bound state for an arbitrary potential given in Eq. (4.33).



# E Short time Green's function and the operators $\zeta_E$ and $\tilde{\zeta}_E$

This appendix is divided into two sections. In the first section we derive the short-time expansion of the Tokatly Green's function. In the second section, we detail the evaluation of the operators  $\zeta_E$  and  $\tilde{\zeta}_E$  for the inter-species scattering in a parabolic confinement, and for the more general case of a non-parabolic confinement.

## E.1 Short-time expansion of the Tokatly Green's function

In this section, we illustrate how to expand the Green's function

$$G_t(\mathbf{X}; \mathbf{X}') = \langle \mathbf{X} | \exp [-(K(\mathbf{\Pi}) + U(\mathbf{X}))t] | \mathbf{X}' \rangle \quad (\text{E.1})$$

with respect to  $t$  yielding the expression in Eq. (4.57) for  $G_t(\mathbf{R}_\perp, 0; \mathbf{R}'_\perp, 0)$ . In order to simplify the notation, we have introduced the five-dimensional vectors  $\mathbf{X} = \{\mathbf{R}_\perp, \mathbf{r}\}$  and  $\mathbf{\Pi} = \{\mathbf{P}_\perp, \mathbf{p}\}$  and the functions  $K(\mathbf{\Pi}) = \mathbf{P}_\perp^2/2M + \mathbf{p}^2/2\mu$  and  $U(\mathbf{X}) = V_1(\mathbf{R}_\perp + \mu\mathbf{r}_\perp/m_1) + V_2(\mathbf{R}_\perp - \mu\mathbf{r}_\perp/m_2)$  for the kinetic and the potential energy, respectively. First, we expand the Green's function around the free solution given by

$$\langle \mathbf{X} | \exp [-K(\mathbf{\Pi})t] | \mathbf{X}' \rangle = \frac{M}{2\pi t} \exp \left[ -\frac{(\mathbf{R}_\perp - \mathbf{R}'_\perp)^2 M}{2t} \right] \left( \frac{\mu}{2\pi t} \right)^{3/2} \exp \left[ -\frac{(\mathbf{r} - \mathbf{r}')^2 \mu}{2t} \right]. \quad (\text{E.2})$$

In order to justify such an expansion, note that for  $t \rightarrow 0^+$

$$\langle \mathbf{X} | K(\mathbf{\Pi}) \exp [-K(\mathbf{\Pi})t] | \mathbf{X}' \rangle = -\frac{d}{dt} \langle \mathbf{X} | \exp [-K(\mathbf{\Pi})t] | \mathbf{X}' \rangle \propto \delta(\mathbf{X} - \mathbf{X}') \frac{1}{t}, \quad (\text{E.3})$$

whereas

$$\langle \mathbf{X} | U(\mathbf{X}) \exp [-K(\mathbf{\Pi})t] | \mathbf{X}' \rangle = U(\mathbf{X}) \langle \mathbf{X} | \exp [-K(\mathbf{\Pi})t] | \mathbf{X}' \rangle \propto U(\mathbf{X}) \delta(\mathbf{X} - \mathbf{X}'). \quad (\text{E.4})$$

Since the kinetic energy in Eq. (E.3) diverges whereas the potential energy in Eq. (E.4) remains finite, the latter can be regarded as a small perturbation. This expansion yields

$$G_t(\mathbf{X}; \mathbf{X}') \simeq (1 - tU(\mathbf{X})) \langle \mathbf{X} | \exp [-K(\mathbf{\Pi})t] | \mathbf{X}' \rangle. \quad (\text{E.5})$$

Let us now set  $\mathbf{X}_0 = \{\mathbf{R}'_{\perp}, 0\}$  in Eq. (E.2) and expand with respect to  $t$ :

$$\begin{aligned}
& \langle \mathbf{R}_{\perp}, 0 | \exp[-K(\mathbf{\Pi})t] | \mathbf{R}'_{\perp}, 0 \rangle \\
&= \left( \frac{\mu}{2\pi t} \right)^{3/2} \frac{M}{2\pi t} \exp \left[ -\frac{(\mathbf{R}_{\perp} - \mathbf{R}'_{\perp})^2 M}{2t} \right] \\
&= \left( \frac{\mu}{2\pi t} \right)^{3/2} \int \frac{d^2 \mathbf{P}_{\perp}}{(2\pi)^2} \exp \left[ i \mathbf{P}_{\perp} \cdot (\mathbf{R}_{\perp} - \mathbf{R}'_{\perp}) - \frac{\mathbf{P}_{\perp}^2}{2M} t \right] \\
&\simeq \left( \frac{\mu}{2\pi t} \right)^{3/2} \int \frac{d^2 \mathbf{P}_{\perp}}{(2\pi)^2} \left( 1 - \frac{\mathbf{P}_{\perp}^2}{2M} t \right) \exp \left[ i \mathbf{P}_{\perp} \cdot (\mathbf{R}_{\perp} - \mathbf{R}'_{\perp}) \right] \\
&= \left( \frac{\mu}{2\pi t} \right)^{3/2} \left( \delta(\mathbf{R}_{\perp} - \mathbf{R}'_{\perp}) - t \frac{\mathbf{P}_{\perp}^2}{2M} \right). \tag{E.6}
\end{aligned}$$

In the last line, the operator  $\mathbf{P}_{\perp}^2$  stands for  $(2\pi)^{-2} \int d^2 \mathbf{P}_{\perp} \langle \mathbf{R}_{\perp} | \mathbf{P}_{\perp} \rangle \mathbf{P}_{\perp}^2 \langle \mathbf{P}_{\perp} | \mathbf{R}'_{\perp} \rangle$ . Inserting  $\mathbf{X}_0$  into Eq. (E.5), we finally obtain Eq. (4.57).

## E.2 Evaluation of the operators $\zeta_E$ and $\tilde{\zeta}_E$

In this section, we outline the evaluation of the kernels  $\zeta_E$  and  $\tilde{\zeta}_E$  given in Eqs. (4.56) and (4.64), respectively.

### Parabolic confinement, $\omega_1 \neq \omega_2$

First, let us consider the special case of parabolic confinement, but the two species may experience different trap frequencies. For this confinement, the Green's function  $G_t(\mathbf{R}_{\perp}, 0; \mathbf{R}'_{\perp}, 0)$  is given in Eq. (4.95). The first step is to project this operator onto the appropriate orthonormal basis  $\{|j\rangle\}$  defined in Eq. (4.65). Note that this definition allows an arbitrary choice of the basis, apart from properly fixing the vector  $|0\rangle$ . One possibility is introduced in Eq. (4.93). This is a natural option because it reflects the cylindrical symmetry of the problem. However, this choice would not permit further analytical progress. For this reason, we employ an alternative basis defined by

$$\langle \mathbf{R}_{\perp} | j \rangle = \langle \mathbf{R}_{\perp} | n_x, n_y \rangle = \frac{1}{a_M} \psi_{n_x} \left( \frac{x}{a_M} \right) \psi_{n_y} \left( \frac{y}{a_M} \right), \tag{E.7}$$

where  $\psi_n(x)$  is the eigenfunction for the 1D oscillator in dimensionless units,  $\psi_n(x) = (\sqrt{\pi} 2^{n_x} n!)^{-1/2} \exp(-x^2/2) H_n(x)$ , with  $H_n(x)$  being Hermite polynomials. Note that the  $x$  and  $y$  directions factorize in the Green's function (4.95), allowing to perform the  $x$  and  $y$  integrals separately. For convenience, we introduce dimensionless coordinates  $x \rightarrow x/a_M$  and find

$$\begin{aligned}
[G(t)]_{\mathbf{n}, \mathbf{m}} &= \langle n_x, n_y | G_t(\mathbf{R}_{\perp}, 0; \mathbf{R}'_{\perp}, 0) | m_x, m_y \rangle \\
&= \sqrt{\frac{\mu}{2\pi t}} \frac{\beta(1-\beta)}{\pi^2 a_M^2} \frac{e^{-\omega_1 t}}{1 - e^{-2\omega_1 t}} \frac{e^{-\omega_2 t}}{1 - e^{-2\omega_2 t}} [F(t)]_{n_x, m_x} [F(t)]_{n_y, m_y} \tag{E.8}
\end{aligned}$$

with

$$[F(t)]_{n,m} = \int dx dx' \bar{\psi}_n(x) \exp \left[ -\frac{x^2 + x'^2}{2} f(t) + xx' g(t) \right] \psi_m(x'). \quad (\text{E.9})$$

The functions  $f(t)$  and  $g(t)$  are defined in Eq. (4.96). We perform the first integration by using the identity [114]

$$\int dz e^{-(z-z')^2} H_n(\alpha z) = \pi^{1/2} (1 - \alpha^2)^{n/2} H_n \left( \frac{\alpha z'}{(1 - \alpha^2)^{1/2}} \right), \quad (\text{E.10})$$

with  $\alpha = \alpha(t) = [(1 + f(t))/2]^{-1/2}$ ,  $z = x/\alpha(t)$  and  $z' = g(t)\alpha(t)x'/2$ , yielding

$$\begin{aligned} [F(t)]_{n,m} &= (2^{n+m} m! n!)^{-1/2} \alpha(t) (1 - \alpha(t)^2)^{n/2} \\ &\times \int dx' \exp \left[ -x'^2 \left( \alpha^{-2}(t) - \frac{g(t)\alpha^2(t)}{4} \right) \right] H_n \left( \frac{g(t)\alpha^2(t)}{2(1 - \alpha^2(t))^{1/2}} x' \right) H_m(x'). \end{aligned} \quad (\text{E.11})$$

By substituting Eq. (E.8) together with Eq. (E.11) into  $\zeta_E$  defined in Eq. (4.56), and by introducing the dimensionless time  $t' = \sqrt{t(\omega_1 + \omega_2)}$ , we get

$$\begin{aligned} [\zeta_E]_{\mathbf{n},\mathbf{m}} &= \frac{1}{4\pi a_\mu} \int_0^\infty dt' \left\{ A h_E(t') \left[ F \left( \frac{t'^2}{\omega_1 + \omega_2} \right) \right]_{m_x, n_x} \right. \\ &\quad \times \left[ F \left( \frac{t'^2}{\omega_1 + \omega_2} \right) \right]_{m_y, n_y} - \frac{2}{\pi^{1/2} t'^2} \delta_{\mathbf{n},\mathbf{m}} \left. \right\}, \end{aligned} \quad (\text{E.12})$$

with the dimensionless parameter  $A = 2\pi^{-3/2} \beta (1 - \beta) a_\mu^2 / a_M^2$  and

$$\begin{aligned} h_E(t') &= \exp \left[ -\frac{(\omega_1 + \omega_2 - E)t'^2}{\omega_1 + \omega_2} \right] \left( 1 - \exp \left[ -\frac{2\omega_1 t'^2}{\omega_1 + \omega_2} \right] \right)^{-1} \\ &\quad \times \left( 1 - \exp \left[ -\frac{2\omega_2 t'^2}{\omega_1 + \omega_2} \right] \right)^{-1}. \end{aligned} \quad (\text{E.13})$$

It is now possible to evaluate the matrix elements of  $[\zeta_E]_{\mathbf{n},\mathbf{m}}$  by numerically computing the double integrals in Eq. (E.12). Note that the integrand does not suffer from any singularity due to the rescaling of the integration variable. Moreover, the convergence of the  $x'$  integral (E.11) is exponentially fast. The first term in the integrand of the  $t'$  integral decays exponentially at large times. Hence for large times, only the second term yields a contribution, where the integration can be performed analytically in this region. For the case of interspecies scattering of Rb and K in an optical trap, all the parameters entering in  $A$ ,  $h_E(t)$  and  $[F(t)]_{n,m}$  can be expressed in terms of the ratios  $m_{\text{Rb}}/m_{\text{K}}$  and  $\Delta_{\text{Rb}}/\Delta_{\text{K}}$ . The generalization to determine  $\tilde{\zeta}_E$  is straightforward and not detailed further.

## Non-parabolic confinement

A numerical evaluation of the operator  $\zeta_E$  and  $\tilde{\zeta}_E$  is less straightforward when the Green's function  $G_t(\mathbf{R}_\perp, 0; \mathbf{R}'_\perp, 0)$  cannot be computed analytically. In this case,  $G_t(\mathbf{R}_\perp, 0; \mathbf{R}'_\perp, 0)$  should be computed by numerical diagonalization of the  $H_{\perp,i}$  and inserting their eigenvalues and eigenfunctions into Eq. (4.54). For large  $t$ , this is feasible because only a small number of eigenfunctions contribute to the sum. However, for  $t \rightarrow 0$ , the number of eigenvectors required to cancel the divergence in Eq. (4.56) quickly proliferates. This practical limitation can fortunately be circumvented by the following trick. Let us formally rewrite Eq. (4.56) as

$$\begin{aligned}\zeta_E(\mathbf{R}_\perp, \mathbf{R}'_\perp) &= \int_0^\infty \frac{dt}{2\mu} \left\{ e^{Et} [G_t(\mathbf{R}_\perp, 0; \mathbf{R}'_\perp, 0) - G_t^0(\mathbf{R}_\perp, 0; \mathbf{R}'_\perp, 0)] \right. \\ &\quad \left. + e^{Et} G_t^0(\mathbf{R}_\perp, 0; \mathbf{R}'_\perp, 0) - \left( \frac{\mu}{2\pi t} \right)^{3/2} \delta(\mathbf{R}_\perp - \mathbf{R}'_\perp) \right\} \\ &= \int_0^\infty \frac{dt}{2\mu} e^{Et} [G_t(\mathbf{R}_\perp, 0; \mathbf{R}'_\perp, 0) - G_t^0(\mathbf{R}_\perp, 0; \mathbf{R}'_\perp, 0)] \\ &\quad + \zeta_E^0(\mathbf{R}_\perp, \mathbf{R}'_\perp),\end{aligned}\tag{E.14}$$

where  $G_t^0(\mathbf{R}_\perp, 0; \mathbf{R}'_\perp, 0)$  and  $\zeta_E^0(\mathbf{R}_\perp, \mathbf{R}'_\perp)$  are the Green's function and the integral kernel, respectively, for an arbitrary reference confining potential  $V_0(\mathbf{x}_\perp)$ . If  $G_t^0(\mathbf{R}_\perp, 0; \mathbf{R}'_\perp, 0)$  is known analytically, we can deal with  $\zeta_E^0(\mathbf{R}_\perp, \mathbf{R}'_\perp)$  as in the previous section. For confining potentials close to the parabolic case, we choose a parabolic  $V_0(\mathbf{x}_\perp)$ .

Regarding Eq. (E.14), we proceed as follows. We restrict the infinite-dimensional Hilbert space to the  $\mathcal{N}$  lowest eigenstates of the potential  $V_0(\mathbf{x}_\perp)$ , and diagonalize the original Hamiltonian in this  $\mathcal{N}$ -dimensional Hilbert space. With the eigenfunctions at hand, the Green's function can be computed using Eq. (4.54). Then, the sum in Eq. (4.54) is exchanged with the  $t$ -integration and the latter is performed. Next, we project the Green's function onto a known single-particle basis  $\{|m\rangle\}$ . To achieve numerical convergence, we increase the Hilbert space dimension  $\mathcal{N}$  until the result does not change anymore. We emphasize that the overall result converges to the exact result although obviously not all the single-particle states used in computing the Green's function are reliable on very long distances (comparable to the numerical system size) because higher-lying energy states are increasingly inaccurate. Nevertheless, the central part (in position space) of the eigenfunctions – which corresponds to the kinetic energy and does not feel the confinement – is accurate enough to cancel the divergence stemming from the kinetic part. In order to compute the scattering solution, we compute  $\tilde{\zeta}_{E_0}$  with an analogous procedure, diagonalize  $\tilde{\zeta}_{E_0}$  numerically, and insert the result into Eq. (4.80). For the non-parabolic confinement in Sec. 4.6, a parabolic  $V_0(\mathbf{x}_\perp)$  is appropriate. In this case, we use for  $\{|m\rangle\}$  the orthonormal basis defined in Eq. (4.93). Then  $\zeta_E^0$  is diagonal and given by Eq. (4.103).

# References

- [1] G. Galilei, *Il Saggiatore* (1623), in *Opere di Galileo Galilei* (UTET, Torino, 1980)
- [2] A. H. Nayfeh and D. T. Mook, *Nonlinear Oscillations* (Wiley, New York, 1979)
- [3] J. Guckenheimer and Ph. Holmes, *Nonlinear oscillations, dynamical systems, and bifurcations of vector fields* (Springer, New York, 1983)
- [4] E. A. Jackson, *Perspectives of nonlinear dynamics* (Cambridge UP, Cambridge, 1991)
- [5] D. M. Larsen and N. Bloembergen, *Opt. Comm.* **17**, 254 (1976)
- [6] M. I. Dykman and M. V. Fistul, *Phys. Rev. B* **71**, 140508 (R) (2005)
- [7] P. D. Drummond and D. F. Walls, *J. Phys. A* **13**, 725 (1980)
- [8] K. Vogel and H. Risken, *Phys. Rev. A* **38**, 2409 (1988)
- [9] A. P. Dmitriev, M. I. D'yakonov, and A. F. Ioffe, *Sov. Phys. JETP* **63**, 838 (1986)
- [10] M. I. Dykman and V. N. Smelyanskii, *Sov. Phys. JETP* **67**, 1769 (1988)
- [11] M. J. Everitt, T. D. Clark, P. B. Stiffell, J. F. Ralph, A. R. Bulsara and C. J. Harland, *Phys. Rev. E* **72**, 66209 (2005)
- [12] V. Peano and M. Thorwart, *Phys. Rev. B* **70**, 235401 (2004)
- [13] V. Peano and M. Thorwart, *Chem. Phys.* **322**, 135 (2006)
- [14] V. Peano and M. Thorwart, *New J. Phys.* **8**, 21 (2006)
- [15] R. Folman, P. Krüger, J. Schmiedmayer, J. Denschlag, and C. Henkel, *Adv. At. Mol. Opt. Phys.* **48**, 263 (2002)
- [16] J. Reichel, *Appl. Phys. B* **75**, 469 (2002)
- [17] H. Ott, J. Fortagh, G. Schlotterbeck, A. Grossmann, and C. Zimmermann, *Phys. Rev. Lett.* **87**, 230401 (2001); W. Hänsel, P. Hommelhoff, T.W. Hänsch, and J. Reichel, *Nature* **413**, 498 (2001); A. Leanhardt, Y. Shin, A. P. Chikkatur, D. Kielpinski, W. Ketterle, and D. E. Pritchard, *Phys. Rev. Lett.* **90**, 100404 (2003); S. Schneider, A. Kasper, Ch. vom Hagen, M. Bartenstein, B. Engeser, T. Schumm, I. Bar-Joseph, R. Folman, L. Feenstra, and J. Schmiedmayer, *Phys. Rev. A* **67**, 023612 (2003)
- [18] C. Henkel, S. Pötting, and M. Wilkens, *Appl. Phys. B* **69**, 379 (1999)
- [19] Yu-ju Lin, I. Teper, C. Chin, and V. Vuletić, *Phys. Rev. Lett.* **92**, 050404 (2004)
- [20] C. Schroll, W. Belzig, and C. Bruder, *Phys. Rev. A* **68**, 043618 (2003)
- [21] M.A. Kasevich, *Science* **298**, 136 (2002)
- [22] M.S. Dresselhaus, G. Dresselhaus, and Ph. Avouris (eds.), *Carbon Nanotubes* (Berlin, Springer 2001)

- [23] D.S. Petrov, D.M. Gangardt, and G.V. Shlyapnikov, J. Phys. IV France **116**, 5 (2004)
- [24] S. Chen and R. Egger, Phys. Rev. A **68**, 063605 (2003)
- [25] I.V. Tokatly, Phys. Rev. Lett. **93**, 090405 (2004)
- [26] J.N. Fuchs, A. Recati, and W. Zwerger, Phys. Rev. Lett. **93**, 090408 (2004)
- [27] C. Mora, R. Egger, A.O. Gogolin, and A. Komnik, Phys. Rev. Lett. **95**, 080403 (2005)
- [28] M. Olshanii, Phys. Rev. Lett. **81**, 938 (1998)
- [29] T. Bergeman, M.G. Moore, and M. Olshanii Phys. Rev. Lett. **91**, 163201 (2003)
- [30] B. E. Granger and D. Blume, Phys. Rev. Lett. **92**, 133202 (2004)
- [31] M. G. Moore, T. Bergemann, and M. Olshanii, J. Phys. IV (France) **116** 69 (2004)
- [32] T. Stöferle, H. Moritz, C. Schori, M. Köhl, and T. Esslinger, Phys. Rev. Lett. **92**, 130403 (2004)
- [33] B. Paredes, A. Widera, V. Murg, O. Mandel, S. Fölling, I. Cirac, G. V. Shlyapnikov, T. W. Hänsch, and I. Bloch, Nature **429**, 277 (2004)
- [34] T. Kinoshita, T. Wenger, and D.S. Weiss, Science **305**, 112 (2004)
- [35] A. Görlitz, J. M. Vogels, A. E. Leanhardt, C. Raman, T. L. Gustavson, J. R. Abo-Shaeer, A. P. Chikkatur, S. Gupta, S. Inouye, T. Rosenband, and W. Ketterle, Phys. Rev. Lett. **87**, 130402 (2001)
- [36] V. Peano, M. Thorwart, A. Kasper, and R. Egger, Appl. Phys. B **81**, 1075-1080 (2005)
- [37] C. Mora, R. Egger, A.O. Gogolin, and A. Komnik, Phys. Rev. Lett. **93** 170403 (2004); C. Mora, R. Egger, and A.O. Gogolin, Phys. Rev. A **71**, 052705 (2005)
- [38] H. Moritz, T. Stöferle, K. Günter, M. Köhl, and T. Esslinger, Phys. Rev. Lett. **94**, 210401 (2005)
- [39] E. Timmermans, P. Tommasini, M. Hussein, and A. Kerman, Phys. Rep. **315**, 199 (1999)
- [40] V. Peano, M. Thorwart, C. Mora, and R. Egger, New J. Phys. **7**, 192 (2005)
- [41] M. I. Dykman and M. A. Krivoglaz, Sov. Phys. JETP **50**, 30 (1979)
- [42] S. Datta and J. K. Bhattacharjee, Phys. Lett. A **283**, 323 (2001)
- [43] H. G. Craighead, Science **290**, 1532 (2000)
- [44] M. L. Roukes, Physics World **14** 25 (2001)
- [45] A. N. Cleland, *Foundations of Nanomechanics* (Springer, Berlin, 2003)
- [46] M. P. Blencowe, Phys. Rep. **395**, 159 (2004)
- [47] M. P. Blencowe, Contemp. Phys. **46** (4), 249 (2005)

- 
- [48] A. N. Cleland and M. L. Roukes, Appl. Phys. Lett. **69**, 2653 (1996)
  - [49] A. N. Cleland and M. L. Roukes, Nature **392**, 161 (1998)
  - [50] C. T.-C. Nguyen, A.-C. Wong and H. Ding, Dig. Tech. Pap.-IEEE Int. Solid-State Circuits Conf. **448**, 78 (1999)
  - [51] H. Krömmner, A. Erbe, A. Tilke, S. Manus and R. H. Blick, Europhys. Lett. **50**, 101 (2000)
  - [52] A. Erbe, H. Krömmner, A. Kraus, R. H. Blick, G. Corso, and K. Richter, Appl. Phys. Lett. **77**, 3102 (2000)
  - [53] F. W. Beil, L. Pescini, E. Höhberger, A. Kraus, A. Erbe, and R. H. Blick, Nanotechnology **14**, 799 (2003)
  - [54] A. N. Cleland, M. Pophristic and I. Ferguson, App. Phys. Lett. **79**, 2070 (2001)
  - [55] E. Buks and M. L. Roukes, Europhys. Lett. **54**, 220 (2001)
  - [56] X. M. H. Huang, C. A. Zorman, M. Mehregany and M. Roukes, Nature **421**, 496 (2003)
  - [57] R. G. Knobel and A. N. Cleland, Nature **424**, 291 (2003)
  - [58] A. Husain, J. Hone, H. W. Ch. Postma, X. M. H. Huang, T. Drake, M. Barbic, A. Scherer, and M. L. Roukes, Appl. Phys. Lett. **83**, 1240 (2003)
  - [59] M. D. LaHaye, O. Buu, B. Camarota, and K. Schwab, Science **304**, 74 (2004)
  - [60] A. Gaidarzhy, G. Zolfagharkhani, R. L. Badzey, and P. Mohanty, Phys. Rev. Lett. **94**, 030402 (2005)
  - [61] K. C. Schwab, M. P. Blencowe, M. L. Roukes, A. N. Cleland, S. M. Girvin, G. J. Milburn, K. L. Ekinci, Phys. Rev. Lett. **95**, 248901 (2005)
  - [62] A. Gaidarzhy, G. Zolfagharkhani, R. L. Badzey, P. Mohanty, Phys. Rev. Lett. **95**, 248901 (2005)
  - [63] U. Weiss, *Quantum Dissipative Systems* (World Scientific, Singapore, 1993; 2nd edition 1999).
  - [64] P. Mohanty, D. A. Harrington, K. L. Ekinci, Y. T. Yang, M. J. Murphy, and M. L. Roukes, Phys. Rev. B **66**, 085416 (2002)
  - [65] A. B. Hutchinson, P. A. Truitt, K. C. Schwab, L. Sekaric, J. M. Parpia, H. G. Craighead, and J. E. Butler, Appl Phys. Lett. **84**, 972 (2004)
  - [66] X. Liu, J. F. Vignola, H. J. Simpson, B. R. Lemon, B. H. Houston, and D. M. Photiadis, J. Appl. Phys. **97**, 023524 (2005)
  - [67] S. M. Carr, W. E. Lawrence and M. N. Wybourne, Phys. Rev. B **64**, 220101 (2001)
  - [68] P. Werner and W. Zwerger, Europhys. Lett. **65**, 158 (2004)
  - [69] A. Lupascu, C. J. M. Verwijs, R. N. Schouten, C. J. P. M. Harmans, and J. E. Mooij, Phys. Rev. Lett. **93**, 177006 (2004)

- [70] P. Bertet, I. Chiorescu, C. P. J. Harmans, and J. E. Mooij, Phys. Rev. B **70**, 100501 (R) (2004)
- [71] J. C. Lee, W. D. Oliver, T. P. Orlando, and K. K. Berggren, Ieee Trans. Appl. Supercon. **15**, 841 (2005)
- [72] I. Siddiqi, R. Vijay, F. Pierre, C. M. Wilson, L. Frunzio, M. Metcalfe, C. Rigetti, R. J. Schoelkopf, M. H. Devoret, D. Vion, and D. Esteve, Phys. Rev. Lett. **94**, 027005 (2005)
- [73] S. Guérin and H. R. Jauslin, Adv. Chem. Phys. **125**, 1 (2003)
- [74] C. Cohen-Tannoudji, J. Dupont-Roc and G. Grynberg, *Atom-Photon Interactions* (Wiley, New York, 1992)
- [75] I. Shavit and L. T. Redmon, J. Chem. Phys. **73**, 5711 (1980)
- [76] M. C. Goorden, M. Thorwart, and M. Grifoni, Eur. Phys. J. B **45**, 405 (2005)
- [77] S. Nakajima, Progr. Theor. Phys. **20**, 948 (1958)
- [78] V. B. Magalinskii, Zh. Eksp. Teor. Fiz. **36**, 1942 (1959) [Sov. Phys. JETP **9**, 1381 (1959)]
- [79] I. R. Senitzky, Phys. Rev. **119**, 670 (1960)
- [80] R. Zwanzig, J. Chem. Phys. **33**, 1338 (1960)
- [81] R. P. Feynman and F. L. Vernon, Ann. Phys. (N.Y.) **24**, 118 (1963)
- [82] H. Mori, Progr. Theor. Phys. **33**, 423 (1965)
- [83] R. Zwanzig, J. Stat. Phys. **9**, 215 (1973)
- [84] A. O. Caldeira and A. J. Leggett, Phys. Rev. Lett. **46**, 211 (1981)
- [85] A. O. Caldeira and A. J. Leggett, Ann. Phys. (N.Y.) **149**, 374 (1983); **153**, 445 (E) (1984)
- [86] A. O. Caldeira and A. J. Leggett, Physica A **121**, 587 (1983)
- [87] A. J. Leggett, S. Chakravarty, A. T. Dorsey, M. Fisher, A. Garg, and W. Zwerger, Rev. Mod. Phys. **59**, 1 (1987); **67**, 725 (E) (1995)
- [88] H. Grabert, P. Schramm, and G.-L. Ingold, Phys. Rep. **168**, 115 (1988)
- [89] P. Hänggi, P. Talkner, and M. Borkovec, Rev. Mod. Phys. **62**, 251 (1990)
- [90] Th. Dittrich, P. Hänggi, G.-L. Ingold, B. Kramer, G. Schön, and W. Zwerger, *Quantum Transport and Dissipation* (Wiley-VCH, Weinheim, 1998)
- [91] Ch. Mak and R. Egger, Adv. Chem. Phys. **93**, 39 (1996)
- [92] N. Makri, J. Math. Phys. **36**, 2430 (1995)
- [93] N. Makri and D. E. Makarov, J. Chem. Phys. **102**, 4600 (1995)
- [94] W. H. Louisell, *Quantum statistical properties of radiation* (Wiley, New York, 1973)



- 
- [95] F. Haake, in *Quantum statistics in optics and solid-state physics*, Vol. 66 of *Springer tracts in modern physics*, edited by G. Höhler (Springer, Berlin, 1982).
  - [96] S. Kohler, R. Utermann, P. Hänggi and T. Dittrich, Phys. Rev. E **58**, 7219 (1998)
  - [97] M. Thorwart, P. Reimann, P. Jung and R. F. Fox, Phys. Lett. A **239**, 233 (1998); Chem. Phys. **235**, 61 (1998)
  - [98] The time evolution has been computed by means of a simplified Born-Markovian master equation; the driving is included only in its coherent part. The stationary amplitude and the relaxation rate, match with the corresponding results computed with the full Floquet Master equation discussed in Section 2.4.3.
  - [99] M. H. Anderson, J. R. Ensher, M. R. Matthews, C. E. Wieman and E. A. Cornell, Science **269**, 198 (1995); K. B. Davis, M. O. Mewes, M. R. Andrews, N. J. Van Druten, D. S. Durfee, D. M. Kurn and W. Ketterle, Phys. Rev. Lett. **75**, 3696 (1995)
  - [100] C. J. Pethick and H. Smith, *Bose-Einstein Condensation in Dilute Gases* (Cambridge UP, Cambridge, 2002)
  - [101] G. Grynberg and C. Robilliard, Phys. Rep. **355**, 335 (2001)
  - [102] W. H. Wing, Prog. Quantum Electronics **8**, 181 (1984)
  - [103] C.V. Sukumar and D.M. Brink, Phys. Rev. A **56**, 2451 (1997)
  - [104] M. P. A. Jones, C. J. Vale, D. Sahagun, B. V. Hall, and E.A. Hinds, Phys. Rev. Lett. **91**, 080401 (2003)
  - [105] S. Sapmaz, Ya.M. Blanter, L. Gurevich, and H.S.J. van der Zant, Phys. Rev. B **67**, 235414 (2003)
  - [106] H. B. G. Casimir and D. Polder, Phys. Rev. **73**, 360 (1948)
  - [107] E. H. Lieb, W. Liniger, Phys. Rev. **130**, 1616 (1963)
  - [108] V. Dunjko, V. Lorent, and M. Olshanii, Phys. Rev. Lett. **86**, 5413 (2001)
  - [109] H. W. Ch. Postma, A. Sellmeijer, and C. Dekker, Adv. Mater. **17**, 1299 (2000)
  - [110] G.-T. Kim, G. Gu, U. Waizman, and S. Roth, Appl. Phys. Lett. **80**, 1815 (2002)
  - [111] J. Reichel and J.H. Thywissen, J. Phys. IV France **116**, 265 (2004)
  - [112] K. Huang, *Statistical Mechanics* (Wiley, London, 1967)
  - [113] L. D. Landau and E. M. Lifshitz 1977 *Quantum mechanics* (Pergamon, New York, 1977)
  - [114] I. S. Gradshteyn and I.M. Ryzhik 1965 *Tables of Integrals, Series and Products* (Academic Press, London, 1965)

- [115] G. Modugno, G. Ferrari, G. Roati, R. J. Brecha, A. Simoni, and M. Inguscio, *Science* **294**, 1320 (2001)
- [116] Z. Hadzibabic, C. A. Stan, K. Dieckmann, S. Gupta, M. W. Zwierlein, A. Görlitz, and W. Ketterle, *Phys. Rev. Lett.* **88**, 160401 (2002)
- [117] S. Inouye, J. Goldwin, M. L. Olsen, C. Ticknor, J. L. Bohn, and D. S. Jin, *Phys. Rev. Lett.* **93**, 183201 (2004)

## Acknowledgment

*”Die Stadt Düsseldorf ist sehr schön, und wenn man in der Ferne an sie denkt, und zufällig dort geboren ist, wird einem wunderbar zu Mute. Ich bin dort geboren, und es ist mir, als müsste ich gleich nach Hause gehn.”*

*(Heinrich Heine)*

I’m sincerely grateful to my supervisors Reinhold Egger and Michael Thorwart in first place for giving me the great opportunity of working in such a stimulating environment as Heinrich-Heine-Universität, living in a beautiful and homely city as Düsseldorf, and to take part in the open and multicultural German society. I will never forget my German years, the persons I met and what they taught me.

On the working side, I feel obliged to all the colleagues at Heinrich Heine Universität and to the scientists who collaborated with me on the research work contained in this thesis.

On the personal side, I’m especially indebted to all the persons who made me feel at home in Düsseldorf, and to my family & friends for their constant support from far away.

If you fall in one or more of the above categories know that you have my enduring gratitude!

A special acknowledgment goes to Michael Thorwart and Christophe Mora for careful proofreading and helpful suggestions to improve this manuscript.

Last but not least, I wish to thank the SFB Tranregio 12 of the DFG for financial support of my position and for providing a stimulating environment.



# Lebenslauf

## Persönliches

- Vittorio Peano
- geb. 25. 02. 1977 in Milano (Italien)
- Staatsangehörigkeit: italienisch
- Abitur 1996 am Gymnasium S. Alessandro in Bergamo

## Wissenschaftliche Ausbildung

- 1996-2002  
Studium der Physik an der *Università degli studi di Milano*
- Juli 2001-März 2002  
Diplomarbeit am der Lehrstuhl für Theoretische Physik bei Prof. Dr. R. Ferrari  
“*Theory and phenomenology of edge currents in mesoscopic quantum systems*”
- März 2002  
Diplom in Physik (Gesamtnote 110/110 cum laude)
- Aug. 2002-Jan. 2003  
Forschungsaufenthalt an der *Università degli studi di Milano*
- März 2003-heute  
Doktorand am Lehrstuhl für Theoretische Physik IV der Universität  
Düsseldorf bei Prof. Dr. R. Egger
- Feb. 2005-März 2005  
Forschungsaufenthalt an den NTT basic research labs, Atsugi (Japan) bei Prof.  
H. Takayanagi

## Sommerschulen und Konferenzen

- Aug. 17-24, 2003  
*Electrical and Mechanical Properties of Nanowires*, Venice International University (Italien)
- Sep. 27-Okt. 4, 2003  
*Dynamics of Interacting Electrons in Quantum Wires*, Miraflores de la Sierra (Spanien)
- Apr. 3-10, 2005  
*Capri Spring School on Transport in Nanostructures*, Isola di Capri (Italien)

Düsseldorf, den 04.04.2006

## List of publications

- V. Peano and M. Thorwart,  
*Macroscopic quantum effects in a strongly driven nanomechanical resonator*,  
Phys. Rev. B **70**, 235401/1-5 (2004).
- V. Peano, M. Thorwart, C. Mora, and R. Egger,  
*Confinement-induced resonances for a two-component ultracold atom gas in arbitrary quasi-one-dimensional traps*,  
New J. Phys. **7**, 192/1-22 (2005).
- V. Peano, M. Thorwart, A. Kasper, and R. Egger,  
*Nanoscale atomic waveguides with suspended carbon nanotubes*,  
Appl. Phys. B **81**, 1075-1080 (2005).
- V. Peano and M. Thorwart,  
*Dynamics of the quantum Duffing oscillator in the driving induced bistable regime*,  
Chem. Phys. **322**, 135-143 (2006).
- V. Peano and M. Thorwart,  
*Nonlinear response of a driven vibrating nanobeam in the quantum regime*,  
New J. Phys. **8**, 21/1-23 (2006).

# Erklärung

Die hier vorgelegte Dissertation habe ich eigenständig und ohne unerlaubte Hilfe angefertigt. Die Dissertation wurde in der vorgelegten oder in ähnlicher Form noch bei keiner anderen Institution eingereicht. Ich habe bisher keine erfolglosen Promotionsversuche unternommen.

Düsseldorf, den 04.04.2006

---

(Vittorio Peano Cavasola)